Research on Non-destructive Testing Technique for Predicting Joint Resistance of Mechanical Lap Joint at Remountable High-Temperature Superconducting Magnet

Doctoral Thesis

Thesis Title

Research on Non-destructive Testing Technique for Predicting Joint Resistance of Mechanical Lap Joint at Remountable High-Temperature Superconducting Magnet.

Department of Quantum Science and Energy Engineering
Graduate School of Engineering,
TOHOKU UNIVERSITY

WEIXI CHEN

(ID No. B7TD1804)

指　導　教　員	橋爪　秀利　　教授
研究指導教員	
審　査　委　員 （○印は主査）	○　橋爪　秀利　　教授 1　　松山　成男　教授　　2　　長谷川　晃　教授 3　　遊佐　訓孝　准教授　　4　伊藤　悟　　准教授

TOHOKU UNIVERSITY
Graduate School of Engineering

Research on Non-destructive Testing Technique for Predicting Joint Resistance of Mechanical Lap Joint at Remountable High-Temperature Superconducting Magnet

分割型高温超伝導マグネットの機械的ラップジョイントにおける接合抵抗予測に向けた非破壊検査技術の検討

A dissertation submitted for the degree of Doctor of Philosophy (Engineering)

Department of Quantum Science and Energy Engineering

by

Weixi CHEN

7 January 2020

Research on Non-destructive Testing Technique for Predicting Joint resistance of Mechanical Lap Joint at remountable High-Temperature Superconducting Magnet

Weixi Chen

Abstract

The nuclear fusion reactor is under research and development with the aim of next-generation energy sources. Heliotron-type nuclear fusion reactor has an advantage in steadying operation and reducing irradiation because of its heliotron magnetic configuration. The helically twisted superconducting magnet is considered to be the difficulty for realization. “Remountable” (demountable) high-temperature superconducting magnet with coil segments that are mounted and demounted repeatedly using a mechanical joint is proposed to overcome this difficulty. Since the segmented coils still have a number of technical difficulties, the joint-winding concept, where a coil is wound by connecting half- or single-pitch conductor segments using mechanical joints, was proposed and considered as the primary option for the current stage. Ohmic-heating generated by non-superconducting material at the mechanical joint can be tolerance by the use of HTS material. Among the candidates of HTS wires and tapes, the REBCO tape is an adequate option because of its high current density under a high magnetic field, high mechanical strength, and low radio activation. In the study of the joining method using REBCO tapes, the applicability of the mechanical lap joint was validated from the perspective of cooling power. However, the current condition that the electrical resistance at the joint section (joint resistance) is only evaluable after cooling and energizing is unsuitable for the practical application. A technique for predicting joint resistance is inevitable to realize a reliable joint for fusion magnet.

The electrical resistance at the contact interface (contact resistance) of the joint takes a large portion of joint resistance. Therefore, identifying a factor at room temperature that has a correlation with the contact resistance at cryogenic temperature is valuable for the development of predicting technique. The contact condition at room temperature was focused, and two common non-destructive techniques: electrical characteristics evaluation and X-ray computer tomography (CT) scan, were evaluated their applicability to the contact condition evaluation in this study. Subsequently, the adequate technique was introduced to analyze the contact condition varied by the different joint fabrication method.

In the application of electrical characteristics evaluation, the micro air gap is considered to exist at the contact surface and be the cause of the increment of joint resistance. Therefore, applying the alternating current to pass these micro air gaps is considered to form a capacitor, and varied the signal of electric impedance at room temperature. Based on these hypotheses, the electrical impedance of the joint at room temperature was measured and discussed with the joint resistance at cryogenic temperature. Multiple single-layer lap joint samples were prepared and the impedance at room temperature was measured and compared to identify the correlation with the joint resistance. The behavior of capacitor could not be observed from the impedance. And in the correlation, the difference of impedance at room temperature was too small to be measured and distinguish different joint resistance. To identify reason of the correlation, a single-layer lap joint was modeled numerically. The simulation result of current distribution showed an apparent difference in the current

path; the current flow perpendicular to the contact interfaces at cryogenic temperature, whereas the current flow parallel to the contact interfaces at room temperature. The reason for the difference in the current path is the contrast of electrical resistivity of constitutional materials, and result in the difficulty in correspondence of the electric resistance at room temperature and joint resistance at cryogenic temperature. Even in case that wide area of insulating area existing in the joint, the electrical characteristic measurement could not identify the existence of this abnormal contact condition. The applicability of electrical characteristics evaluation is concluded to be inadequate for contact condition evaluation.

In the application of the X-ray CT scan, the cross-sectional images of the contact interface can be extracted and observed visually, the existence of non-contact area like air gap can be recognized. The contact area was calculated using the image segmentation technique. The observed contact area can be used to calculate the contact resistivity more accurately compared to using the conventional contact area, which is simply multiplying the original joint length and width of REBCO tape. Due to the limitation of the resolution, a precise correlation between contact resistance and contact area was not obtainable, but the range of contact resistivity can be evaluated by introducing the contact interface observation using the X-ray CT scan. The X-ray CT scan was chosen comprehensively to further the evaluation of contact conditions with different joint fabrication methods.

In the analysis of contact condition variation on joint fabrication method, joint samples with three kinds of dominant joint fabrication method: eight single-layer joint samples, two two-row-four-layer joint samples with the simple-stack procedure, two two-row-four-layer joint samples with the joint-piece procedure, were prepared and evaluated. The result of the evaluation is valuable for judging the appropriate joint fabrication method for the practical fusion magnet. In the analysis of X-ray CT scan cross-sectional images, the joint accidentally misaligned and overlapped was found. The merit that the application of an X-ray CT scan can detect the deteriorated REBCO tape result from overlapping was recognized. For the evaluation of contact resistivity, the range of contact resistivity for each joint fabrication was 1.77-4.04 $p\Omega m^2$, 2.12-5.15 $p\Omega m^2$, 1.28-6.07 $p\Omega m^2$, respectively. No typical tendency to contact resistivity relying on the joint fabrication method can be identified. The reason for relatively high contact resistivity is surmised to be the non-uniform joint pressuring from the location distribution of contact resistivity. The greatness of uniform pressuring on the joint was recognized. However, even the highest contact resistivity obtained in this study is acceptable in terms of required cooling power from the extrapolating the joint resistance at fusion magnet operation condition. The range of contact resistance is able to be calculated from the contact area observed at room temperature regardless of the joint fabrication method.

In this study, an adequate non-destructive testing technique was searched with the aim of developing a prediction technique for joint resistance of a mechanical lap joint. The electrical characteristics evaluation and X-ray CT scan were chosen as candidates, and the applicability for evaluating the contact condition at the contact interface of the joint was evaluated. The X-ray CT scan performed positive results for its inner observation ability, and the contact resistivity at the contact interfaces can be evaluated more accurately. Subsequently, the contact resistivity variation on the joint fabrication method was evaluated using the X-ray CT scan. The ability to detect the overlapped and deteriorated REBCO was recognized, and the evaluation of contact resistivity with different fabrication method shows no typical tendency. The range of contact resistance is considered to be predictable with the range of contact resistivity and the contact area at the contact interface.

Contents

1 Introduction

1.1 Nuclear fusion reactor[1]

1.1.1 Nuclear fusion reaction

The nuclear fusion reactor is under research and development all over the world. The most feasible nuclear fusion reaction that can be utilized for power generation is considered to be DT reaction. Eq. 1.1 expresses the DT reaction using Deuterium and Tritium to fuse Helium.

$$ {}^{2}_{1}\mathrm{D} + {}^{3}_{1}\mathrm{T} \longrightarrow {}^{4}_{2}\mathrm{He} + \mathrm{n} + 17.6\ \mathrm{MeV} \tag{1.1} $$

In this reaction, helium atom with a kinetic energy of 3.5 MeV and neutron with a kinetic energy of 14.1 MeV are generated. In the nuclear fusion reactor, kinetic energy of neutron is transformed to thermal energy to heat the water and then it drives a turbine to create electricity.

However, to initiate the nuclear reaction on Earth is not simple at all. Since the orbital electrons in an atom prevent two atoms nucleus from fusion, the atom needs to be plasma condition to free the orbital electrons. After being the plasma condition, nuclear fusion is able to be induced when the two nucleus approached. Since the nucleus is charged positively, the energy that more than Coulomb potential, Φ, is need to applied to approach the nuclei. The Coulomb potential is expressed in Eq. 1.2

$$ \Phi = \frac{q_1 \cdot q_2}{4\pi\epsilon_0}\frac{1}{r} \tag{1.2} $$

where q_1 and q_2 are the charge of nuclei, ϵ_0 is permittivity in vacuum, r is the distance between two nuclei. To achieve the distance close enough to fuse, the electron temperature of plasma is need to be raised to more than one hundreds million degree C, The nuclear fusion reaction is able to be realized in laboratory environment, but for a nuclear fusion rector, the generated energy is needed to be enlarged enough to the energy spend for reacting. The inertial confinement fusion and magnetic confinement fusion are the two major branches for the nuclear fusion research.

For the inertial confinement fusion (ICF), the instantly inertia of nuclei is focused to confine and approach the nuclei. Laser-driven ICF is a common method for this type of fusion. The fuel pellet forms sphere with a diameter of 1-2 mm and consisted of deuterium and tritium. The surface of the pellet is heated and vaporized by high-power laser instantaneously (nano-second order). The implosion of inner part is interacted by the expansion of the surface part, and high temperature high density environment at the center of the pellet initiates the nuclear fusion reaction. The difficulty of this technique is considered to be development of high-power and continuous operable laser, laser targeting to the pellet with high precision, high radiative

tolerance material, injection technique for pellet, and emission technique for fusion products. Since the progress in research for laser technique is promising, the further achievement of inertial confinement fusion bears watching.

For the magnetic confinement fusion, the circular motion of the charged particle around the magnetic filed line by Lorentz force is focused. The radius of the circular motion ρ is be expressed as 1.3

$$\rho = |q|\frac{V}{mB} \tag{1.3}$$

where $|q|, V, m$, and B are the charge of the particle, the velocity component of the particle perpendicular to the magnetic file line, the weight of the particle, and magnetic flux density, respectively. In case the magnetic flux density rises, the radius would decrease, and the charged particle will tracked and confined by the magnetic field. To increase the frequency of nuclear fusion reaction, the density of the nuclei is better to rise, and the density of the magnetic field is required to be high. The device with torus-shape field for plasma confinement is including the Tokamak and stellarator, which are the most common nuclear fusion device at current stage.

1.1.2 Torus-shape magnetic confinement device

Fig. 1.1 illustrates the basic configuration of torus-shape magnetic confinement device. The multiple circle-shape coils (toroidal field coil) formed placed with equal interval, and torus-shape closed magnetic field lines are formed. However, this simple torus cannot confine the plasma well. This is because the magnetic field generated by the toroidal field coil (toroidal magnetic field) is not uniform inside the container. Since the magnitude of the magnetic field is inversely proportional to the square of the distance, the farther away from the center of the torus, the smaller the toroidal magnetic field. Due to the gradient of this magnetic field, a grad $\boldsymbol{B}$ drift effect expressed by the following Eq. 1.4 occurs.

$$\boldsymbol{v}_{\nabla B} = \frac{1}{2}mv_{\perp}^{2}\frac{\boldsymbol{B}\times\nabla B}{qB^{3}} \tag{1.4}$$

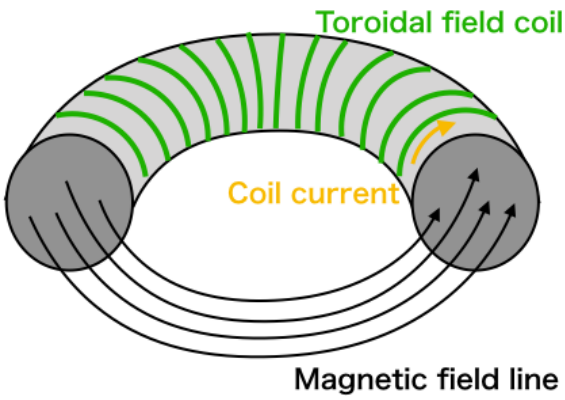

Fig. 1.1: Configuration of torus-shape magnetic confinement

where $\boldsymbol{v}_{\nabla B}, v_{\perp}$are the grad $\boldsymbol{B}$ drift velocity and the velocity component of the particle that perpendicular to the magnetic field. Since the nuclei and electrons, which are charged particles, have different positive and negative charges, they start moving across the lines of magnetic force in opposite directions. This causes a bias in the charge and an electric field. Due to the interaction between the electric and magnetic fields, the $\boldsymbol{E} \times \boldsymbol{B}$ drift expressed in Eq. 1.5 occurs.

$$\boldsymbol{v}_{\boldsymbol{E}\times\boldsymbol{B}} = \frac{\boldsymbol{E} \times \boldsymbol{B}}{B^2} \tag{1.5}$$

Due to the $\boldsymbol{E} \times \boldsymbol{B}$ drift, plasma particles flow from the center of the magnetic field and flow out, reducing the central plasma density and making it impossible to sustain fusion reactions. In order to solve this problem, a magnetic field in the poloidal direction shown in Fig. 1.2 is need to be applied. With the additional magnetic filed, the magnetic field lines in the synthesized magnetic filed are spirally (helically) twisted, and the direction of ions and electrons moving is changed to mix and cancel the effect of $\boldsymbol{E} \times \boldsymbol{B}$ drift. shows this spiral magnetic field.

Among the methods of applying a torsion of the magnetic field in the poloidal direction, a device using electromagnetic induction generated by a center solenoid disposed in the center of the toroidal magnetic field coil is a Tokamak-type, and a magnetic field having a direct torsion generated by changing the shape of the coil is called a stellarator.

As shown in Fig. 1.3, the Tokamak-type device has three types of coils: a toroidal magnetic field coil (Toroidal Field Coil: TF coil), a central solenoid (Central Solenoid: CS), and a poloidal magnetic field coil (Poloidal Field Coil: PF coil), to form a torsion magnetic field. In the ignition of the magnetic field, a torus plasma is first generated along the toroidal magnetic field generated by the TF coil, and then excites the magnetic field in the center of CS by starting to apply current to CS. Since the plasma is the a conductor and surrounding the CS, the current (plasma current, or bootstrap current) is induced inside the plasma and the magnetic field in poloidal direction is generated by the induced current. However, there is a limitation to inducing the current due to the upper limit of magnetic field excited by CS. The continuous plasma current is driven by neutral beams or electromagnetic waves. A force acts in the direction in which the plasma radius expands in the torus plasma and deteriorate the confinement efficiency. Therefore, this

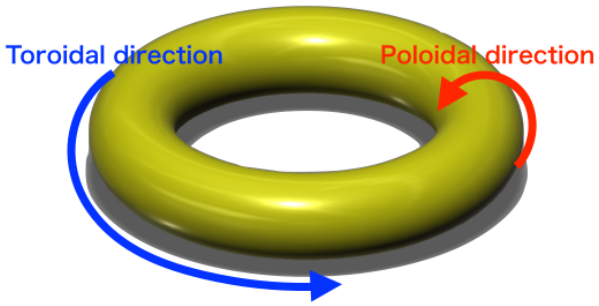

Fig. 1.2: Direction in torus-shape of magnetic filed

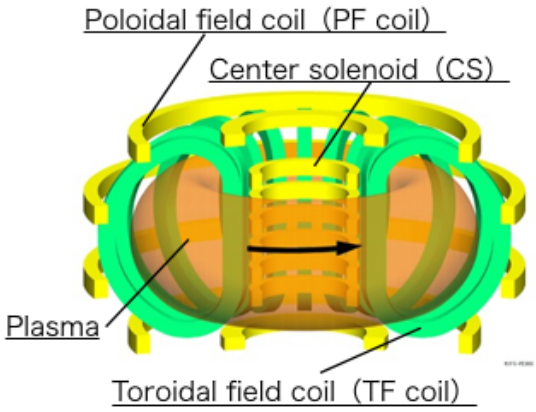

Fig. 1.3: Coils in Tokamak-type divice[2]

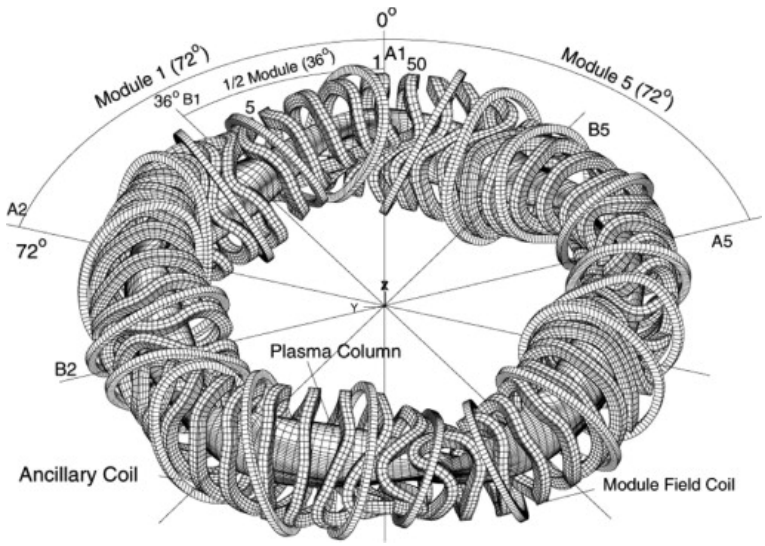

Fig. 1.4: Coil of Wendelstein 7-X[3]

adjustment is performed using a magnetic field generated using a PF coil. The Tokamak-type experimental device currently records the highest fusion reaction efficiency among magnetic field confinement devices, and based on this result, the experimental reactor ITER is now being built in Cadarache, France with international cooperation. Maintain the plasma current is an inevitable key technique to realize the steady operation in Tokamak-type fusion reactor.

In a device of stellarator, confined magnetic field is formed and twisted by a steady current magnetic field of the coil. Maintaining plasma current to generate the magnetic field in poloidal direction is not a problem. An example of an experimental device that has been researched and developed is the Wendelstein 7-X designed and constructed by Max Planck Institute in Germany. As shown in Fig. 1.4, this device generates both a toroidal magnetic field and a poloidal magnetic field by using a modular coil with a twist in the toroidal coil. However, the shape of the device is very complicated, and the poor internal accessibility can be expected.

In Japan, the National Institute for Fusion Science (NIFS) located in Gifu prefecture has been conducting design and verification tests of a unique heliotron-type device. Fig. 1.5 shows the shape of coils in a heliotron-type device, and an experimental device called Large Helical

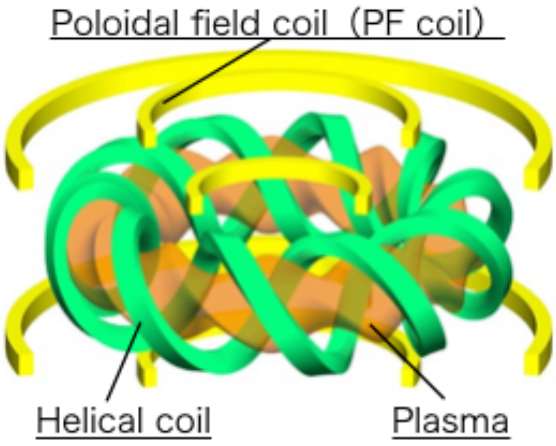

Fig. 1.5: Configuration of the coils from heliotron-type device [2]

Device (LHD) [4] was developed and used for plasma research. Based on the knowledge acquired from LHD including the conceptual design and the results of physical engineering in experiments, a demonstrate fusion reactor, the FFHR series [9]-[13], is under research and developed.

1.1.3 Heliotron-type nuclear fusion reactor FFHR-d1

FFHR-d1 shown in Fig. 1.6 is a prototype fusion reactor of heliotron-type reactor. The FFHR-d1 superconducting magnet is designed using a heliotron configuration in which both a toroidal magnetic field and a poloidal magnetic field are generated by a three-dimensional helical coil shown in Fig. 1.5. The magnetic field is generated by the DC current flowing through the helical coil, and has a great advantage that the steady operation is easy in principle compared to the Tokamak-type as described above. The cross section in Fig 1.6 shows the neutron flux irradiated, and the amount of neutron irradiation in equipment such as helical coils, poloidal coils, and divertors is small [10]. This not only reduces the activation of the material but also reduces the thermal conductivity lowering of the material due to neutron irradiation, which is very advantageous from the viewpoint of removing heat with high heat flux. Such an arrangement is possible because these important devices can be placed behind the plasma facing device due to the magnetic field lines of the heliotron configuration. If it is possible to reduce the deterioration of equipment, the frequency of equipment replacement, that is, the maintenance, can be reduced, and the economical efficiency of the furnace increases. It can be said that this type of fusion reactor is a suitable option for commercial reactors.

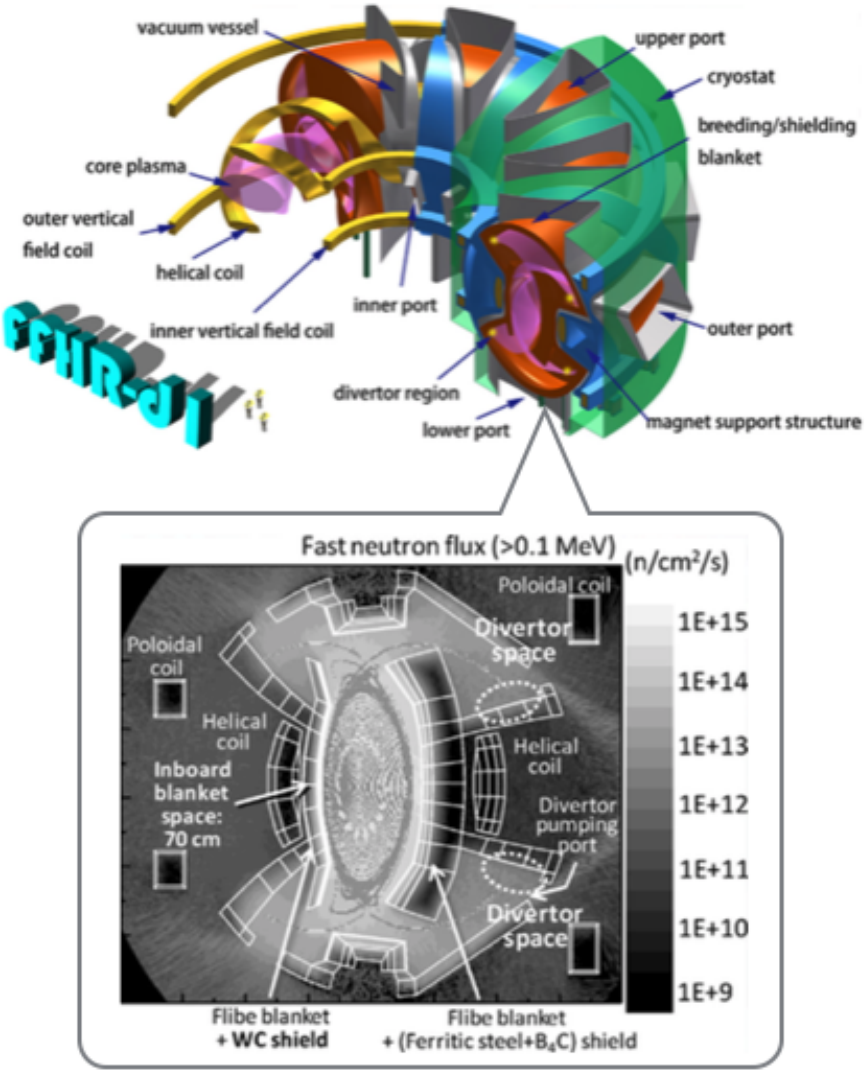

Fig. 1.6: FFHR-d1[10]

1.2 Superconducting magnet for fusion reactor

1.2.1 Nuclear fusion superconducting magnet

In the nuclear fusion reaction using the magnetic field confinement method, it is necessary to confine the nuclei in a strong magnetic field for as long as possible in order to cause the nuclei to collide with each other. A large current is needed to flow through the coil to generate a strong magnetic field. Copper is used for conductors such as ordinary electric wires, but copper has Joule heat when current flows due to its electrical resistance. Although a method of increasing the cross-sectional area of the conductor to suppress heat generation is conceivable, it is not suitable for a nuclear fusion reactor for power generation because it consumes more power for pump output for flowing cooling water.

Here we use an ITER size reactor for comparing the power consumption between normal conductor and superconductor. If the TF coil in ITER are constructed with water-cooled copper coils, the estimated power consumption for 18 TF is 1800 MW in total [5]. But the consumption of electric power for refrigerating superconducting coil in ITER is designed to be 35 MW [8]. On the other hand, superconducting magnets have almost no power loss due to perfect conductivity, the power consumption for cooling can be greatly reduced. Considering that the heat output of ITER is 500 MW, the use of a superconducting magnet is an indispensable condition for the establishment of a reactor for power plant. In addition, superconducting magnets can generate a strong magnetic field, which can increase the efficiency of plasma confinement. Therefore, a superconducting magnet was devised for the coil in the fusion reactor.

NbTi and Nb_3Sn are the material for superconducting magnet commonly used in the magnetic field confinement fusion experimental device currently in operation or under construction. The temperature at which the superconductor transitions to the superconducting state is called the critical temperature (T_c), and the critical temperatures of NbTi and Nb_3Sn are 10 K and 18 K, respectively. Therefore, it is necessary to use liquid helium (boiling point 4.2 K) to cool these superconducting material. On the other hand, since 1986, copper oxide superconductors whose critical temperature exceeds the boiling point of liquid nitrogen (77 K) have been discovered and developed. Superconductors with a T_c higher than the boiling point of liquid nitrogen are classified as high-temperature superconductors (HTS), and those with the T_c lower than that It is called the Low Temperature Superconductor(LTS). In recent years, with the commercialization of high-temperature superconductors, the use of high-temperature superconductors in fusion reactors has been studied.

The phenomenon in which the superconductor loses its superconducting state due to external factors such as temperature rise is called quench. To ensure safe operation of the coil, it is necessary to design a conductor that avoids this phenomenon. Conductors called cable-in-conduit conductors are used for ITER coils and LHD PF coils. This conductor is made by

inserting hundreds of NbTi and Nb_3Sn wires into a stainless steel tube by twisting them together, and forcing a liquid helium refrigerant into the tube to directly cool the superconductor. On the other hand, an immersion cooling coil using NbTi / Cu composite superconductor stabilized with high-purity aluminum is used for the helical coil of the LHD, which is cooled by immersing the coil in liquid helium. In these conductor design, the cooling method of the superconductor is always cooled by the refrigerant, and the quench is designed to be suppressed even if some thermal disturbance occurs near the superconductor.

However, it is not easy to manufacture the conductor designed as described above in practice. For example, Nb_3Sn, which is to be used in ITER TF coils and CSs, reduces the maximum flowable current (critical current) to 1/3 with only 0.6% strain applied to the conductor. Therefore, there is a Wind and React method in which a coil is formed by combining niobium and a copper-tin alloy to perform heat treatment in order to minimize strain [14]. This requires a very large heat treatment furnace, which leads to an increase in manufacturing costs. For the other candidate of superconducting material, NbTi is an alloy and has larger tolerance to stress degradation than Nb_3Sn, and was used as a material for winding LHD helical coils. However, it was necessary to perform a complicated and sophisticated long-time task of winding a 36-km-long superconductor around a vacuum vessel over a year and a half using a special winding device [15][16]. The helical fusion reactor FFHR-d1, which is currently being designed, needs to increase the heat output for power generation. It is necessary to increase the size of fusion plasma that can be confined, and it is unavoidable to increase the size of the reactor. The size of the superconducting magnet in FFHR-d1 is expected to be about four times as long as the LHD. Using the method of manufacturing a helical coil for LHD, it expects to take about six years for manufacturing helical coil by simple calculation. Therefore, it is necessary to adopt a method that can manufacture the coil in a shorter time through the designing process. Furthermore, in commercial reactors, the plasma-facing equipment such as blankets and divertors need to be replaced after a certain period of operation due to the aging and neutron irradiation. However, since the helical coils are arranged so as to surround these reactor internal structures, it is necessary to disassemble and remanufacture the helical coils every time they are replaced. The reactor will not be economically viable with such a long time for maintenance.

1.2.2 Remountable superconducting magnet

To overcome the difficulty of realizing helical coil, the idea that separating and assembling the superconducting magnet with use of high-temperature superconducting magnet was proposed and developed [17]-[24]. This idea achieves facilitating the manufacturing and shortening the manufacturing time. And because the superconducting magnet can be detached in parts, the accessibility inside the reactor can be significantly improved. The segmented fabrication of the magnet on Tokamak-type fusion magnet has also been studied [25]-[28].

The original concept of the Remountable (demountable) high-temperature superconducting magnet is shown in Fig. 1.7 (a). This concept aims at dividing and manufacturing a helical coil as a segment every half cycle. In addition, by enabling the attachment and detachment of each segment, partial maintenance and inspection and replacement of the helical coil become possible, and furthermore, the internal accessibility is improved and the maintenance of the furnace internal structure becomes easier. As a result, the helical fusion reactor has a great advantage in operating as a commercial reactor, and this concept is considered as an option for advanced fusion reactors.

However, several challenging tasks are needed to achieve to realize the remountable high-temperature superconducting magnet described above. For instance, several hundred superconducting conductors (390 in the design stage of FFHR-d1) that constitute the coil segment must be joined with electrically insulator surrounding the conductor, or the technique for detaching the irradiated huge size coil segment. Therefore, in the FFHR-d1 design of NIFS, the connection method of the entire coil segment was discontinued, and a conductor connection winding method in which the helical coil is wound while connecting the superconducting conductors one by one was proposed. This concept is shown in Fig. 1.7 (b). This method does not make it demountable, but it can reduce manufacturing costs and time, greatly increasing its feasibility even at the current technology level.

Another important factor introduced to this concept recently is to use a high-temperature superconductor. At the joint of the remountable high-temperature superconducting magnet, the electric current flows through a part that is not a superconductor, so that electrical resistance generated Joule heat. Since this heat generation is steady heat generation, the temperature of the joint becomes constantly high. When a low-temperature superconductor is used, the joint has a low temperature tolerance to the critical temperature be cause of the generated heat [17]. At cryogenic temperatures, the specific heat of a substance has a Debye's cube law, which is proportional to the cube of the absolute temperature. When a quench occurs at the location due to thermal disturbance once, it is easy to propagate since the surrounding superconductors

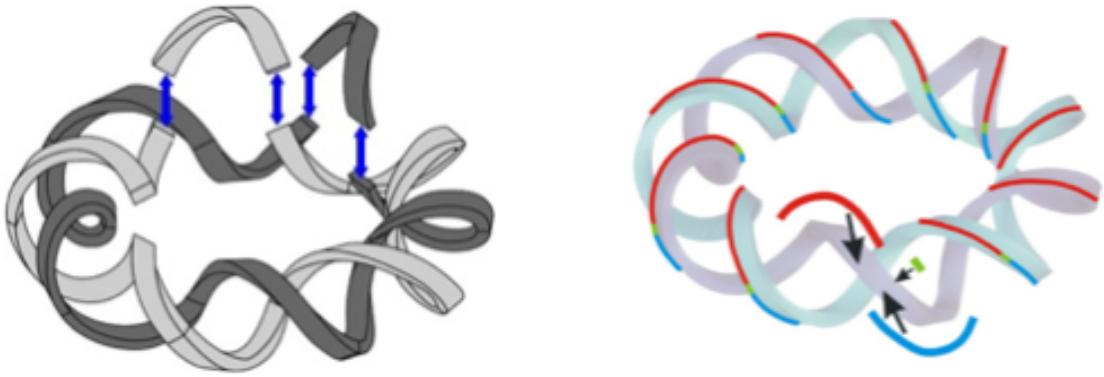

(a) Remountable [21] (b) Joint-winding [22]

Fig. 1.7: Concept of segmented fabrication for helical coil

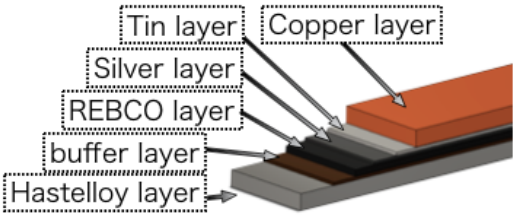

(a) REBCO tape with soldered stabilizer layers

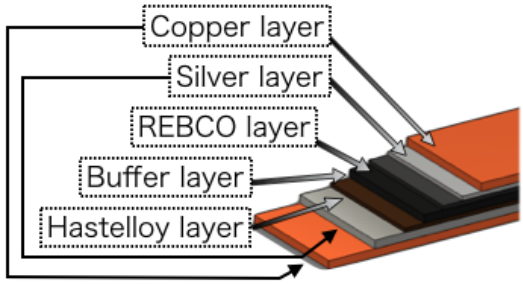

(b) REBCO tape with electroplated stabilizer layers

Fig. 1.8: Configuration of REBCO tape

has little temperature margin to transit to a normal state. On the other hand, by using a high-temperature superconductor, the operating temperature can be set to 20-30 K. With higher specific heat, higher heat capacitor can be achieved and the temperature rise due to thermal disturbance is less likely to occur. In addition, since the margin between the critical temperature and the operating temperature is large enough, quench propagation are also unlikely to occur. Therefore, it is necessary to use a high-temperature superconductor instead of a low-temperature superconductor in a remountable magnet that has a steady Joule heating at the joint. Among the potential HTS wires and tapes, rare-earth barium copper oxide (REBCO) tape is considered to be an ideal candidate because of its high current density under high magnetic fields, high mechanical strength, and low radioactivation.

The structure of the REBCO tape is layered structure as shown in Fig. 1.8, and the detail of the tape is explained in Section 2.1.

1.3 Joining technique

1.3.1 Studies about joining

High-temperature superconductors are generally commercialized as tape configuration. Several types of resistive lap joint have been studied for various HTS applications. Solder joint with tin-lead solder has achieved joint resistivity (the product of the joint resistance and the nominal contact area) of 2-5 pΩm^2 at 77 K, self-field [29]-[31]. However, tin-lead solder has a risk to decrease critical current (I_c) due to the temperature limit of HTS material without oxygen annealing in a large-scale conductor with a length of one meter which has temperature gradient at the soldering process and prolonged soldering time. Nano-particle metal paste joint is one example not require oxygen annealing, and it realized 4.8 pΩm^2 with 1 hour heat treatment [32]. One candidate to shorten the joining process is ultrasonic welding (UW) [33]. Combined UW technique with solder realized 5.7 pΩm^2 [34].

1.3.2 Mechanical joint

When used in a coil, multiple layers are stacked and wrapped in a copper or stainless steel jacket and used as a single superconducting conductor to keep high current capacity. In order to suppress the occurrence of quench at the joint, the electrical resistance of the joint must be as small as possible, several mechanical joining methods for the joint as shown in Fig. 1.9 were proposed and studied[35]-[41]. Mechanical joining is a method of joining by applying pressure from the outside with screws or bolts instead of using solder. In this joining method, basically the joining surface is ground with abrasive paper to reduce the joining resistance (electrical resistance generated at the joint section: that was experimentally evaluated from the applied current and the voltage drop in the section including the joining part). After the cleaning oxide film and smear on the joint surface, the joint is pressurized to join. However, the resulting oxidize film and smear, and unevenness of the joint surface and non-uniform joining pressure on the joint surface cause an increment in joint resistance. Therefore, it has been proposed to insert an indium foil, which is a soft metal, between the joining surfaces to uniform the joining pressure and improving the joint conditions.[38]

The mechanical butt joint shown in Fig. 1.9 (a) is a method to join the conductor with cross section of conductor. The advantages of this joining method include the freedom to change the angle of the joining surface and the ease of grinding the necessary joining surface before joining. However, when a current flows through the conductor, the electromagnetic force acts in a way that separates the joining surfaces. It is necessary to design a joint support structure that can withstand the electromagnetic force. In a previous study, conductors of this joining method were fabricated with 10 layers of GdBCO high-temperature superconducting tapes, and the result was that the bonding resistance was 800 nΩ at 77 K [35].

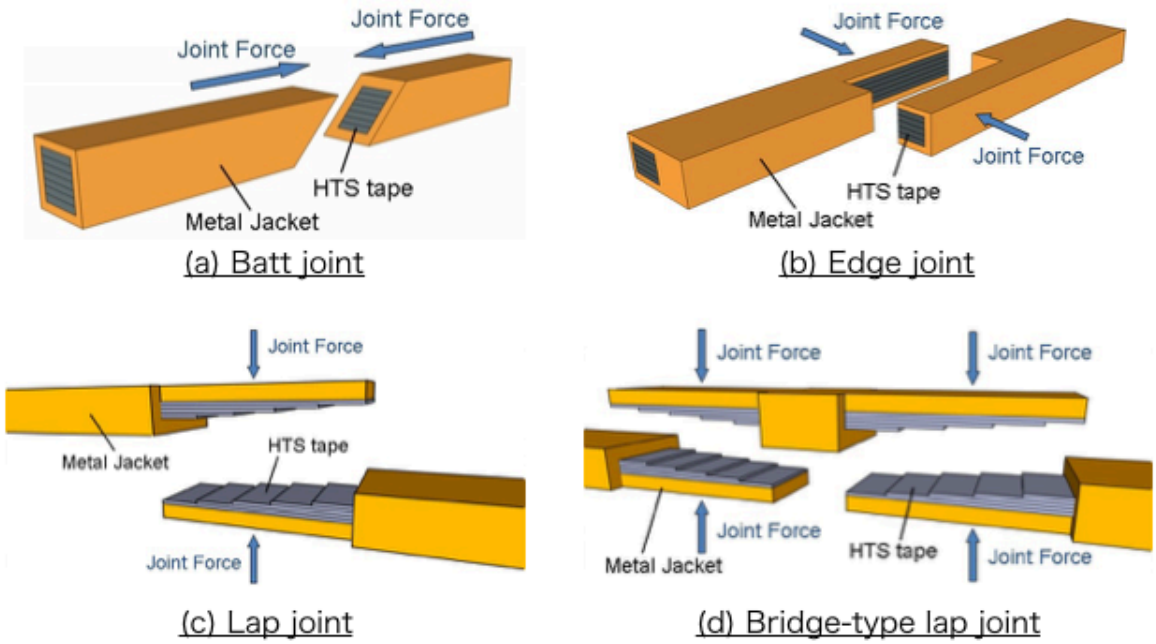

Fig. 1.9: Concept of joining technique[21]

The mechanical edge joint shown in Fig. 1.9 (b) is a joining method that is perpendicular to the lamination direction of the laminated REBCO tapes and that is joined in the conductor cross section in the axial direction. This joining method can secure a sufficient contact area and can maintain the contact area even when an electromagnetic force is generated in the axial direction during energization. At present, a mechanical edge joint conductor with a joint length of 50 mm has been fabricated with 10 GdBCO tapes, and has achieved a performance of 80 nΩ at 77 K [36] [37].

The mechanical lap joints shown in Fig. 1.9 (c) and (d) are the joints that have a structure in which the superconducting tapes overlaps like a staircase. This joining method has the merit of easy to secure joining area for lowering the joint resistance and facilitating enlarging the conductors size. As shown in Fig. 1.9 (c), a single mechanical lap joint is joining by pressuring the two conductor with the surface of the REBCO tapes face to each other. In the case of the bridge-type mechanical lap joint of the shown in Fig. 1.9 (d), another part is prepared for the joint, and two joint is pressuring together. In this method, since the divided conductors of the helical coil have almost the same structure, same coil segment can be manufactured in one production line, and the production cost can be expected to reduce. In addition to cost, single mechanical lap joints require high accuracy for the configuration of conductor to adjust two conductor for joining, whereas the bridge-type mechanical lap joint can be modified accordingly using the additional joint part.

In a previous study, a large-sized conductor with a bridge-type mechanical lap joint consisting of three rows and 14 layers using a REBCO tapes was fabricated and tested [40]. A current of 118 kA and a joint resistance of 2 nΩ(joint resistivity, the product of joint area and joint

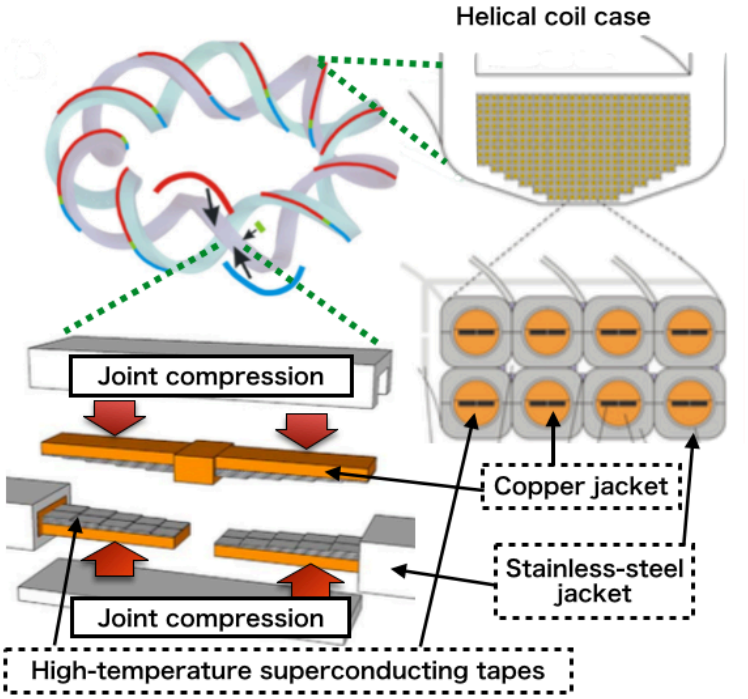

Fig. 1.10: Design concept of coil fabrication [10]

resistance : 10 pΩm^2) was successfully achieved at 4.2 K and 0.45 T. The applicability of the joint was validated from a perspective of cooling power. This joining method using joint-winding with mechanical lap joint is considered to be the primary option for FFHR-d1 at current stage as shown in Fig. 1.10.

1.3.3 Joint resistance at mechanical lap joint

The current path at joint section of a mechanical lap joint is illustrated in Fig. 1.11. The current is considered to flow the superconducting material as long as possible, then cross the joint section with the direction perpendicular to the contact interface. Referring to the current path, the components make up for the joint resistance can be illustrated as a series of electrical resistances as Fig. 1.12.

$R_{\mathrm{Ag}}, R_{\mathrm{Cu}}$ is the electrical resistance of silver layer and copper layer of REBCO tape, R_{inter} is interlayer resistance inside the REBCO tapes, R_{In} is the electrical resistance of indium foil inserted between the REBCO tape, and the R_{Contact} is the electrical resistance at the contact interface. $R_{\mathrm{Ag}}, R_{\mathrm{inter}}, R_{\mathrm{Cu}}$ depend on the manufacturing of REBCO tape, and predictable in

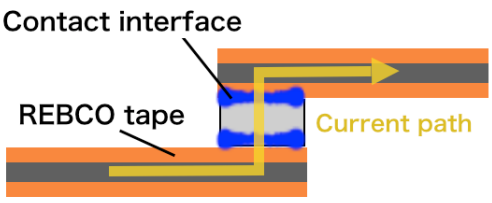

Fig. 1.11: Current path at joint section

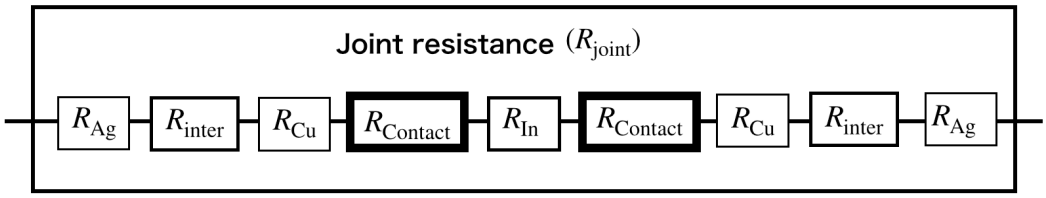

Fig. 1.12: Equivalent circuit of joint resistance

advance to the cooling and energizing. R_{In} is variable and depends on the thickness of indium foil. Although the indium is known for its relatively high resistivity among the materials, the range of variation is limited, and it decreases to low [75] at the designed operating temperature of 20 K. R_{Contact} is the most important portion amounts for the joint resistance, and is variable depending on the joining condition; contact surface condition and the joining pressure. And the previous studies indicated the range of variation is wide because of the handling of pressuring. However, the joint resistance could only be evaluable after cooling, and energizing because of the difference in the current path between the ambient and cryogenic environments at the joint. This situation is not desirable; the helical coil is constructed with 7800 joints using half-pitch segments [10]. A technique for lowering the range of variation of the contact resistance, and an inspecting and qualification technique at room temperature is indispensable to realize a reliable fabrication process for these joints.

1.3.4 Research and development for lowering variation of contact resistance

To lowering the range of variation of the contact resistance, low-temperature heating process has be studied [46]-[48]. Raising the temperature below the melting point of indium during the joint fabrication is effective to soften indium, uniform the joining pressure, improve the contact condition and lower the joint resistance. The contact resistance was validated to decreased to one-fifth by the approximately 100 °C heating.

In the previous studies, the severalfold joint resistance in multilayer joint compared to the single layer joint was a problem and considered to cause by the difficulty in placing the indium foil precisely for uniform pressurization [39][40]. introducing the heating process was expected to solve this problem by softening the indium inside the completely stacked joint. The conductor that structured with simply stacked 13 layers of REBCO tapes and pressuring with 90 °C of heating is fabricated and evaluated.[49] The sample was measured at 77 K, and $5.0 - 12.8$ $\mathrm{p\Omega m^2}$ of joint resistivity was obtained and the value was compatible to those of the single layer lap joint. Subsequently, another fabrication method using an integrated joint piece was proposed and tested [50]. In this method, the REBCO tapes was fixed to form an integrated joint piece firstly, then the integrated joint piece and conductor region was pressured together. The join resistivity ranged $4.2 - 7.1$ $\mathrm{p\Omega m^2}$ was acquired. We named the former the simple-stack procedure, and the latter the joint-piece procedure. From the result of joint resistivity,

Table. 1.1: Comparison of conditions from two previous studies [49] [50]

Fabrication Method	Used REBCO tape	Condition of REBCO tape	Temperature of heat process	Joint resistivity ($p\Omega m^2$)	Concern
Simple-stack	FYSC-SC10 10-mm-width from Fujikura Ltd.	Free	90 °C	5.0-12.8	Unevenness of REBCO Tape Cross-section
Joint-piece	SDS12050-AP 12-mm-width from Super Power Inc.	Fixed	120 °C	4.2-7.1	Possible Unevenness of Contact surface

joint-piece procedure shows better joint performance. Besides, the fixed REBCO tapes in join-piece procedure is intrinsically preventable to the REBCO tape deterioration by misalignment reported before [39]. However, indeed, the two obtained result could not be used in comparison due to the difference in sample fabrication conditions as listed in Table. 1.1 And how far does the well-known dog-boning geometry cross section of REBCO tape with electroplated stabilizer layers influence the contact surface is unknown. Dog-boning is the term commonly used to describe an unevenness thickness of stabilizer layers formed by electroplating. With this shape, often the layers are thicker near the tape edges, leading to a shape of typical bone. To identify the preferable joint fabrication method for application, two joint methods needs to be evaluated with same fabrication conditions and then compare the contact resistance. The final conclusion needs to be considered comprehensively.

1.3.5 Candidates for development of non-destructive evaluation technique

Aside from the progress in lowering the range of variation of the contact resistance, the prediction technique for the contact resistance at cryogenic temperature was still unestablished. In advance to realize a prediction technique for contact resistance, a method for evaluating the contact resistance is need to be constructed. Two techniques: electrical characteristics measurement and X-ray Computer tomography scan, were considered to be suitable for evaluating contact resistance. The brief for the two techniques is explained following.

- Electrical characteristics measurement

  Measuring the impedance of joint at room temperature was considered to be the simplest and effective way to predict joint resistance at cryogenic temperature. This is because the current was considered to pass the joint, and measured signal would contained the information about the contact interface. Air gap, or non-contact area was considered to exist at the contact interface and become the main cause for the increment of contact resistance. In case the alternating current was applied through these area, the gap possibility behaves as capacitor, and change the electrical characteristics of the joint. Based on this assumption, the correlation between the electrical characteristics at room temperature and the contact resistance at cryogenic temperature is required to be clarified.

- X-ray Computer Tomography scan

  X-ray computer tomography (CT) scan is known for its excellent nondestructive inner inspection ability. The area of X-ray CT scan application is not only limited to biological field but also industry area. Relating to the superconducting material, it was used for analyzing condition of filament in superconducting material [42] [43], and tracing trajectories of superconducting wires in Cable-in-Conduit Conductor (CICC) [44]. As a pioneer to introduce this technology for analyzing joint, our laboratory's earlier study [45] has used X-ray CT scan to observe the contact interfaces to evaluate the area or to analyze the contact condition inside the joint. With the inner observation of the X-ray CT scan, the existence of random gaps at the contact interfaces was confirmed, which is considered to be the cause for contact resistance increment. Based on the ability of X-ray CT scan, it is reasonable to introduce this state-of-art technology for analyzing contact resistance formed by contact interface inside the joint.

1.4 Objective

As aforementioned background, the prediction technique at room temperature for joint resistance at cryogenic temperature is inevitable for the realization of reliable joint. Since the most important composition of the joint resistance is contact resistance, the prediction of the contact resistance is effective. Finding a parameter related to the contact condition at room temperature that has correlation with the contact resistance at cryogenic temperature is important. The objective of this study is to identify the appropriate technique for inspecting the contact condition at room temperature and evaluating the correlation with the contact resistance at cryogenic temperature. Subsequently, using the correlation evaluated before to discuss the contact condition from the perspective of different joint fabrication method: simple-stack procedure and joint-piece procedure, and obtain the useful information to conclude the preferable joint.

Fig. 1.13 shows the content of implementation. The first step is to identify the appropriate technique for inspecting the contact condition. The electrical characteristics evaluation and X-ray CT scan were selected as the candidates for the inspection technique. The applicability of the two techniques was evaluated and discussed in chapter 3 and chapter 4 accordingly. The simplest configuration of the lap joint: single-layer lap joint with 4-mm-width and 5-mm-width of REBCO tape was used to discuss. As the X-ray CT scan was chosen as the appropriate technique, the second step is to use the X-CT scan to evaluate the influence of different joint fabrication methods on contact conditions. The content of the evaluation is reported in chapter 5. Single-layer lap joint with 12-mm-width REBCO tape, two-row-four-layer joint sample fabricated by simple-stack procedure and joint-piece procedure with 12-mm-width REBCO tape was prepared. The contact resistivity, which is calculated by multiplying the contact area and contact resistance, was evaluated and compared to discussed the intrinsic feature influenced by the fabrication method. The applicability of the evaluated contact condition was analyzed by extrapolating the joint resistance and compare it with operating conditions in a fusion reactor. In chapter 6 section, the achievement of this study was summarized.

1. Construction of contact resistance evaluation method

subject : Single-lap joint sample with 4-mm-width and 5-mm-with REBCO tape

1) Application of electrical characteristics evaluation **(Chapter 3)**
- Empirical evaluation for correlation between joint resistance at cryogenic temperature and electrical characteristics at room temperature
- Numerical simulation for current path at the joint for analyzing the correlation

2) Application of X-ray CT scan **(Chapter 4)**
- Observation for cross-sectional image at contact interface
- Contact area evaluation with image segmentation
- Evaluation for contact resistivity

2. Analysis of contact condition for optimizing joint fabrication method between simple-stack procedure and joint piece procedure(Chapter 5)

subject 1 : Single-lap joint sample with 12-mm-width REBCO tape
subject 2 : Two-row-four-layer joint sample with 12-mm-width REBCO tape

- Fabrication and evaluation of joint sample
- Evaluation for influence of fabrication method on contact resistivity
- Evaluation for applicability of acquired contact resistivity

Fig. 1.13: Implementation of this study

2 Theories

2.1 Superconductivity[51]

2.1.1 Discovery of superconducting

The superconductivity phenomenon was discovered in 1911 by Kamerlingh Onnes of the Netherlands. Onnes was an expert in low-temperature physics, and for the first time in 1908, the liquefaction of helium, which had no success at the time, enabled him to reach an absolute temperature of 4 K. At that time, discussions were held on what would happen to the electrical resistance of the metal if the temperature was reduced to absolute zero, and there were two opinions: the electrical resistance became infinite and the electrical resistance became zero. Under these circumstances, Ones considered that electric resistance would not be zero if impurities were present, and tried a demonstration test using mercury obtained at a high purity at that time. In the process, he accidentally discovered that the electrical resistance of mercury suddenly became zero near 4 K. Onnes did not present the phenomenon at once, but modified the purity of mercury and iterated the validation to confirm the existence of zero resistance. And finally, he declare that a completely new state of superconducting exists.

2.1.2 Characteristics of superconducting

When the superconductivity phenomenon was discovered, an immediate application was the production of powerful electromagnets. This is because if the electric resistance is zero, it is possible to pass a large current through a thin conductive wire without generating heat, and it is thought that a compact electromagnet that generates a strong magnetic field can be manufactured by superconducting coil. However, it was found that the superconducting coil at that time could generate only a weak magnetic field. This is because the critical magnetic field (Critical field: H_c) is a condition to maintain the superconducting state, and that of the superconducting material at the stage was about 0.1 T. In the superconducting state, the electric resistance becomes zero, but when a current is applied, extra energy is added to the superconducting state, and the state changes from the superconducting state to the normal conducting state at a certain current density. The critical value of the current density is called critical current density (Critical current density: J_c). As shown in Fig. 2.1, the three conditions combining the above two critical conditions and the first mentioned critical temperature (Critical temperature: T_c) evaluate the superconducting state. In order to maintain the superconducting state, it is necessary to fall below any of these limits (included in the boundary enclosed by Fig. 2.1).

For the explanation of superconducting state, the condition that electrons fills the energy

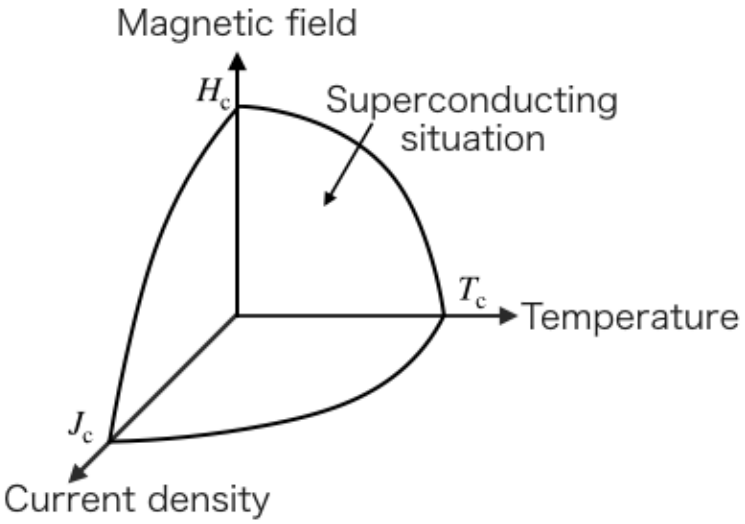

Fig. 2.1: Condition for superconducting situation

levels is shown in Fig. 2.2. The arrow of electron expressed the spin of electron. The electron is Fermi particle and cannot enter more than one in the same energy level and spin according to the Pauli exclusion principle as Fig. 2.2(a). Therefore, the electrons are moving in the metal randomly, scattered by the lattice oscillation and impurities, and result in electrical resistance.

On the other hand, the electrons make pairs in superconducting state, and the name of pair is cooper pair. Intrinsically, the negatively charged electron could not form pairs because of the repulsion force. The the phenomenon was explained by J. Bardeen, L. N. Cooper, and J. R. Schriefer, in BCS theory. The mechanism of the forming electron pair is illustrated in Fig. 2.3 In the metal, the positively charged nucleus is distributed in grid, and a negatively charged electron was moved into the grid and pulled the nucleus sounding the electron. The grid was distorted and the center are that nucleus assembles behaves as a positively charged area to pull another electron. The two electrons seems to interact through the nucleus grid, attract each other and apparently form cooper pairs. According to the BCS theory, the electrons interact each other would result in Bose Einstein concentration and drop to the lowest energy level as a Bose particle shown in Fig. 2.2(b). In case the electric field applied to this state, the electron will start to move all together and be accreted unless the cooper pair was broken. These electron display the superconducting state, and the energy that destroy the cooper pair is according to the critical temperature of the superconducting material.

Perfect conductor and perfect diamagnetism are the typical features of superconducting material. The perfect conductor is the feature that the electrical resistance is completely zero at superconducting condition. According to the Maxwell equation expressed in Eq. 2.1, in case the electric field $\boldsymbol{E}$ inside the superconducting material, $\frac{\partial \boldsymbol{B}}{\partial t}$ is zero. The magnetic filed $\mathbf{B}$ is constant.

$$\nabla \times \boldsymbol{E} = \frac{\partial \boldsymbol{B}}{\partial t} \tag{2.1}$$

Two assumption can be established from the contact magnetic field.

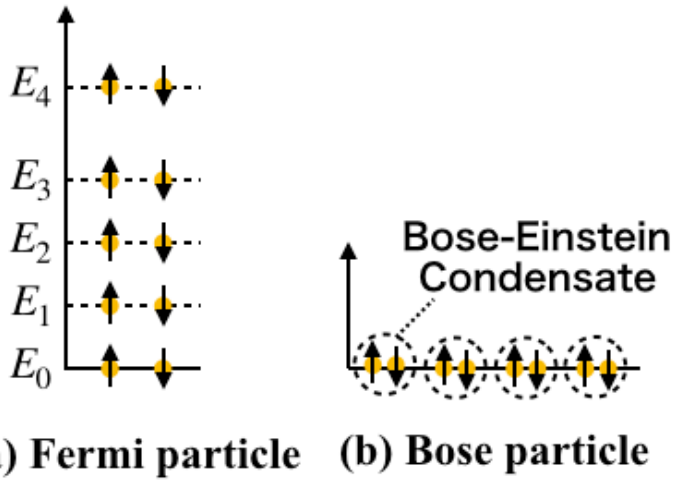

Fig. 2.2: Energy level of Fermi particle and Bose particle

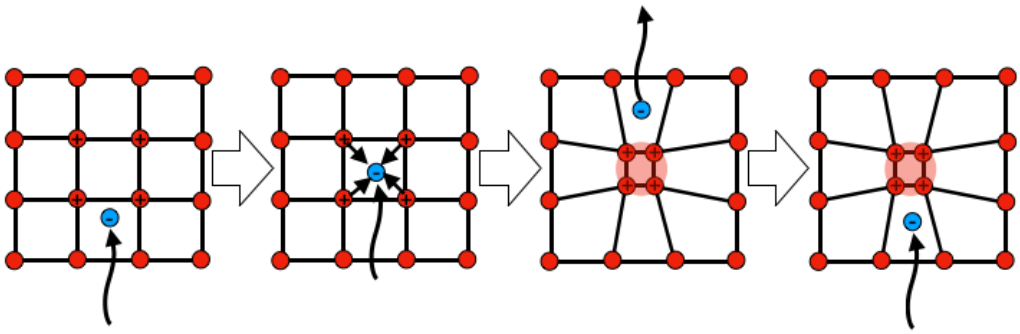

Fig. 2.3: Mechanism of forming the electron pair

1. In case an external magnetic field is applied to a superconductor in superconducting state, the interior of superconducting material remains zero magnetic field, and this condition continues even after the applied magnetic filed is removed.

2. In case an external magnetic field is applied to a superconductor in normal conducting state, then cool the superconductor to become the superconducting state with the magnetic field applied, the applied magnetic field remains even after the applied magnetic field is removed. A current is expected to induced to keep the magnetic field in interior of superconductor.

W. Meissner and R. Ochsenfeld empirically validated the magnetic field at interior of a superconductor remains zero regardless of the initial condition for external magnetic field. This phenomenon call perfect diamagnetism or Meissner effect, and indicate the characteristic that no magnetic filed remains inside the superconducting material.

The Meissner effect is explained by brothers Fritz and Heinz London using London equations expressed in Eq 2.2.

$$\mathrm{rot}\boldsymbol{J} + (\frac{n_s e*^2}{m*})\boldsymbol{B} = 0 \tag{2.2}$$

e$*and$m$*$ are the weight and electric charge of cooper pair, respectively. n_s is the number density

of superconducting carriers. At the sample time, Eq. 2.2 suggested the external magnetic field penetrates to a certain depth of superconducting material, and the London penetration depth λ is expressed in Eq. 2.3.

$$\lambda = (\frac{m*}{\mu_0 n_s e*^2})^{\frac{1}{2}} \tag{2.3}$$

where the μ_0 is permeability of free space. The London penetration depth is calculated to be $10^{-8} - 10^{-7}$ m, which is extremely thin compare to the size of the superconducting material.

However, the London theory was unveiled to be insufficient to explain the behavior of cooper pairs. B. Pippard modified the London equation, and declare the spacial propagation distance of cooper pair as Coherence length:ξ. The Coherence length is a characteristic depends on superconducting material. According to the BCS theory, the Coherence length in a superconducting material without impurity ξ_0 is expressed in Eq. 2.4

$$\xi_0 = \frac{2\hbar v_F}{\pi \nabla} \tag{2.4}$$

where the $\hbar = \frac{h}{2\pi}$ and h is Plank's constant, v_F is Fermi velocity, ∇ is the difference of free energy between the superconducting state and normal conducting state. In case the impurity exists, the Coherence length ξ can be expressed using mean free path of electron l as Eq. 2.5

$$\frac{1}{\xi} = \frac{1}{\xi_0} + \frac{1}{l} \tag{2.5}$$

The London penetration depth and Coherence length both are utilized as important parameter in orienting the superconducting condition.

2.1.3 Type I superconductor and type II superconductor

The Meissner effect can exclude the magnetic field from interior of superconducting material. However, excluding magnetic field require energy, and make the superconducting state unstable by absorb these energy. If the increment of energy overcome the difference of the energy between the superconducting state and normal conducting state, the superconductor will shift to the norma conducting state from superconducting state. The magnetic field of shifting is corresponding to the critical magnetic field, and the feature of superconducting can be verified until this magnet field.

On the other hand, and prediction for different type of magnetic characteristics was formed by L. Landau and V. Ginzburg in Ginzburg-Landau theory in 1950. The theory was improved by A. A. Abrikosov later, and the type II superconductor was confirmed, and the former superconducting was distinguished as type I superconductor. Fig. 2.4 show the difference magnetic characteristics between the type I and type II superconductor. The type I superconductor shows perfect diamagnetism until the external applied magnetic field reach the critical magnetic

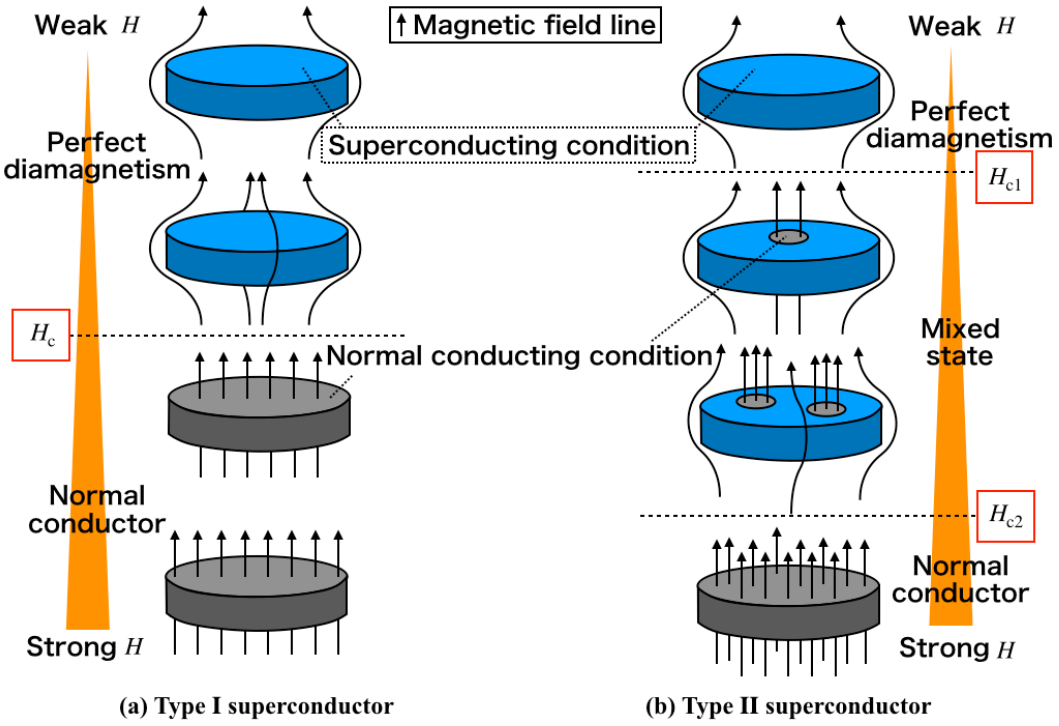

Fig. 2.4: Magnetic field line behavior in superconductor

field, and then shifts to normal conducting state beyond the critical magnetic field. By contrast, the type II superconductor shows same characteristics as weak external magnetic field. After the magnetic field increased to a certain strength, the magnetic field line start to penetrate the interior of superconductor. For the type I superconductor, keeping perfect diamagnetism require additional energy to exclude the magnetic field line. But for the type II superconductor accept the penetrating of magnetic filed line and save the energy to keep stable in superconducting state. With the increment of magnetic field strength, the penetrating magnetic filed line increased until whole area of superconductor is filled and shift to normal conducting state. The strength of magnetic field that start to penetrating the type II superconductor is called Lower critical field : H_{c1}, and the magnetic field make the type II superconductor shift to normal conducting state is called Upper critical field : H_{c2}. The definition of the type II and type II superconductor is based on the comparison between London penetrating length λ and Coherence length ξ. In case that $\xi > \lambda$ is corresponding to the type II superconductor, and the inverse correlation is the type II superconductor.

The type II superconductor has a mixed state between the H_{c1} and H_{c2}. At this state, the magnetic field line are quantized inside the superconductor and called vortex (other name : fluxoid, flux quantum) . The magmetic strength of a vortex is expressed in Eq. 2.6

$$\Phi_0 = \frac{h}{2e} = 2.068 \times 10^{-15}[Wb] \tag{2.6}$$

Where the Φ_0, h, e and the vortex, Plank's constant, and electric charge of electron.

2.1.4 Flux-flow resistance in type II superconductor

The vortex in the type II superconductor is schematic illustrated in Fig. 2.5. The current flows in y-axis direction , and the external magnetic field was applied in z axis direction, and the vortex is penetrating the superconductor in z axis direction.

The force that each vortex received is calculated as following Eq. 2.7 $\sim$ 2.10

$$\boldsymbol{B} = n\Phi_0 \tag{2.7}$$

$$\nabla \times \boldsymbol{B} = \mu_0 \boldsymbol{J} \tag{2.8}$$

$$\boldsymbol{F}_L = \Phi_0 \boldsymbol{J} \times e_z \tag{2.9}$$

$$\boldsymbol{F}_L = e\boldsymbol{E} = e\boldsymbol{v} \times \boldsymbol{B}, \ (\boldsymbol{E} = \boldsymbol{v} \times \boldsymbol{B}) \tag{2.10}$$

In case the vortex is distributed uniformly, and the number of vortex per unit length is n, the magnetic field $\boldsymbol{B}$ can be expressed as Eq. 2.7. The current $\boldsymbol{J}$ was applied as Eq. 2.8 and the Lorentz force per unit length of the magnetic field line is expressed in Eq. 2.9. Eq. 2.9 indicates the vortex received the force in the x-axis direction. The movement of the vortex calls flux-flow, and the translation of vortex in an ideal superconductor means the electron translating, and result in energy loss. $\boldsymbol{F}_L$ can be expressed using a vector as Eq. 2.10 and the electric field can be generated. This can be interpreted that even the current flow of the superconductor with zero resistance at the mixed state, the voltage drop exists. This voltage drop is considered to be electric resistance, and this electrical resistance called flux-flow resistance.

However, in fact, most of the type II superconductor does not generate electric resistance even in a mixed state. It is thought that lattice defects and impurities exist inside the actual superconductor, which hinders the movement of vortex. The effect of hindering the movement of the vortex is called a pinning effect, the force of which is called a pinning force, and the center thereof is called a pinning center. The circulating shielding current flows around the vortex ac-

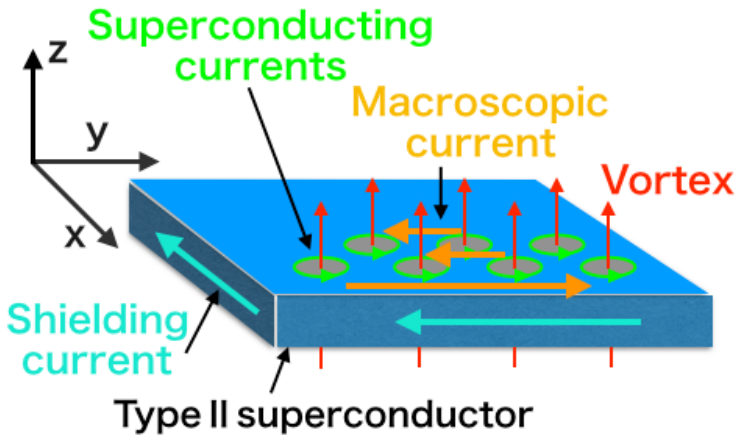

Fig. 2.5: vortex in type II superconductor

cording to the right-hand rule, and the magnetic field lines sequentially penetrate from the side of the superconductor. Considering the line in the x-axis direction of the superconductor, the side of the superconductor has more vortex than the inside of the superconductor. The current flows macroscopically can be observed due to the difference in the amount of circulating superconducting current. The Meissner current (Shielding current) flows in the negative direction of the y-axis will cancels the macroscopic current on the side-surface of the superconductor.

When the current applied to the superconductor is small, and the Lorentz force acting on the magnetic flux lines is balanced with the pinning force, no flux-flow resistance occurs. However, when the applied current increases and the Lorentz force becomes larger than the pinning force, a flux-flow occurs, and electric resistance shows up. At this time, the critical current density is a limit at which the flux-flow resistance does not occur.

2.1.5 Other electric resistances in type II superconductor

When the current flow through the superconductor or the applied external magnetic field varies with time, the vortex moves and energy loss occurs. The loss due to spontaneous movement of the vortex, which cannot be controlled from the outside, induced by the vortex being trapped or coming off the pinning center is called hysteresis loss. When the magnetic field applied to the filamentary superconductor has a temporal variation, a shielding current flows in a loop between the filaments, and a loss due to the shielding current is called a coupling loss. The hysteresis loss and the coupling loss are collectively called AC loss. Hysteresis loss can be reduced by thinning the superconductor, and coupling loss can be reduced by twisting the superconductor filaments and reducing the loops between the filaments. As described above, in order to reduce the AC loss, the superconducting wire is generally used by bundling and twisting fine wires. In addition, even when a direct current is applied, the vortex moves due to external factors such as the movement of the superconducting wire causes Joule loss The raised temperature of the superconductor increases the possibility of a magnetic flux jump. Thinning is effective in suppressing this. Therefore, currently used superconducting wires need to be thinned.

2.1.6 $I-V$ characteristics of type II superconductor

When a current is applied to the type II superconducting wire, the electric field rises gently. In such a case, the current density corresponding to $E = 1\mu\mathrm{V/cm}$ is treated as the critical current density for convenience. The electric field calculated from the condition of $E = 1\mu\mathrm{V/cm}$ is E_c. The $I-V$ characteristic around this electric field can be expressed as a power law of the equation as Eq. 2.11.

$$E = E_\mathrm{c}\left(\frac{J}{J_\mathrm{c}}\right)^n \tag{2.11}$$

This index is called n value, and a method of expressing electric field and current characteristics with such a function is called an n-value model. In a superconductor, it is said that the larger

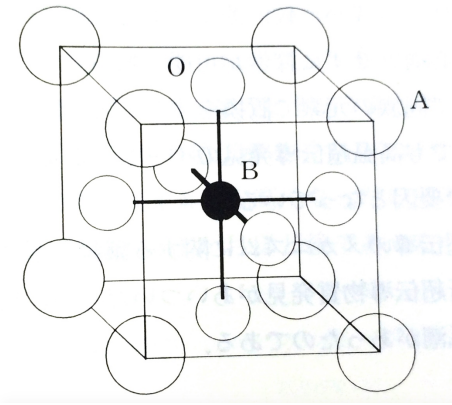

Fig. 2.6: Structure of perovskite

the n value, the better the superconducting properties. This is because the voltage can be sharply reduced by slightly reducing the current near the critical current density. Since it is difficult to directly calculate the n value as a physical quantity, it is treated as a parameter that is practically used. Generally, as the temperature and magnetic field become higher, the inhomogeneity of the critical current density becomes relatively large, so the n value decreases.

2.1.7 Copper oxides high-temperature superconductor[52]

Among the superconducting material, the copper oxides high-temperature superconductor has the highest critical temperature under atmosphere pressure nowadays. The discovery of the series of copper oxides high-temperature superconductor is date back to 1986 of La-Ba-Cu-O superconductor. And the subsequent research developed Y-Ba-Cu-O superconductor and open up a new frontier for using liquid nitrogen as coolant for superconducting material, because the critical temperature of Y-Ba-Cu-O superconductor is higher than the boiling point of liquid nitrogen(77 K) The description of high-temperature superconductor was used for these superconductor from the this stage. And the superconductor using other coolant cooler than liquid nitrogen for refrigeration is distinguished as low temperature superconductor.

The crystal structure of this promising material is called perovskite and shown in Fig. 2.6. The copper nucleus is located in the B of Fig. 2.6, Six oxygen atoms (O) form an octahedron, and the ions A bind this octahedron. In the chemical formula, it is described as ACuO3. The copper oxide superconductor takes the octahedron made of six oxygen atoms as a basic block, and shares the vertex of A with other blocks in a certain direction. The features of this structure are summarized below.

1. A site contains +2 or +3 valence of metal ions .It is easy to partially change the metal in site A.

2. The B site usually contains copper ions, which can also be partially replaced by other ions, and contains +3 to +5 valence of metal ions.

3. Scandium (Sc), Titanium (Ti), Vanadium (Ba), Chromium (Cr), Manganese (Mn), Iron

(Fe), Cobalt (Co), and nickel (Ni) were studied. These 3d transition metal enters the Cu site, an ion state with high valence is stably maintained.

4. Oxygen ion defects can be generated at high density.

5. Since the octahedron composed of ions (mainly copper ions) and oxygen at the B site is bonded to other octahedrons only at each vertex, the bond between the octahedrons is not strong and deformable. Therefore various perovskite structures exist.

6. Substitution of metal ions at A-site and B-site can greatly change the composition, so it is possible to greatly increase the physical properties of the material determined by the composition.

2.1.8 Rare Earth Barium Copper Oxide (REBCO) superconductor

Rare Earth Barium Copper Oxide (REBCO) is a kind of copper oxides high temperature superconductor and represented by the chemical formula $REBa_2Cu_3O_y$. RE123 is abbreviated name and Rare Earth indicate the material containing rare earth elements. The name of the actual material differs depending on the rare earth element used. For example, when yttrium (Y) is used, it is YBCO, and when gadolinium (Gd) is used, it is GdBCO. REBCO high-temperature superconducting wires are characterized by a high critical current density and a small decrease in critical current density even in a strong magnetic field.

The crystal structure of REBCO is shown in Fig. 2.7. The current is concentrated in the plane (ab-plane) of CuO_2, it is necessary to align the ab planes of the crystal grains in the direction of current flow in order to manufacture a wire. It is known that if the directions of the a-axis and b-axis are not aligned at the crystal grain boundaries in the ab plane, the current-carrying characteristics are degraded.

The configuration of common REBCO high-temperature superconducting wire is shown in Fig. 2.8 [53][54]. the tape is layered structure, and the Pulsed laser deposition (PLD) method and the metal organic chemical vapor deposition (MOCVD) were developed for manufacturing the REBCO superconducting material, When a superconducting substance is formed directly on a metal substrate, the constituent elements of the superconducting substance are diffused, and the superconducting properties deteriorate. Therefore, a buffer material is required between the metal substrate and the superconducting material, and this portion is called a buffer layer. The Silver layer, Tin layer, and copper layer is also called stabilizer layer. These layer is utilized for not only protecting REBCO layer physically, but also form protecting circuit for the case that applied current exceeds the critical current of REBCO superconductor. The soldered stabilizer layer was used widely, but electroplated stabilizer has been introduced for its merit on flexibility and high cost-efficiency. Therefore, the REBCO tape with electroplated stabilizer was mainly focused in this study.

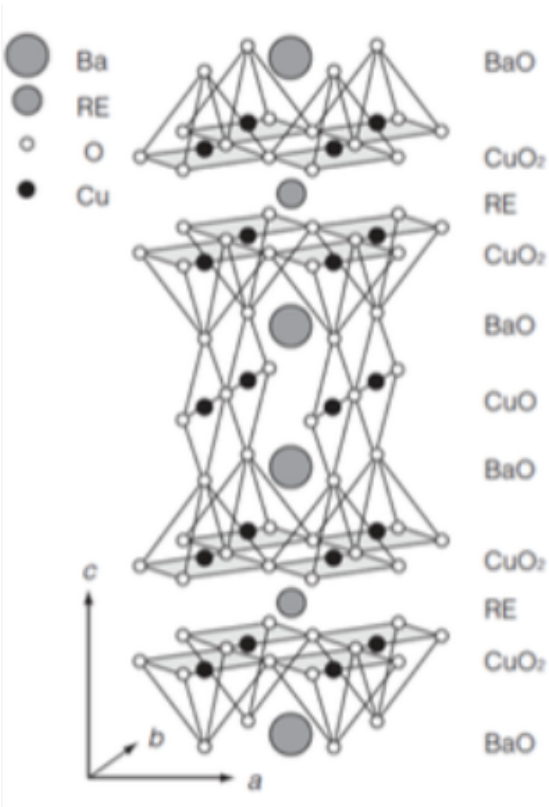

Fig. 2.7: Crystal structure of REBCO

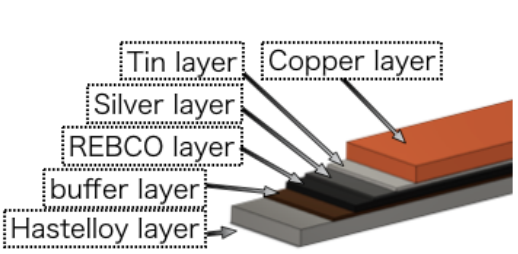

(a) REBCO tape with soldered stabilizer layers

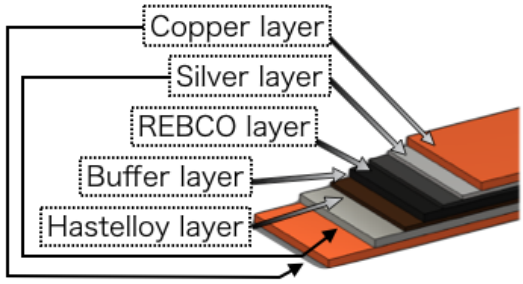

(b) REBCO tape with electroplated stabilizer layers

Fig. 2.8: Configuration of REBCO tape

2.2 X-ray Computer Tomography scan[56][62]

X-ray is a kind of electromagnetic radiation with a wavelength ranges $10^{-11} - 10^{-8}$. The X-ray is known for its excellent penetrating ability, and used in analyzing the interior structure of an object from medial to industrial frontier. When the X-ray penetrates a two-dimensional or three-dimensional object and form a projection, the acquired projection data can be used to reconstruct the shape of object. The process that the image reconstruction from projection is called tomography, and with the utilization of computer is called computer tomography (CT). The device developed for X-ray CT is called X-ray CT scanner, and the reconstructed shape of object consist of distribution of CT number. The CT number is a relative value of X-ray attenuation coefficient, and the cross section of sliced distribution form two-dimensional image as CT images.

2.2.1 Production of X-ray

The X-ray is produced by a charged particle (electrons or ions) with sufficient energy hitting a material. X-ray tube and synchrotron are the source of X-ray produced from electrons for use of applications. The X-ray CT scanner uses the X-ray tube for the production of X-ray for its size of equipment. Fig. 2.9 illustrated the common X-ray tube to explain the production of X-ray. A high voltage of was applied between the cathode and anode, and the electrons flied out from the cathode was accelerated by the electric field and collide to the anode. The X-ray photon is produced from the point of electron collision by the process of Bremsstrahlung (braking radiation) and characteristic X-ray emission explained following.

1. Bremsstrahlung

   This process is the electrons are scattered by the strong electric field form by the nucleus as "brake" and the radiation was given off to satisfy the energy conservation. The X-ray produced by this process has a continuous spectrum.

2. Characteristic X-ray emission

   This process is traced back to the electron collision on the anode material. The electron convey its energy to the orbital electron out of the inner electron shell of the atom of the anode material. The orbital electron is excited and fills the vacancies subsequently, the energy corresponding to the energy level between the orbitals are emitted as X-ray photon. Therefore the X-ray produced by this process has discrete spectrum and depends on the anode material.

The maximum energy of the produced X-ray is limited by the energy of the incident electrons, and equal to the energy that electron charged through the acceleration between cathode and anode by the applied electric field. The voltage between the cathode and anode is called X-ray

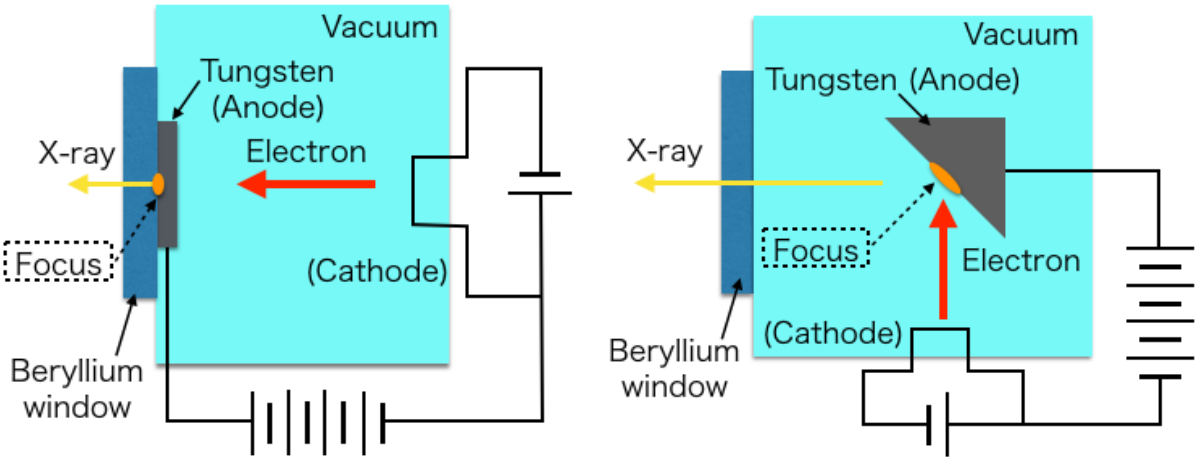

(a) Transmission-type X-ray tube (b) Reflection-type X-ray tube

Fig. 2.9: Configuration of X-ray tube

voltage, and the number of electron flied out the cathode is X-ray tube current. 160 kV of X-ray tube produces the electron is with an energy of 160 keV in the maximum and the X-ray photon as same. Therefore, the resulting X-ray output from a X-ray tube consist of a continuous spectrum falling off to zero at the X-ray tube voltage, and several spikes of characteristic X-ray. This type of X-ray is called the white X-ray, whereas the X-ray with only one energy spectrum is called monochromatic X-ray. The anode of X-ray tube called target, and the general target material is tungsten. The choice of the tungsten is because of its high atomic number to produce X-ray relatively efficiently and high melting point to tolerate the heat generation.

Considering the X-ray penetrate an object and project the image on a panel. The boundary of the projected image can be blur by the size of focus as shown in Fig. 2.10 To minimize the difference between P_{actual} and P_{ideal} for distinct projection, The size of focus need to be reduced. However, reducing the size of focus equal to concentrate the point of electron collision, and increases the temperature of target material to critical. The energy and the number of colliding electron is the also increase the temperature of target material. In the Fig. 2.9, two types of X-ray tube were illustrated. The transmission-type X-ray tube in Fig. 2.9(a) has thin target material and relatively small size of focus compare to the reflection-type X-ray tube in Fig. 2.9(b). But the higher voltage can be applied to the reflection-type X-ray tube due to is high wider electron collision point, and realize higher penetrating property.

The micro-meter order size of X-ray tube focus are realized currently[55]. The increment of X-ray tube voltage and current and reducing the size of focus form trade-off relation with the clarity of X-ray projection. The conditions of the X-ray tube are needed to be modified accordingly to the application.

2.2.2 Attenuation of X-ray

During the X-ray penetrating the material, X-ray photon interacts with the atom of the material. Three main interactions: photoelectric absorption, Compton scattering, and Rayleigh scattering

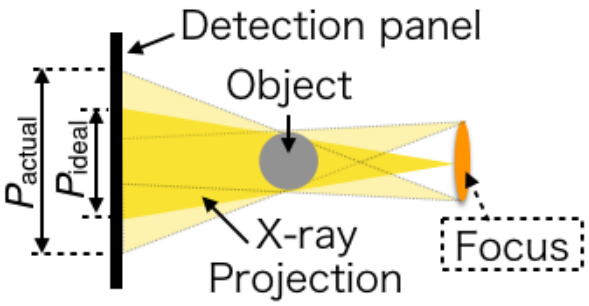

Fig. 2.10: Projection of X-ray

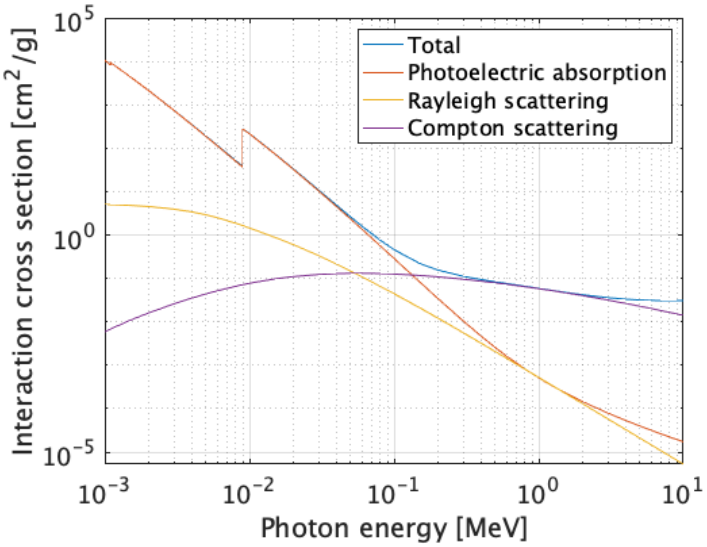

Fig. 2.11: Photon cross section of copper[60]

occurs. The photoelectric absorption is a phenomenon that the electron is emitted when a photon collided to a material. The Rayleigh scattering, or coherent scattering, is the X-ray photon elastically scattered by the atom. And the Compton scattering, or incoherent scattering, is an inelastic scattering of the X-ray photon by an out shell electron of the collided atom. The interactions was studied respectively [57]-[59], and summarized to a database [61], [60] for calculation of application. The cross section [cm^2/g] was used to evaluate the probability of the interaction. The higher the cross section is, the higher probability the interaction occurs. And the cross section depends on the energy of X-ray photon and the atomic number of interacted material. The photon cross section of copper is shown in Fig. 2.11 as an example. The Ratio of the interaction shows the photoelectric absorption is dominant interaction at the low energy of photon, then gradually transformed to the Rayleigh scattering and Compton scattering. In addition to the three interactions, pair production is another interaction caused by the photon. This interaction is generally omitted because the pair production required the minimum energy of 1022 keV, which consist of the doubled rest energy of the electron, and much higher than the range of X-ray imaging.

The cross section of photon interaction is interpreted as attenuation of photon, and the mass

attenuation coefficient μ_{m} [cm^2/g] is expressed using cross section as Eq. 2.12

$$\mu_{\mathrm{m}} = \rho \frac{N_{\mathrm{A}}}{A} (\sigma_{\mathrm{pho}} + \sigma_{\mathrm{Rayleigh}} + \sigma_{\mathrm{Compton}}) \tag{2.12}$$

ρ, N_{A}, A are density [g/cm^3], Avogadro constant (6.022×10^{23} [mol^{-1}]), and atomic mass of the material, respectively. $\sigma_{\mathrm{pho}}, \sigma_{\mathrm{Rayleigh}}, \sigma_{\mathrm{Compton}}$ are the cross section of photoelectric absorption, Rayleigh scattering, and Compton scattering. Since the cross section of interaction is depending on the energy of X-ray (E) and the atomic number (Z), the mass attenuation coefficient can be expressed as a function of E, Z. The intensity of X-ray attenuated by a material with thickness of x can be expressed using $\mu_{\mathrm{m}}(E, Z)$ in Eq. 2.13.

$$I = I_0 \exp\{-\rho \mu_{\mathrm{m}}(E, Z) x\} \tag{2.13}$$

where the I_0 is the original X-ray intensity, and the I is the attenuated X-ray intensity. Noting that Eq. 2.13 expresses the X-ray attenuation of a particular energy of X-ray in a material. Since the attenuation of X-ray photon is not the reduction of the energy but the intensity, it is reasonable to calculate the attenuated white X-ray (I_{White}) from accumulating the attenuation of each energy of as Eq. 2.14

$$I_{\mathrm{White}} = \sum_E I_0(E) \exp\{-\rho \mu_m(E, Z) x\} \tag{2.14}$$

And the attenuation of X-ray linearly increased by the thickness of penetrating material and the number of material, the white X-ray attenuated by multiple materials n can be expressed in Eq. 2.15

$$I_{\mathrm{Multi}} = \sum_{Z=1}^{n} \left[\sum_E \exp\{-\rho \mu_m(E, Z) x_Z\} I_0(E) \right] \tag{2.15}$$

Where x_Z is the thickness of each material.The white X-ray penetrated the materials I_{Multi} can be evaluated approximatively.

2.2.3 Radon transform

The projection of X-ray on an object is illustrated in Fig. 2.12. The distribution of X-ray attenuation is expressed using $f(x, y)$, and the attenuated intensity of X-ray I is expressed as Eq. 2.16

$$I = I_0 \exp\left\{ - \int_s f(x, y) \mathrm{ds} \right\} \tag{2.16}$$

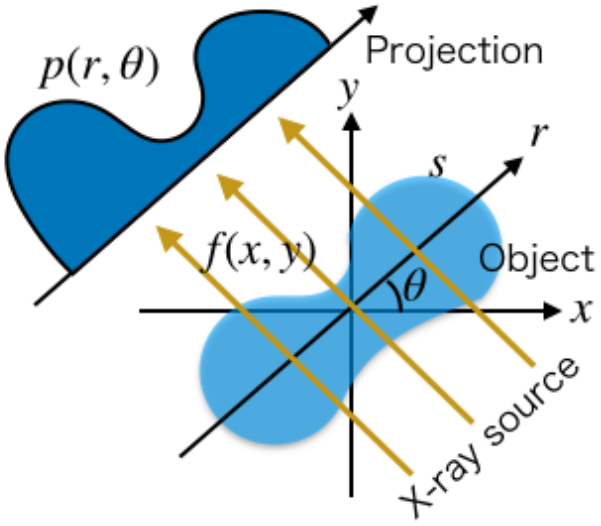

Fig. 2.12: X-ray projection of object $f(x,y)$

The ds along the direction of s, and here monochromatic X-ray is assumed for convenience. The gradient of s is

$$\begin{aligned} \frac{y}{x} &= \tan(\theta + \frac{\pi}{2}) \\ &= \frac{-\cos\theta}{\sin\theta} \end{aligned} \tag{2.17}$$

The condition $x\cos\theta + y\sin\theta = 0$ satisfy the points on line s, therefore the accumulated attenuation of one axis of X-ray can expressed using integral as following.

$$p(r,\theta) = \int_{-\infty}^{\infty}\int_{-\infty}^{\infty} f(x,y)\delta(x\cos\theta + y\sin\theta)\mathrm{dxdy} \tag{2.18}$$

Here the $\delta(\cdot)$ is the Dirac delta function. In the projection, r is also need to be considered for the projection. Parallel translation was used to consider the condition of the points need to satisfy, $x\cos\theta + y\sin\theta - r = 0$. The projection of X-ray $p(r,\theta)$ can be expressed following.

$$p(r,\theta) = \int_{-\infty}^{\infty}\int_{-\infty}^{\infty} f(x,y)\delta(x\cos\theta + y\sin\theta - r)\mathrm{dxdy} \tag{2.19}$$

The transforming the $f(x,y)$ to adapt to the $p(r,\theta)$ shown in Eq. 2.19 is called Radon transform.

Using the coordinate of $r-s$, which is rotated with angle θ from coordinate of $x-y$, the coordinate of axis is rotated as following.

$$\begin{pmatrix} r \\ s \end{pmatrix} = \begin{pmatrix} \cos\theta & \sin\theta \\ -\sin\theta & \cos\theta \end{pmatrix} \begin{pmatrix} x \\ y \end{pmatrix} \tag{2.20}$$

The projection $p(r,\theta)$ can be expressed using the coordinate of $r-s$

$$p(r,\theta)=\int_{-\infty}^{\infty} f(r\cos\theta-s\sin\theta, r\sin\theta+s\cos\theta)\mathrm{ds} \tag{2.21}$$

The expression of Eq. 2.21 is called ray-sum, and definetely equal to the Eq. 2.19.

2.2.4 Projection slice theorem

In the CT, $p(r,\theta)$ is measured in the range of $0 \leq \theta < 2\pi$, and objective is to reconstruct the $f(x,y)$. The reconstruction of $f(x,y)$ is literary inverse Radon transform. The reconstruction process can be easily explained using the two-dimensional Fourier transform. The two-dimensional Fourier transform $F(\mu,\upsilon)$ from $f(x,y)$ is expressed by Eq. 2.22

$$F(\mu,\upsilon)=\int_{-\infty}^{\infty}\int_{-\infty}^{\infty} f(x,y)\exp\left\{-j2\pi(\mu x+\upsilon y)\right\}\mathrm{dxdy} \tag{2.22}$$

Using transformation of variable of $\mu=\rho\cos\theta, \upsilon=\rho\sin\theta$ to express $F(\mu,\upsilon)$ in polar coordinate of $\rho-\theta$, Eq. 2.22 can be modified as following.

$$F(\rho\cos\theta,\rho\sin\theta)=\int_{-\infty}^{\infty}\int_{-\infty}^{\infty} f(x,y)\exp\left\{-j2\pi\rho(x\cos\theta+y\sin\theta)\right\}\mathrm{dxdy} \tag{2.23}$$

Combined with Eq. 2.20, Eq. 2.23 can be modified as Eq. 2.24.

$$\begin{aligned} F(\rho\cos\theta,\rho\sin\theta) &= \int_{-\infty}^{\infty}\left\{\int_{-\infty}^{\infty} f(r\cos\theta-s\sin\theta, r\sin\theta+s\cos\theta)\mathrm{ds}\right\}\exp(-j2\pi\rho r)\mathrm{dr} \\ &= \int_{-\infty}^{\infty} p(r,\theta)\exp(-j2\pi\rho r)\mathrm{dr} \end{aligned} \tag{2.24}$$

The interpretation of Eq. 2.24 is the following. When the projection data from angle of θ, $p(r,\theta)$, is Fourier transformed with r to P, the spectrum of P is equal to the spectrum of cross section cut from the two-dimensional Fourier transformed $f(x,y)$ with angle of θ. This equivalence called projection slice theorem. Acquiring the projection data from all angle and Fourier transform the data can generate the two-dimensional Fourier transform of the object cross section.

2.2.5 Reconstruction using filtered back-projection

As the explanation of projection slice theorem, acquiring the projection data from all angle and generating the two-dimensional Fourier transform of the object, subsequently introducing two-dimensional inverse Fourier transform can obtain the $f(x,y)$ of the object. However, due to the difference of coordinate between the Cartesian and polar, the inverse Fourier transform could not reconstruct clearly and precisely. A particular method for correction is needed.

The inverse Fourier transform of $F(\mu, \upsilon)$ is expressed in Eq. 2.25

$$f(x,y) = \int_{-\infty}^{\infty}\int_{-\infty}^{\infty} F(\mu,\upsilon)\exp\left\{j2\pi(\mu x+\upsilon y)\right\}\mathrm{d}\mu\mathrm{d}\upsilon \tag{2.25}$$

Then using polar coordinate of $r-\theta$ to substitute the Eq. 2.26 in following

$$f(x,y) = \int_{0}^{2\pi}\int_{-\infty}^{\infty} F(\rho\cos\theta,\rho\sin\theta)\exp\left\{j2\pi\rho(x\cos\theta+y\sin\theta)\right\}\rho\mathrm{d}\rho\mathrm{d}\theta \tag{2.26}$$

Them separate the range of integration by $0\sim\pi$ and $\pi\sim 2\pi$, the Eq. 2.26 can be expressed as following.

$$\begin{aligned} f(x,y) \quad = \quad & \int_{0}^{\pi}\int_{-\infty}^{\infty} F(\rho\cos\theta,\rho\sin\theta)\exp\left\{j2\pi\rho(x\cos\theta+y\sin\theta)\right\}\rho\mathrm{d}\rho\mathrm{d}\theta \\ & +\int_{0}^{\pi}\int_{-\infty}^{\infty} F\left\{\rho\cos(\theta+\pi),\rho\sin(\theta+\pi)\right\}\exp\left[j2\pi\rho\{x\cos(\theta+\pi)\right. \\ & \left.+y\sin(\theta+\pi)\}\right]\rho\mathrm{d}\rho\mathrm{d}\theta \end{aligned} \tag{2.27}$$

Considering $\cos(\theta+\pi) = -\cos\theta, \sin(\theta+\pi) = -\sin\theta, F(\rho,\theta+\pi) = F(\rho,\theta)$, and Eq. 2.20, Eq. 2.27 can be modified as following.

$$f(x,y) = \int_{0}^{\pi}\left\{\int_{-\infty}^{\infty} G(\rho)|\rho|\exp(j2\pi\rho r)\mathrm{d}\rho\right\}\mathrm{d}\theta \tag{2.28}$$

where

$$G(\rho) = \int_{-\infty}^{\infty} p(r,\theta)\exp(-2\pi\rho r)\mathrm{d}r \tag{2.29}$$

In case $Q(r,\theta)$ is introduced as following,

$$Q(r,\theta) = \int_{-\infty}^{\infty} G(\rho)|\rho|\exp(j2\pi\rho r)\mathrm{d}\rho \tag{2.30}$$

Eq. 2.28 can be substituted as following

$$f(x,y) = \int_{0}^{\pi} Q(x\cos\theta+y\sin\theta,\theta)\mathrm{d}\theta \tag{2.31}$$

According to the expansion of equations above, the reconstruction process can be interpreted as following.

1. Fourier transform the acquired projection image $p(r,\theta)$ with r as Eq. 2.29
2. Filter using $|\rho|$ and inverse Fourier transform the as Eq. 2.30
3. Back project (or superposition) the $Q(r,\theta)$ as Eq. 2.31

This reconstruction method called Filtered Back-Projection (FBP) method, and is widely introduced in the reconstruction process due to its merit in low calculation cost and fast respond

ability. The shape of filter $|\rho|$ decide the clearness of the reconstructed CT images. For instance, Ramachandran-Lakshminarayanan filter [63] and Shepp-Logan filter [64] are the general utilized in CT reconstruction process.

In practice, the X-ray beam is not parallel projected the to the X-ray detection surface as illustrated as Fig. 2.12, but more likely to be fan-beam and con-beam shape illustrated in Fig. 2.10 due to the production of X-ray. However, the theories of CT is also adaptable by arranging the angle of axis and weight coefficient in the calculation accordingly.

2.2.6 CT number

Considering the CT scanner commonly uses X-ray tube as the source of X-ray, which generate white X-ray, the X-ray attenuation coefficient from a white X-ray μ_{a} can be expressed as 2.32

$$\mu_{\mathrm{a}} = \frac{1}{\rho x} \frac{I_{\mathrm{White}}}{\sum I_0(E)} \tag{2.32}$$

and the CT number can be expressed using μ_{a} as following

$$\text{CT number} = k\mu_{\mathrm{a}} + art \tag{2.33}$$

k and art are the constant and the influence of artifact respectively. The artifact is the phantom created by reconstruction process of CT. Therefore, although the CT image indicates the distribution of material inside, the understanding of artifact is required to interpret the CT image.

2.3 Bolt tightening[65]

When the bolt is fastened, the axial force $F_{\mathrm{A}}$is applied according to the torque T as expressed in Eq. 2.34.

$$T = KdF_{\mathrm{A}} \tag{2.34}$$

where K is torque coefficient, and d is a nominal diameter of the bolt. The torque coefficient is affected and varied by lubrication condition and configuration of thread. Eq. 2.35 expresses the correlation between the torque coefficient and these environments.

$$K = \frac{1}{2d}\{d_2(\frac{\mu_{\mathrm{th}}}{\cos\alpha} + \tan\beta) + \mu_{\mathrm{n}} \cdot d_{\mathrm{n}}\} \tag{2.35}$$

In the equation above, μ_{th} and μ_{n} are the friction coefficients at thread and seat,d_2 and d_{n} are the effective diameters of thread and seat, α and β are the flank angle and the lead angle of the thread. Fig. 2.13 indicates the location of the aforementioned parameters. where the D and d_{H} are the outer and inner diameter of the seat, and $d_{\mathrm{n}} = \frac{2}{3} \cdot \frac{D^2 - d_{\mathrm{H}}^3}{D^2 - d_{\mathrm{H}}^2}$. The regular value of the torque coefficient with lubrication oil ranged from 0.14 to 0.26 and averaged 0.20. Since the lubrication oil was not used in consideration of workability, the torque coefficient possibly tends to increase due to the increment of friction. Considering controlling the range of torque coefficient is deflected from the main objective but arduous, the regular value of the torque coefficient was used, and the variation of torque coefficient was considered in the discussion of the result.

The applied pressure, P_{joint}, at the joint is calculated as the following equations

$$\begin{aligned} P_{\mathrm{joint}} &= \frac{F_{\mathrm{A}} \times n}{S} \\ &= \frac{\frac{T}{Kd} \times n}{S} \end{aligned} \tag{2.36}$$

where n, S are the number of bolts, the cross section area of pressuring, respectively. The number of bolts was decided from the mechanical property of the bolt. Following the torque

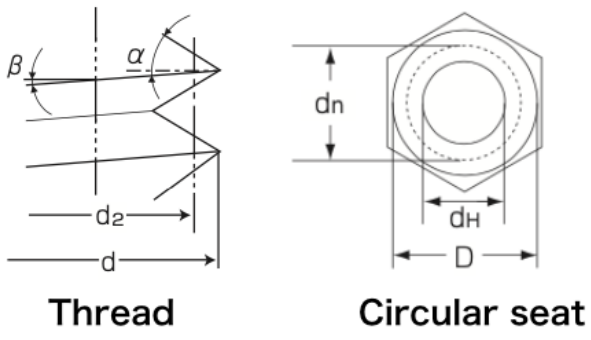

Fig. 2.13: Fabrication of single lap joint sample with 4-mm-wide REBCO tape

control method of bolt tighening, the maximum axial force of each bolt was set to 70% of strength, which is under elastic deformation. The strength classification of the stainless bolt we used was 12.9, and the strength was $1200 \times 0.9 = 1080[\mathrm{N/mm^2}]$, the axial force applied to each bolt was limited to $756[\mathrm{N/mm^2}] \times S_{\mathrm{A}}[\mathrm{mm^2}]$, where S_{A} is effective cross-section area of the bolt.

3 Application of electrical characteristics evaluation

3.1 Objective

To develop an evaluation technique for the contact resistance from electric characteristics, the correlation between contact resistance at cryogenic temperature and that at room temperature was evaluated. The evaluation is processed in three steps as follows.

1. Evaluated the correlation between joint resistance at cryogenic temperature and electric characteristics at room temperature experimentally

2. Analyzing the reason for the correlation acquired above from the behavior of the current using numerical simulation.

3. Remediating the measurement method for improving the evaluation using electric characteristics measurement.

The single-layer lap joint sample fabricated with REBCO tapes with two different stabilizer layers: solder stabilizer layers and electrolyzed stabilizers were utilized for discussion. The micro air gap existed at the contact surface was considered to be the cause of the increment of joint resistance, and the alternating current was considered to pass these micro air gaps and form a capacitor. Based on these hypotheses, the electrical impedance of the joint at room temperature was measured and discussed with the joint resistance at cryogenic temperature. Subsequently, the current path at the joint was evaluated using the finite element method numerical simulation to interpret the correlation acquired above. The exaggerated poor contact conditions like a wide area of air gap existed at the contact interface were simulated to evaluate the influence of the contact conditions on the electrical resistance at cryogenic temperature and room temperature. With the acquired knowledge from empirical and simulation results, the remediation method for improving the evaluation of the contact resistance was proposed, and applicability was discussed using numerical simulation.

3.2 Evaluation for correlation between joint resistance at cryogenic temperature and electrical impedance at room temperature

3.2.1 Preparation of single layer lap joint sample

The fabrication of the single-layer joint sample and the compositions of the REBCO tapes with two typical compositions were illustrated in Fig. 3.1. The REBCO tapes are 5-mm-wide copper-stabilized REBCO tapes (FYSC-SC05, Fujikura Ltd., Tokyo, Japan) and 4-mm-wide copper-stabilized REBCO tapes (SCS4050-AP, SuperPower Inc, Schenectady, NY, USA, I_c : over 91 A at 77 K and self-field). The compositions and the thicknesses of the REBCO tapes: layers from the top to the bottom are shown in Fig. 3.1, respectively. The copper surface at the top of the REBCO tapes at the joint section was ground using sandpaper with an abrasive particle diameter of 81 µm. Then the surface was cleaned with ethanol. And a 100-µm-thick indium foil was also cleaned using ethanol in advance to the joining

The pressure for joining was applied by bolting. The bolts with 5 mm diameter were used, and the number of bolts was four. The required torque was calculated using Eq. 2.36, and was applied by two steps: fist the half of the required torque and then requred torque, to steadily apply the pressure. The pressure was applied at room temperature for 1 minute, then the pressure was released, and acrylic plates were used to sandwich the joint sample to save the sample from accidentally breaking. The pressure of less than 6.67 MPa was applied by the acrylic plates to hold the sample. Fifteen joint samples with REBCO tapes from Fujikura Ltd. were fabricated, whereas 18 joint samples with REBCO tapes from Super Power Inc. were fabricated. The joint samples were denoted as lot Fuji and lot SP for distinguishing.

3.2.2 Experimental set up

To compare the electrical characteristics at cryogenic and room temperature empirically, the joint resistance and each joint sample were measured first, then the electrical impedance was measured. The reason for measuring impedance is the electrical impedance contained the information of electrical resistance, and try-on of the alternating current measurement catch the feature of poor contact condition. Fig. 3.2 shows the experimental set up for joint resistance with a joint sample from lot Fuji. The measurement is conducted with the four-terminal method. The two terminals that were used to measure voltage were set on both REBCO tapes that straddle the joint, with a separation distance of approximately 20 mm. Currents up to 50 A (0, 10, 20, 30, 40, and 50 A) were applied for the sample from lot Fuji, whereas 25 A (0, 5, 10, 15, 20, 25) for the samples from lot SP. The regulated DC power supply (GP035-300R, Takasago Ltd, Tokyo, Japan)was used for energizing, and voltage was measured using a digital multimeter

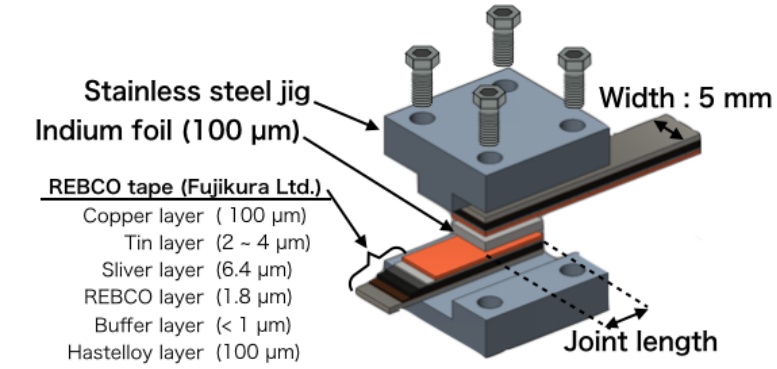

(a) Single layer lap joint using REBCO tapes from Fujikura Ltd.

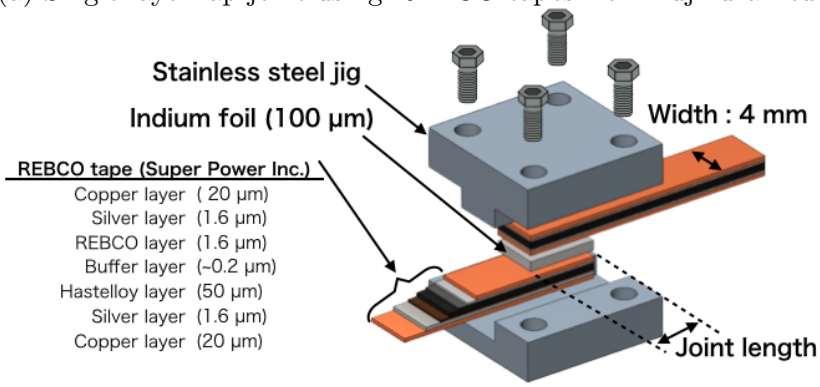

(b) Single layer lap joint using REBCO tapes from Super Power Inc.

Fig. 3.1: Fabrication of single layer lap joint sample with narrow-width REBCO tapes

(2742, Keithley). The joint resistance was evaluated by applying the least-squares approach to the measured $I - V$ curve. Each sample was soaked into liquid nitrogen (77 K) and then energized.

The electrical impedance was measured using LCR meter (ZM2371, NF Corp., Yokohama, Japan) with a frequency range from 1 Hz to 3 kHz and an impedance analyzer (ZA5405, NF Corp., Yokohama, Japan) with a frequency range from 20 Hz to 10 kHz. The measurement of LCR meter used the four-terminal method with bridge-circuit, and that of impedance analyzer used a four-terminal pair method to guarantee the accuracy of the electrical impedance. Fig. 3.3 shows the experimental set up for the measurement. The jig was processed by acrylic to prevent unnecessary electromagnetic noise caused by surrounding metallic material. The

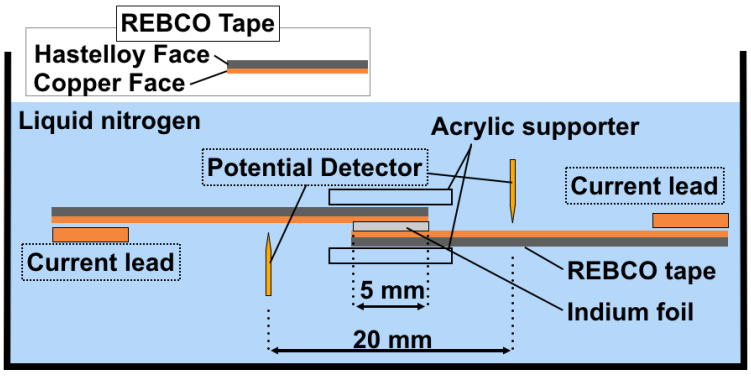

Fig. 3.2: Joint resistance measurement

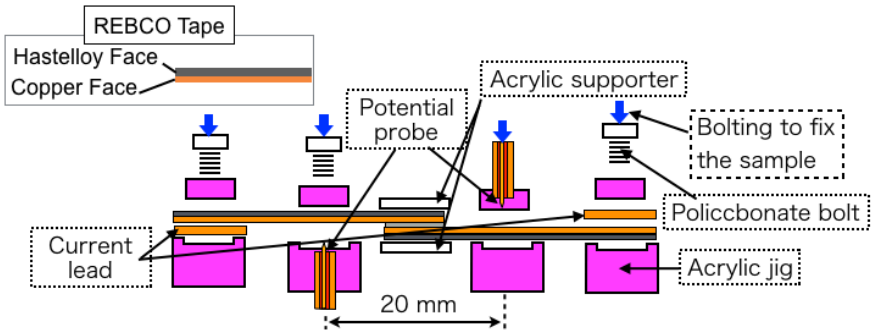

(a) Method to hold the sample

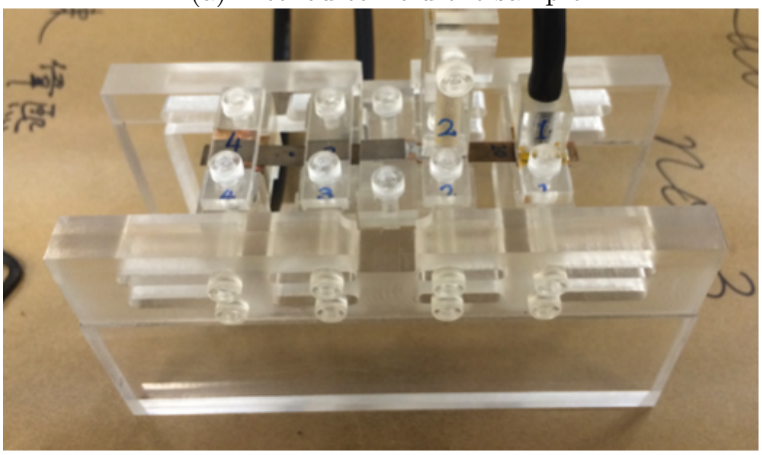

(b) Actual jig

Fig. 3.3: Electrical impedance measurement set up

distance between the potential probes was 20 mm, and the potential probes and current leads are connected with the measurement equipment using coaxial cable. Fig. 3.4 shows the appearance of the measurement. The electrical impedance of each sample was measured three times to confirm the error of measurement.

3.2.3 Result and discussion

The measured $I - V$ curve of the joint sample area shown in Fig. 3.5 The joint resistance was calculated from the gradient of the $I - V$ curve using the least-squares approach, and the

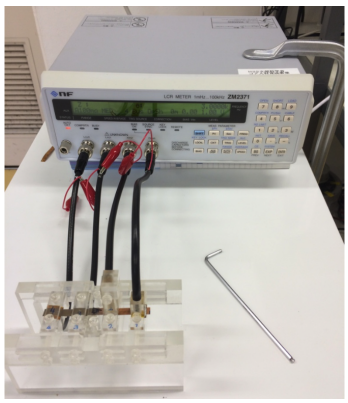

(a) Measurement using LCR meter

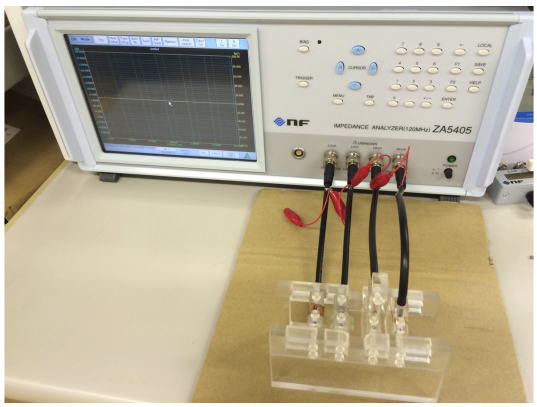

(b) Measurement using impedance analyzer

Fig. 3.4: Experimental set up for impedance measurement

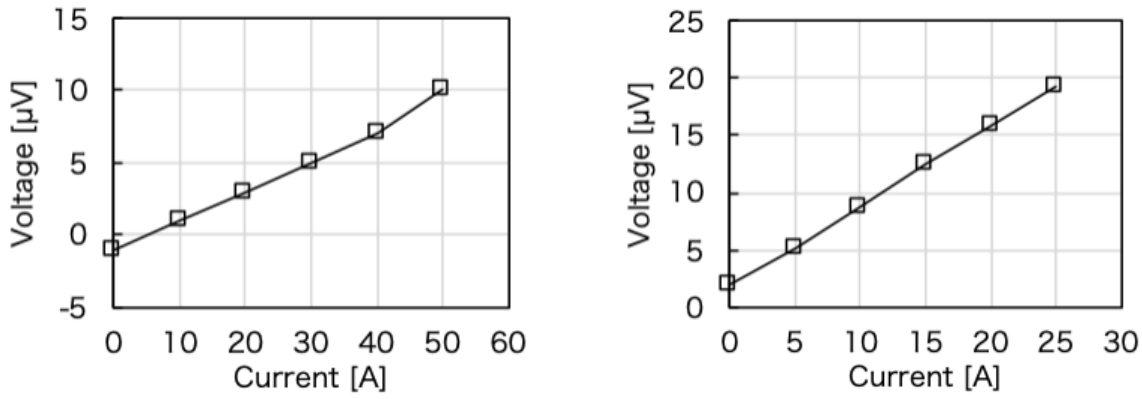

(a) Fuji1 (b) SP1

Fig. 3.5: Measured $I-V$ curve of single-layer lap joint sample

Table. 3.1: Joint resistance of narrow-width single layer lap joint sample

Sample name	Joint resistance (μΩ)	Joint resistivity (pΩm^2)	Sample name	Joint resistance (μΩ)	Joint resistivity (pΩm^2)
Fuji 1	0.30	7.50	SP 1	0.70	13.98
Fuji 2	0.22	5.38	SP 2	0.36	7.10
Fuji 3	0.25	6.25	SP 3	0.28	5.58
Fuji 4	0.26	6.50	SP 4	0.32	6.32
Fuji 5	1.15	28.85	SP 5	0.37	7.48
Fuji 6	1.21	30.25	SP 6	0.39	7.76
Fuji 7	0.32	8.00	SP 7	0.59	11.74
Fuji 8	1.15	28.75	SP 8	3.12	62.14
Fuji 9	0.48	12.00	SP 9	0.82	16.40
Fuji 10	1.39	34.75	SP 10	0.82	16.40
Fuji 11	1.81	42.25	SP 11	0.31	6.22
Fuji 12	0.48	12.00	SP 12	0.28	5.66
Fuji 13	0.62	15.40	SP 13	0.59	11.78
Fuji 14	1.10	27.50	SP 14	0.32	6.44
Fuji 15	0.80	20.00	SP 15	0.38	7.58
			SP 16	0.32	6.24
			SP 17	0.45	8.98
			SP 18	0.90	18.00

result of joint resistance was listed in Table 3.1. The joint resistivity was simply calculated by multiplying the joint resistance with the joint area (REBCO tape width × Joint length).

The frequency dependence of the impedance Fuji 1 and SP1 are shown in Fig. 3.6. In case the electrical characteristic like capacitor existed at the and the current pass it, the current path is expected to form a parallel circuit with a resistor and capacitor. Then some features like resonance frequency can be expected to be observed in the frequency dependence. However, the result without resonance frequency indicated no feature of electric composition like capacitor and inductor exist. The increment of impedance at the high-frequency range is considered to result from the skin effect of the alternate current. The current passes the joint parallel to the contact interface following the simulated path is also an interpretation for this result. Since the measurement error at high frequency tends to be larger, the impedance at low frequency was discussed further.

The impedance at room temperature in a frequency of 500 Hz was extracted for comparing. Fig. 3.7 shows the impedance composition of all single lap joint samples. Noting that since the

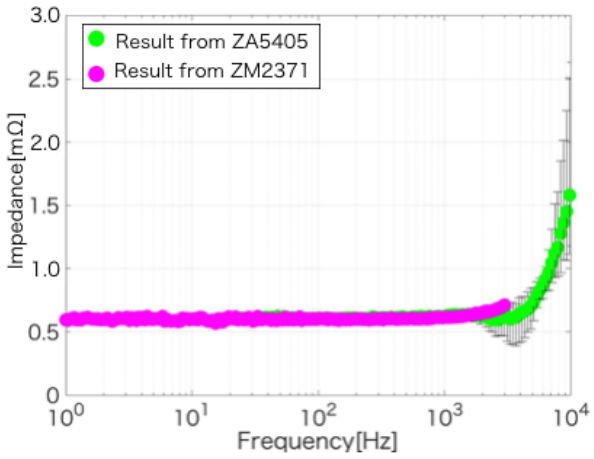

(a) Impedance of Fuji1

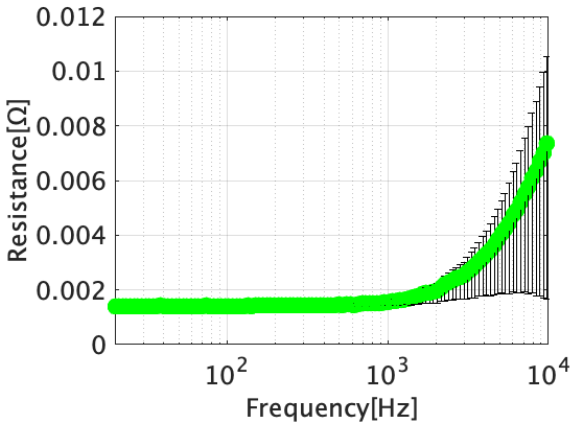

(b) Impedance of SP1

Fig. 3.6: Frequency dependency of impedance

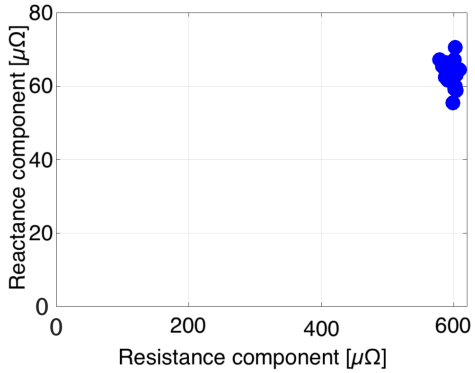

(a) Impedance composition from lot Fuji

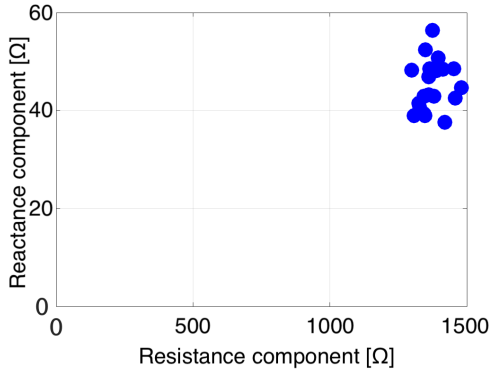

(b) Impedance composition from lot SP

Fig. 3.7: Composition of impedance at room temperature in a frequency of 500 Hz

thickness of copper layer from lot SP is thinner than that from lot Fuji, the resistance from lot SP is larger than that from lot Fuji. The resistance composition account for the most part of impedance, the resistance component of each sample was extracted and compared with joint resistance at cryogenic temperature.

Fig. 3.8 Shows the comparison between the joint resistance at cryogenic temperature and electrical resistance at room temperature, which is the component of resistance from the measured impedance. The result shows even the sample with high joint resistance at cryogenic temperature has the electrical resistance at room temperature as same as that with low joint resistance. The measurement error range and the actual variation of contact resistivity at the contact interface make it even difficult to distinguish the joint resistance at a cryogenic temperature from electrical resistance at room temperature. Contrary to the expectation, no correlation between cryogenic temperature and room temperature could be confirmed for both type of REBCO tape. The reason for this result is need to be unveiled and appropriate remediation need to be considered.

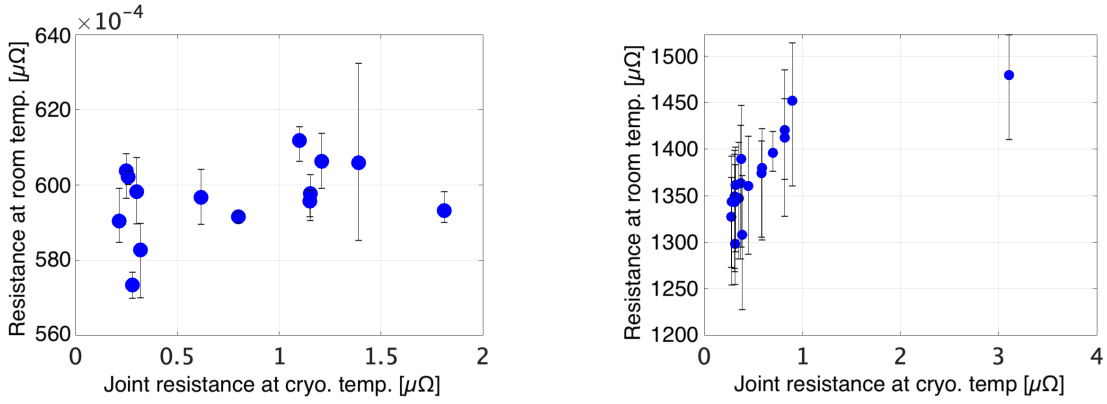

(a) Correlation with lot Fuji (b) Correlation with lot SP

Fig. 3.8: Correlation between joint resistance at cryogenic temperature and resistance at room temperature

3.3 Analysis for the correlation between the joint resistance at cryogenic temperature and electrical impedance at room temperature using numerical simulation

3.3.1 Current distribution analysis

To analyze the reason of acquired correlation between the joint resistance at cryogenic temperature and electric impedance at room temperature, a joint was modeled numerically as shown in Fig. 3.9. The current distribution at the joint section was analyzed with 2-dimension finite element simulations. A commercial software, COMSOL Multiphysics version 5.2 with the AC/DC module was used for calculating the electrical potential formulation. The model was meshed with tetrahedral element, and government equation is $\nabla \cdot (-\sigma \nabla \phi) = 0$. In the model, the compositions out of the buffer layer in REBCO tape were omitted. This is because the relatively high electrical resistivity and geometry of buffer layers insulate the current enough to be ignored. In addition to the existed material layers, the contact resistance was modeled by adding an imaginary resistance between the indium foil and the copper layer of REBCO tape. Although modifying the boundary between the indium foil and copper layer was a solution to model the contact resistance, this was not acceptable because the calculation for the electrical resistance required surface integral later.

The electric resistance of the REBCO layer at cryogenic temperature is almost zero, whereas that at room temperature is as high as an electric insulator. Therefore, the current was expected to flow mainly in the REBCO layer at cryogenic temperature but other metallic layers at room temperature. The boundary conditions and electric resistivity of materials are needed to adjust accordingly. To simulate the current mainly flow the REBCO layer at cryogenic temperature, the electrical potentials at the REBCO layers at two REBCO tapes were set. The electrical potential at the edge of copper layers was varied to simulate the current flows of the metallic layers at room temperature. The thickness of the modeled layer and the electrical resistivity of

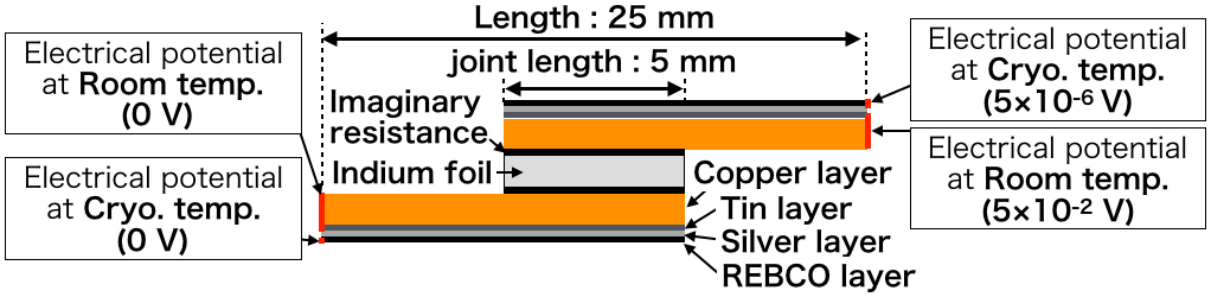

Fig. 3.9: 2-dimensional simulation model of the single layer lap joint

each material were listed in table 3.2. The practical contact resistivity at cryogenic temperature was 0.5 pΩm^2, according to the previous study. And contact resistivity of 3.25 pΩm^2 at room temperature was extrapolated from this value. The electrical resistivity of imaginary resistance was calculated by dividing the thickness from the contact resistivity.

Table. 3.2: Material properties of each composition

Composition name	Thicknesses of lot Fuji (µm)	Thicknesses of lot SP (µm)	Resistivity at room temperature ($\times 10^{-8}$ Ωm)	Resistivity at room temperature ($\times 10^{-8}$ Ωm)
Indium	100.0	100.0	8.40	1.67
Contact resistance	1.0	1.0	325.00	50.00
Copper	100.0	20.0	1.68	0.21
Tin	3.0	0	10.9	2.25
Silver	6.4	2.0	1.59	0.27
REBCO	2.0	2.0	1×10^8	1×10^{-2}

The simulated current distribution of a single-layer lap joint from lot Fuji is shown in Fig. 3.10. Two location of the joint were focused, and the potential distribution and current path were shown using surface color and streamline respectively. In cryogenic temperature, the current flows to the REBCO layer until the edge of the joint, then passes the joint and reach the REBCO layer of the other REBCO tape. The direction of current flowing the joint is perpendicular to the contact interface. From this direction, we could predict that if the contact interfaces have poor conditions like an air gap, the current flow would be disturbed and result in an increment of resistance. On the other hand, the current at room temperature shows a totally different direction of flow. When the current reaches the joint section, the current will diffuse to all layers of the metallic layer. Then the direction of the current at the center of the joint is parallel to the contact interface. This tendency indicates in case the contact interface has an air gap at the edge of the joint, the current will be disturbed. In case the air gap existed at the center of the joint, the current flows next to the air gap, and no current disturbance will happen. Therefore the resistance would not be increased. The same tendency of current distribution could be found from the lot SP as shown in Fig. 3.11.

The reason for the difference in current distribution is considered to be the contrast of electrical resistivity. The superconducting material has extremely low electrical resistivity compared to other metallic material. The current would flow the path that was resulting in the lowest electrical resistance. Because current flowing the REBCO layer generated almost no resistance, the current will flow the REBCO layer as long as possible and take the shortest distance to pass the joint to reach the REBCO layer of the other REBCO tape. Therefore, in the superconducting situation, i.e., cryogenic temperature, the current would pass the contact interfaces vertically. On the other side, the current will pass the conductor with the most significant cross-section, or the lowest electrical resistance at room temperature. When the current reached the edge of the joint section, the cross-section perpendicular to the contact interface is reasonable to lower the electrical resistance at joint unless the current resistance is exceptionally high to pass the

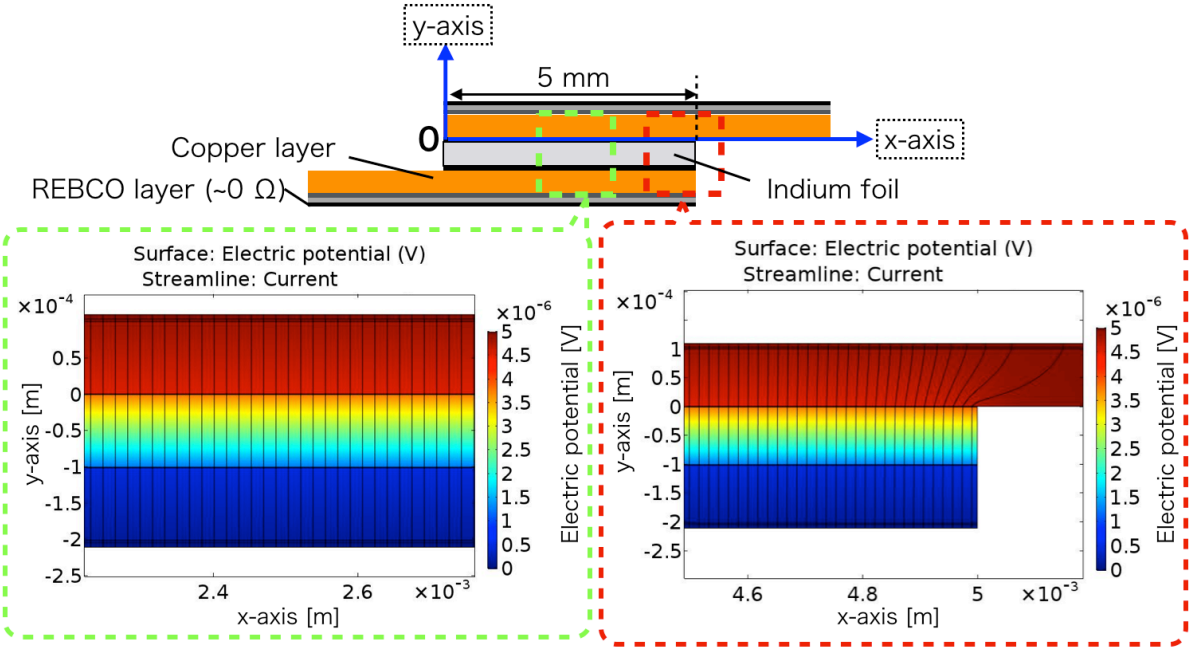

(a) Current distribution at cryogenic temperature

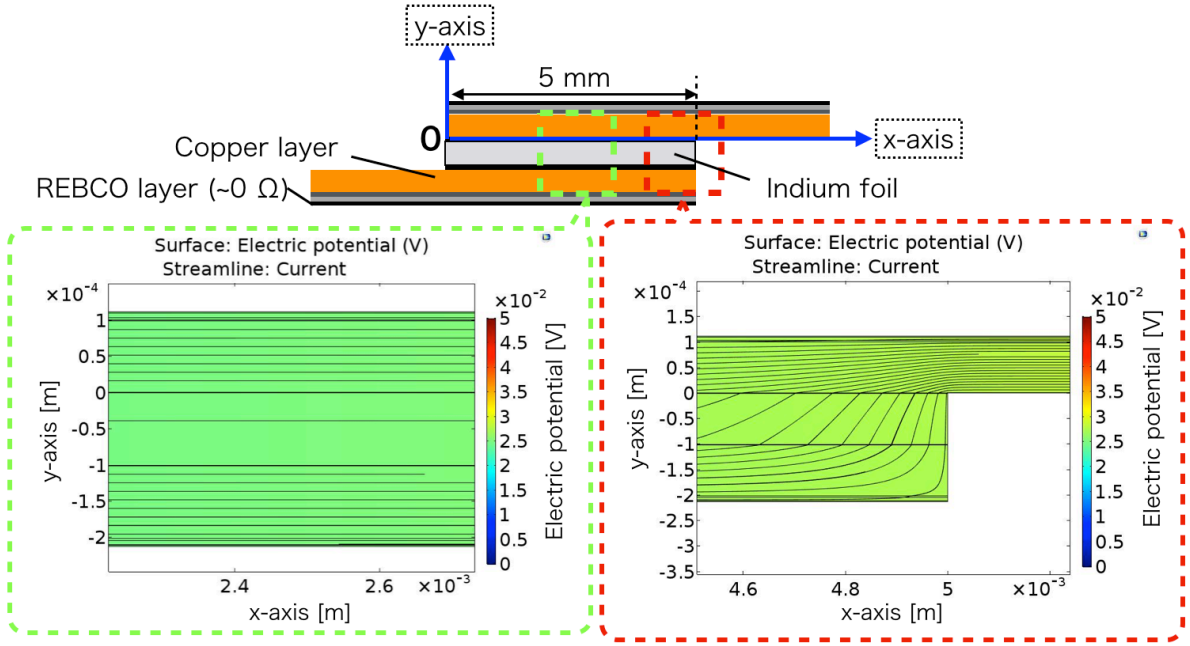

(b) Current distribution at room temperature

Fig. 3.10: Current distribution of single layer lap joint sample from lot Fuji

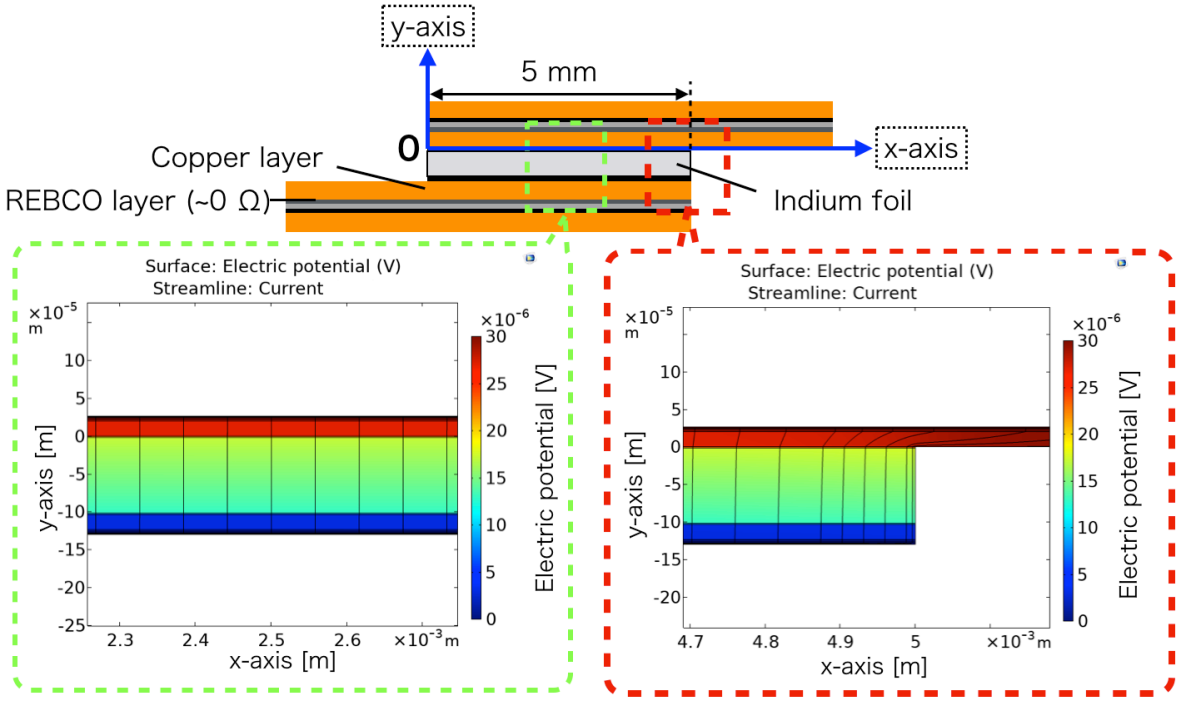

(a) Current distribution at cryogenic temperature

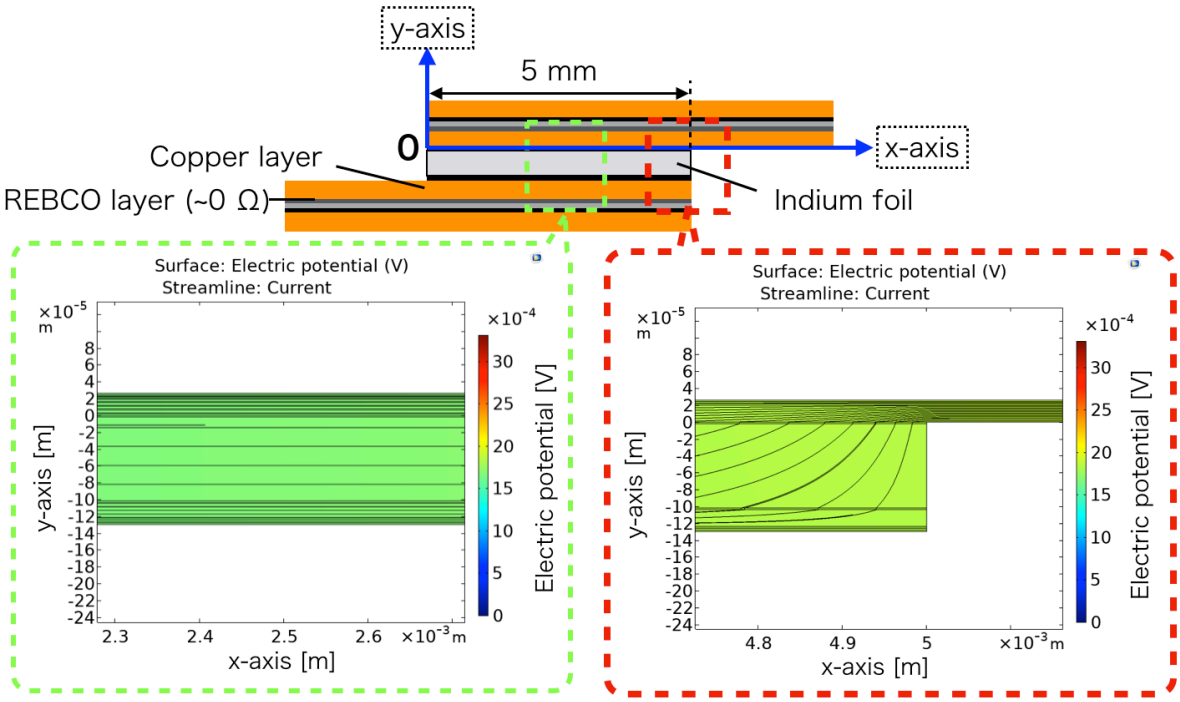

(b) Current distribution at room temperature

Fig. 3.11: Current distribution of single layer lap joint sample from lot SP

current. The condition of contact resistance at room temperature was enlarged to 1000 times to simulate the exceptionally high resistance contact condition. Fig. 3.12 shows the current distribution with contact resistivity of $3.25 \times 10^{-12}\Omega\mathrm{m}^2$ and $3.25 \times 10^{-9}\Omega\mathrm{m}^2$, corresponding to contact resistivity of $0.5 \times 10^{-12}\Omega\mathrm{m}^2$ and $0.5 \times 10^{-9}\Omega\mathrm{m}^2$ at cryogenic temperature. The direction of current passing the contact interface approaches to the vertical at the current distribution with 1000 times enlarged contact resistance demonstrated the effect of the contrast of electrical resistivity.

3.3.2 Simulated correlation between joint resistance at cryogenic temperature and electrical resistance at room temperature

Based on acquired simulation results, a correlation between joint resistance at cryogenic temperature and electrical resistance at room temperature can be evaluated. The joint resistance and electrical resistance of the model, R, can be calculated from the total generated heat of the joint, Q, using Eq. 3.1

$$R = \frac{V^2}{Q} \tag{3.1}$$

Where V is applied electrical potential, and Q is surface integration of the generated energy density of the joint. The contact resistivity was swept from 0.50 to 12.00 pΩm with an interval of 0.50 pΩm at cryogenic temperature model, while from 3.25 to 7.80 pΩm with an interval of 3.25 pΩm at room temperature model. The The voltages applied to the boundary condition was as same as shown in Fig. 3.9. The correlation between calculated joint resistance and electrical resistance from two different temperatures is shown in Fig. 3.13. The ideal correlation is the amount of change of two resistances is large enough to measure, so the change of joint resistance at cryogenic temperature can be predicted from the measurement of electrical resistance at room temperature. In the simulated result, the change of joint resistance was 0.92 µΩ, while the change of electrical resistance at room temperature was 16 µΩ. In the cryogenic temperature, tens of ampere of current can be applied, so the difference of voltage at tow ends of the joint can be µΩ order. In the room temperature, hundreds of mA of current can be applied, and the voltage can also be expected to be µΩ order. Although both voltages are under the range of measurable from the simulation, the error of measurement was large enough to exceed the difference caused by the contact resistance as shown in the empirical result in Fig. 3.7. The non-uniform distributed contact resistivity at the contact interface in the simulation model probably different in the actual sample is also considered as the cause of electrical resistance variation. A poorer contact condition was simulated to evaluate the influence of the non-uniform distributed contact condition to check the ability of electrical characteristics evaluation.

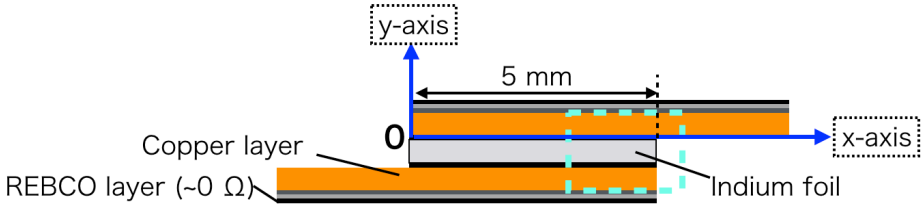

(a) Location of focus

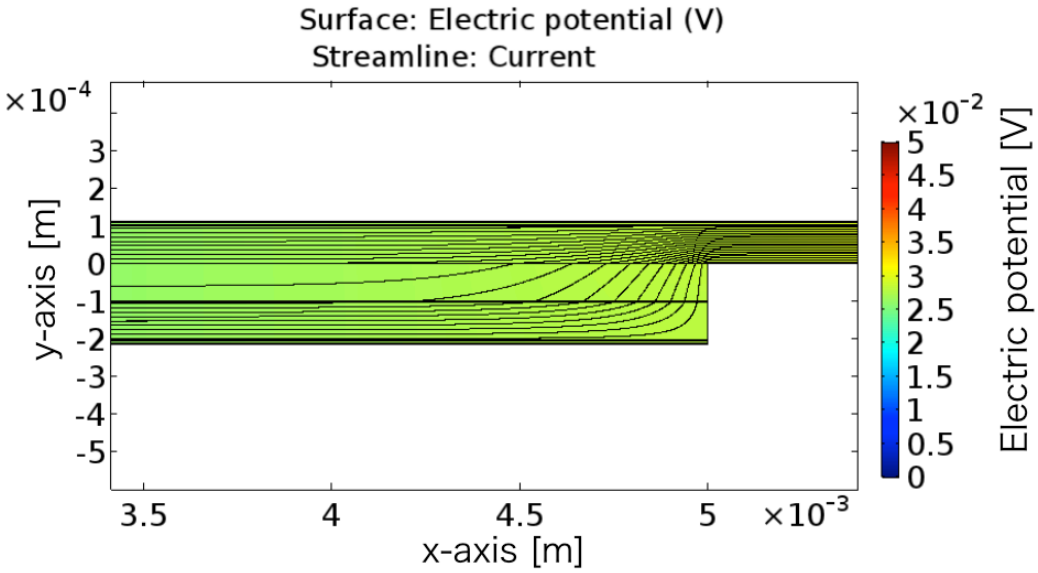

(b) Current distribution at a contact resistivity of 3.25 $\times 10^{-12} \Omega m^2$

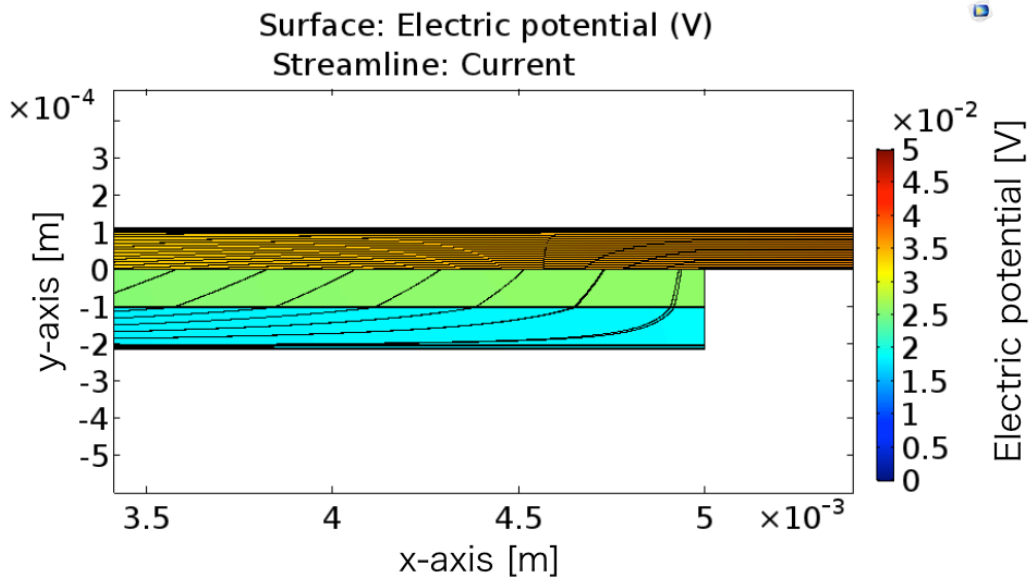

(c) Current distribution at a contact resistivity of 3.25 $\times 10^{-9} \Omega m^2$

Fig. 3.12: Current distribution variation with modification of contact resistance at room temperature

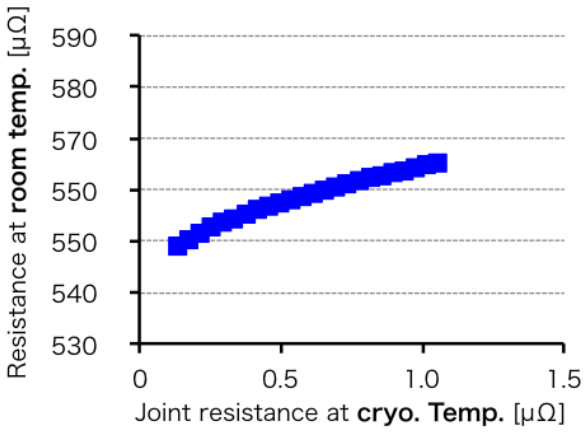

Fig. 3.13: Simulated correlation between joint resistance and electrical resistance

3.3.3 Electrical resistance variation at room temperature depended on contact condition

A model using insulating conditions to simulate a wide area of air gap existing in the contact interface was constructed. Fig. 3.14 shows the geometry of the modeled insulator based on a single-layer lap joint from lot Fuji.

A certain area at imaginary resistance was set as an insulator, electric resistivity is extremely high as one Ωm, to simulating poor contact conditions like air gap. The location and the length of insulator was swept to evaluate its influence. The insulator location was swept from 0.1 to 2.0 mm at an interval of 0.1 mm, and the simulated insulator length was 0, 0.5, 1.0, 1.5, 2.0 mm.

The evaluated electrical resistance at cryogenic temperature (joint resistance) and room temperature was shown in Fig. 3.15 respectively. In the former, the length of the insulator significantly influenced the joint resistance, but the location of the insulator shows the inapparent influence on the joint resistance. The current passing can explain this. The current pass the contact interface vertically was hampered by the poor contact condition, and disturbed current path increased the resistance. In the latter, the location of the insulator shows a slight influence on the electrical resistance, and the closer the insulator approach the edge of the joint, the more the electrical resistance increased. This could be explained by the current diffused at the edge of the joint section, and the direction of current at the edge was almost perpendicular to the contact

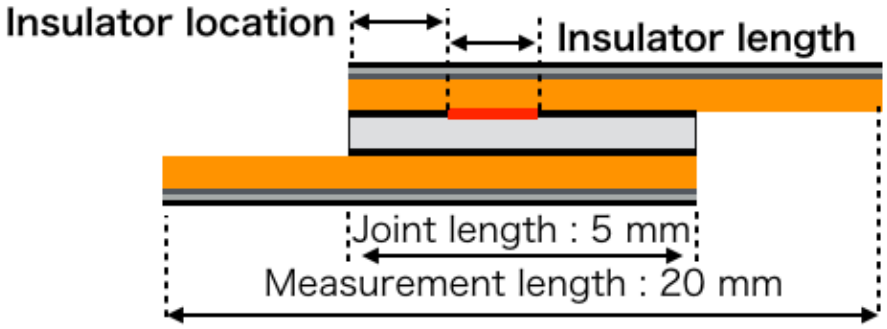

Fig. 3.14: Simulation model of variating contact condition at single layer lap joint

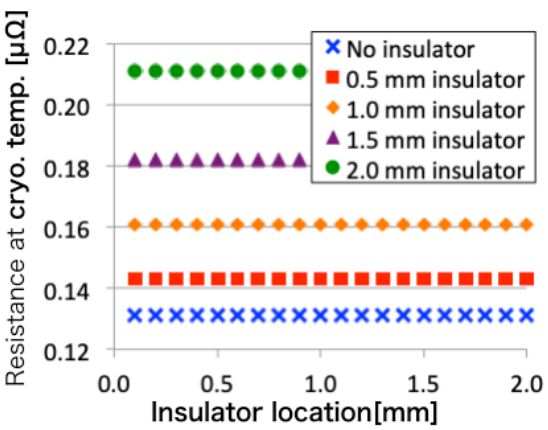

(a) Joint resistance variation at cryogenic temperature

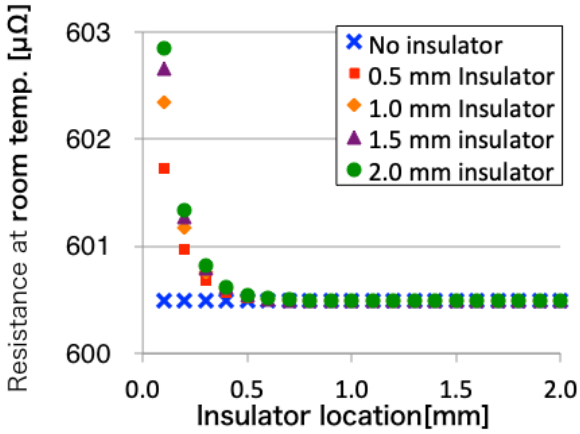

(b) Electrical resistance variation at room temperature

Fig. 3.15: Variation of electrical characteristics by virtual air gap

interface, which would be hampered by the insulator. In case the insulator existed at the location of more than 0.5 mm, the electrical resistance shows no difference between the different length of the insulator. This is because the current here flows parallel to the contact interface, and would no be influenced by the poor contact condition. The aforementioned simulation result indicated the poor contact condition would increase the joint resistance at cryogenic temperature, but could not increase electrical resistance at room temperature. Evaluating contact condition at cryogenic temperature from room temperature seems extremely difficult.

3.3.4 Consideration in remediation of current application method using numerical simulation

In the previous subsection, we conclude predicting the joint resistance at a cryogenic temperature from room temperature is difficult due to the current path with the same measurement set up. Another idea came up with intentionally generating current disturbance by inducing current perpendicular to the contact interface at room temperature. In case the current could pass the contact interface vertically at room temperature, the effect of current disturbance caused by the contact interface is expected to be detectable, and subsequently the contact resistivity at cryogenic temperature become predictable. To induce the current perpendicular to the joint surface, applying the current from the side of the joint, as shown in Fig. 3.17 was considered. This application could be realized by wire-bonding technology with tens of micrometer diameter metallic wires. To evaluate the applicability of this idea, the simplified 3-dimension joint, of which the copper layers sandwiches the indium foil, was modeled. The existence of apparent poor contact condition was simulated using insulating condition, and these area can be considered as air gap in the real. The detectability of this insulation area was evaluated using the thought-up method.

The commercial finite element method numerical analysis software COMSOL Multiphysics version 5.2 with the AC/DC module was used. The geometries of copper and indium modeled

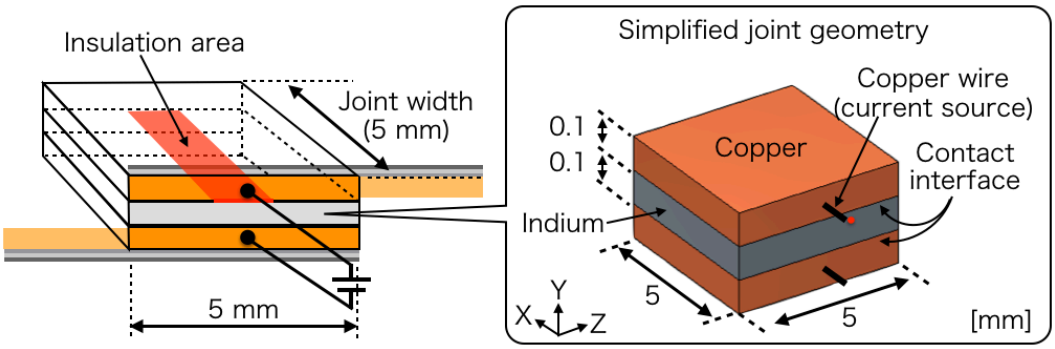

Fig. 3.16: 3-dimensional simulation model for simplified lap joint section

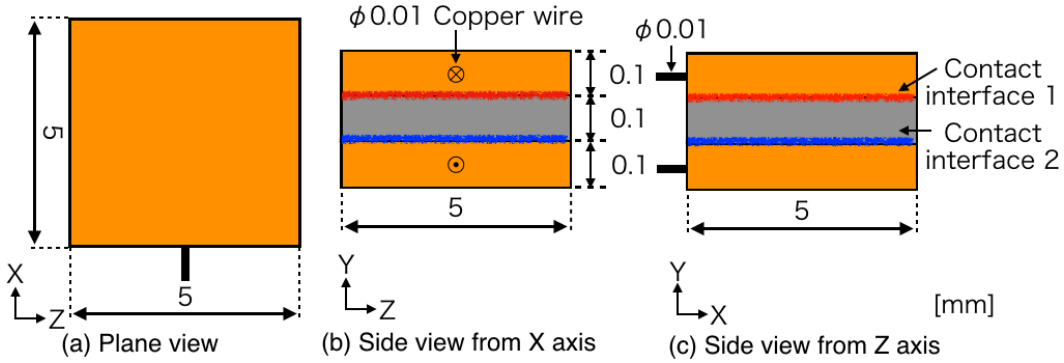

Fig. 3.17: Geometry of the simplified joint model

the joint from lot Fuji and the thickness of layers was 100 µm. The interface between the copper layer and indium foil simulated a contact resistivity of 3.25 pΩm^2 from an extrapolation using an empirical value of 0.5 pΩm^2 contact resistivity at cryogenic temperature [46][67]. A certain area with insulation condition was configured to simulate the air gap existing at the upper contact interface. A current of 0.1 A was applied to copper wire, and the voltage of two copper wires was acquired. To evaluate the feasibility of this idea, the variation of the voltages, $Variation(x)$, influenced by the contact condition, was calculated using Eq. 3.2.

$$\text{Variation}(x) = \frac{V_x - V_0}{V_0} \times 100 \tag{3.2}$$

Where$x$, V_x, and $V_0$are the parameter, voltage of the copper wire when the parameter is x, and voltage without any insulation (77.6 µV), respectively.

As first step, the width of the insulation condition area was fixed to 5 mm, and the length of the area swept from 0 to 4 mm with an interval of 0.5 mm. The condition of contact interfaces and the calculated variation are shown in Fig. 3.18. Air gap on the contact interface 1 was simulated, and the condition of interfaces is distinguished by different color. The contact condition equal to the contact resistivity of 3.25 pΩm^2 that aforementioned before. The result of the voltage as more than 4 % in Fig. 3.18 (c) shows the large difference cause by the air gap can detected, and indicates the thought-up current application is effective in detecting the full-width wide air gap. This model of the air gap is corresponding to the 2-dimensional model

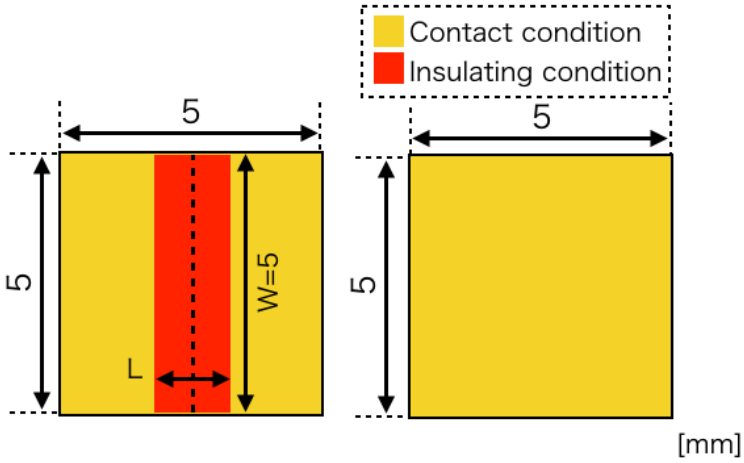

(a) Contact interface 1 (b) Contact interface 2

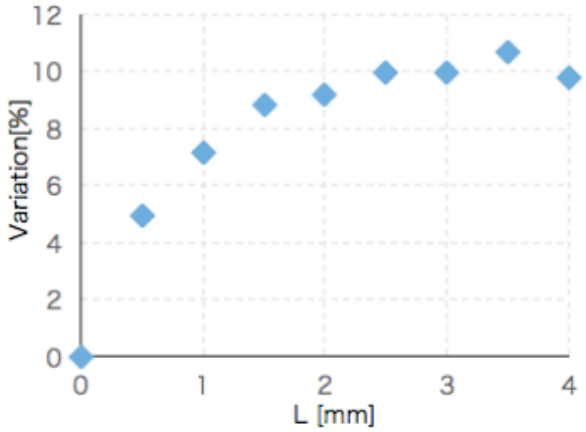

(c) Length dependency of detectable potential variation

Fig. 3.18: Application for detecting full-width wide air gap at joint area

with the air gap existed in the center of the joint shown in Fig. 3.14. In the 2-dimensional model simulation, the air gap is undetectable from Fig. 3.15 (b) due to the current path. Therefore, inducing current from side advanced the availability of prediction using electric characteristics evaluation.

As second step, the air gap existed inside the joint was simulated, and detectability of the same current inducing method was evaluated. As shown in Fig. 3.19 (a)(b), air gap on the contact interface 1 was simulated as same as the firs step. The length of the air gap is fixed to 0.5 mm, and the distance between the air gap and the side, W, was swept from 0 to 4 mm. Fig. 3.19 shows the geometry of the simulated air gap and the result of variation dependency on W. The variation indicates in case the air gap existed at the inner side of the joint and the distance from the side is more than 0.2 mm, it would be difficult to detect the distinct the existence of the air gap from the voltage. Since the air gap inside the joint is the most important defect need to be distinct, the reason for this result needs to be identified for advancing.

The current path at the cross-section of current inducing copper wires, as shown in Fig. 3.20 was focused on. The current distribution at according cross section with the condition that W = 0 mm and W = 0.1 mm are shown in Fig. 3.21. The streamline indicates the current path, and

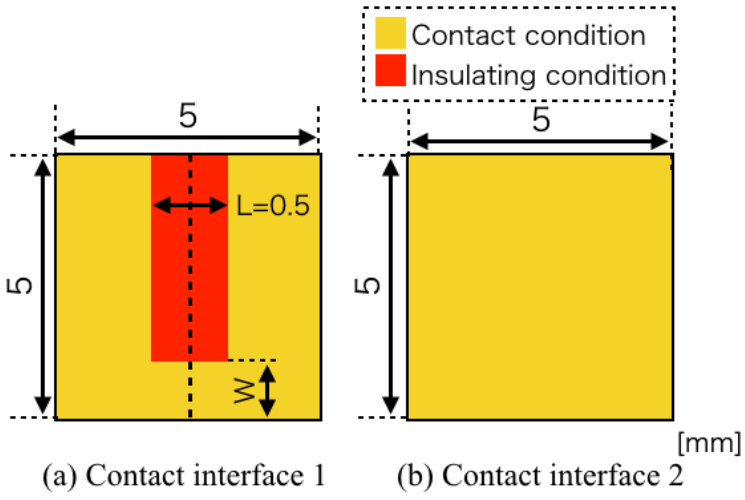

(a) Contact interface 1 (b) Contact interface 2

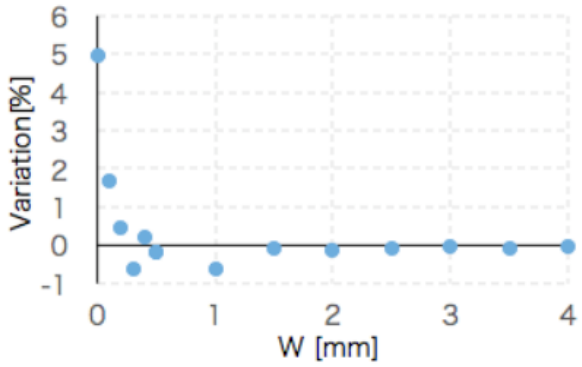

(c) Depth dependency of detectable potential variation

Fig. 3.19: Application for detecting air gap inside the joint area

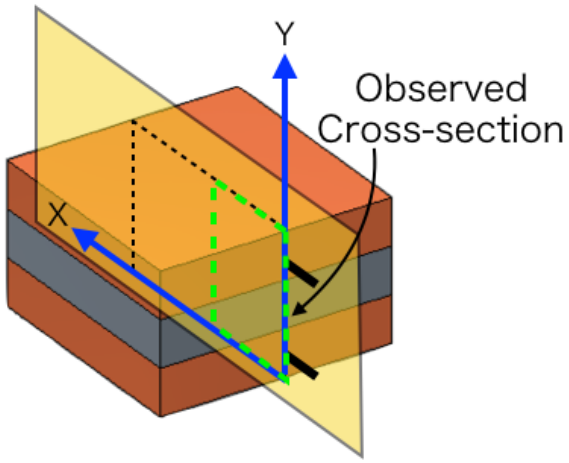

Fig. 3.20: Location of focused on cross section for current distribution analysis

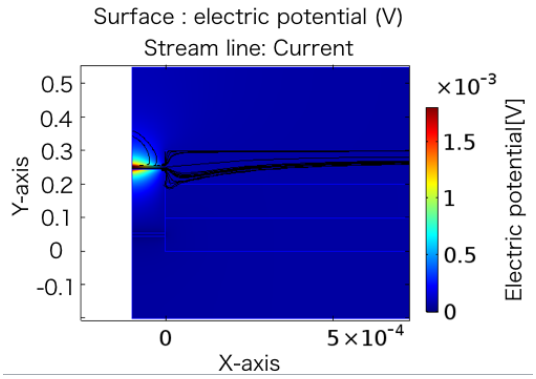

(a) Current distribution with W = 0 mm

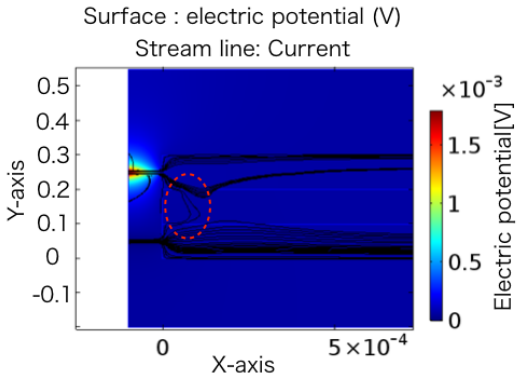

(b) Current distribution with W = 0.1 mm

Fig. 3.21: Current distribution at the cross section of current inducing copper wires

the current applied from the upper copper wire flows to the lower copper wire at once circled by the red dot line can be found in Fig 3.21 (b). Since these current would not be disturbed by the air gap, the variation of the voltage at the copper wires would not appear enlarged and detectable. Even if only a short area at the side contact normally, the induced current would flow concentrated on this area and result in difficulty in finding the influence of the air gap existing inside the joint. Further variation of air gap was not evaluated due to this difficulty of current flow characteristics.

3.4 Summary

In this section, the correlation between the joint resistance at cryogenic temperature and the electric impedance at room temperature was measured and evaluated for discussing the applicability of electric characteristics measurement for contact resistance evaluation. Two kinds of typical REBCO tape, the REBCO tape with soldered stabilizer layers from Fujikura Ltd. and that with electroplated stabilizer layer from Super Power Inc. was used to discuss. A number of single-layer joint samples were prepared, and the joint resistance at cryogenic temperature and electric impedance at room temperature were measured and compared. Although the electric impedance was expected to have frequency dependency, no tendency could be confirmed. The correlation between the two temperature also examined no correlation could be observed. This result indicates the even the joint resistance cryogenic temperature is high, no characteristics of the electric impedance at room temperature can be used to predict this.

The reason for this correlation is analyzed using numerical simulation modeling the joint. The difference in the current path between the cryogenic temperature and the room temperature is illustrated in Fig. 3.4 (a). The direction of the current passing the joint was found to be different, and this difference results from the contrast of the electrical properties of the material and results in difficulty of distinguishing the joint resistance at cryogenic temperature from measurement at room temperature.

Remediation by inducting current from the side was considered and simulated. This method is sufficient to distinguish the existence of a full-joint-width wide air gap, which was difficult in the conventional measurement at room temperature. However, the air gap that existed inside the joint is difficult to be detected since the induced current would flow concentrated on the area that normally contacted, as illustrated in Fig. 3.4(b).

From the aforementioned experimented and simulated result, the application using electric characteristics measurement for evaluating the contact condition is concluded to be inadequate.

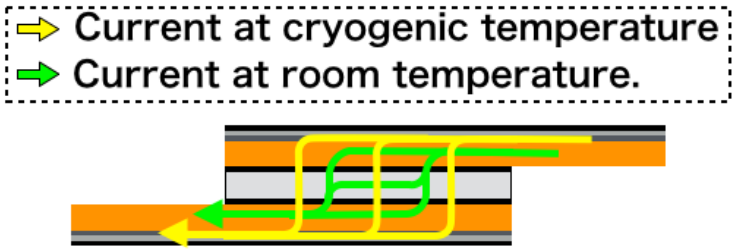

(a) Current paths at cryogenic and room temperature

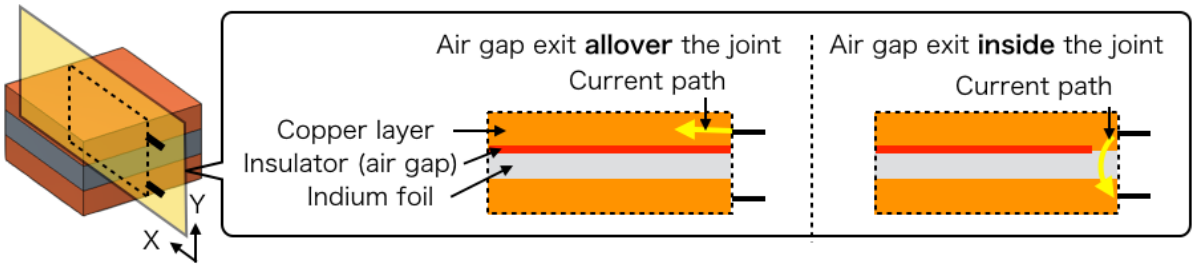

(b) Current paths at remediated current application method

Table. 3.3: Schematic current path at joint

4 Application of X-ray Computer Tomography scan

4.1 Objective

The X-ray CT scan is considered as the other technique for evaluating contact resistance in the joint. The contact area that can be observed using X-ray CT scanner was focused and analyzed in following procedure.

1. Evaluating the influence of extruded indium caused by the pressurizing of joining using numerical simulation.

2. Scan the joint sample with X-ray CT scanner, and measuring the joint resistance at 77 K, then scanning the sample again for comparing the contact condition before and after the cooling.

3. Introducing an image segmentation technique to evaluate the contact area quantitatively.

4. Evaluating the influence of cooling by comparing the observed contact area before and after the cooling.

5. Evaluate and analyzing the contact resistivity at the contact interfaces using the observed contact area.

The single-layer lap joint samples with 4-mm-wide REBCO tapes from Super Power Inc. were prepared. Since the indium at the joint extruded by pressurization of the joint, the influence of these indium was evaluated using numerical simulation. This is to define the contact area that needs to be focused. Then the prepared samples were scanned using X-ray CT scanner, and the joint resistance of each sample were measured at 77 K. The cross-sectional images of contact interfaces from each joint sample were extracted manually, and the air gap existing at the contact interface could be observed visually. An image segmentation technique called graph-cut was introduced to evaluate the contact area quantitatively. The observed contact area before and after the sample cooled down to 77 K was compared to the influence of cooling on contact area. The contact resistivity was calculated using the observed contact area, and the nominal contact area that calculated by simply multiplying the original joint length and REBCO tape width was used to compare with that using the observed contact area to discuss the achievement using an X-ray CT scan. The variation of contact area was considered from the perspective of contact theory.

4.2 Fabrication of single-layer lap joint sample

The fabrication of the joint sample and the compositions of the REBCO tapes were illustrated in Fig. 4.1. The REBCO tape is 4-mm-wide copper-stabilized REBCO tapes (SCS4050-AP, SuperPower Inc, Schenectady, NY, USA, I_c : over 91 A at 77 K and self-field). The tapes from two different lots were used and denoted as lot A and lot B. The compositions and the thicknesses of the tapes: layers from the top to the bottom are copper (20 µm), silver (1.6 µm), REBCO (1.6 µm), buffer layers (less than 0.2 µm), Hastelloy substrate (50 µm), silver (1.6 µm), and copper (20 µm). The copper surface at the top of the REBCO tapes at the joint section was ground using sandpaper with an abrasive particle diameter of 81 µm. Then the surface was cleaned with ethanol. And a 100-µm-thick indium foil was also cleaned using ethanol for the preparation of joining.

After the grinding and cleaning, the top surfaces of the two REBCO tapes were set face-to-face, and the indium foil was inserted between them. A pressure of 100 MPa was applied by bolting a set of stainless steel jig [66]. The required torque was calculated using Eq. 2.36, and was applied by two steps: fist the half of the torque and then full torque, to apply the pressure as uniform as possible. The pressure was applied at room temperature for 1 minute, and the thickness of the joint was measured using a micrometer(MDC-25SB, Mitsutoyo corp., Kanagawa, Japan) after releasing the pressure. This is because the indium plastically deformed by the pressure, and the degree of the formation could not be control precisely due to the pressuring condition. The resulting indium thickness is also needed for discussing the contact condition later. The resulting indium lasted in the joint is the properties of indium at the pressurizing condition e.g. temperature, pressuring time. Although the improvement for joining technique is under developing[46][47], the condition of joint fabrication related to this research was unified for the discussion under the objective. 41 samples were prepared, 23 samples using REBCO tape from lot A, of which 15 samples had a 5-mm-long joint length, four samples had a 2-mm-long joint length, and four samples had a 10-mm-long joint length. For the 18 samples using the REBCO tapes from lot B, all their joint lengths were 5 mm. Fig. 4.2 shows the process of fabricating a single lap joint sample with a 10-mm-long joint length, and the number

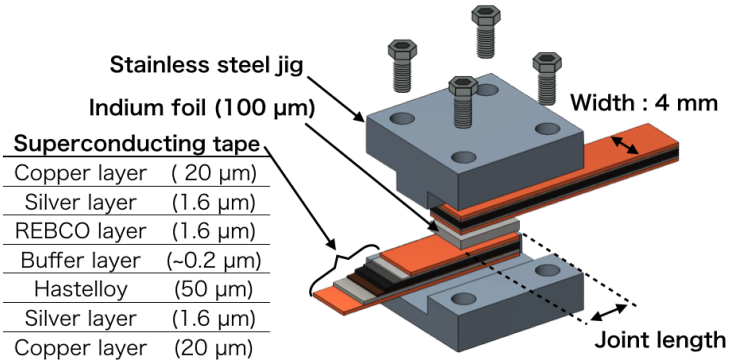

Fig. 4.1: Fabrication of single lap joint sample with 4-mm-wide REBCO tape

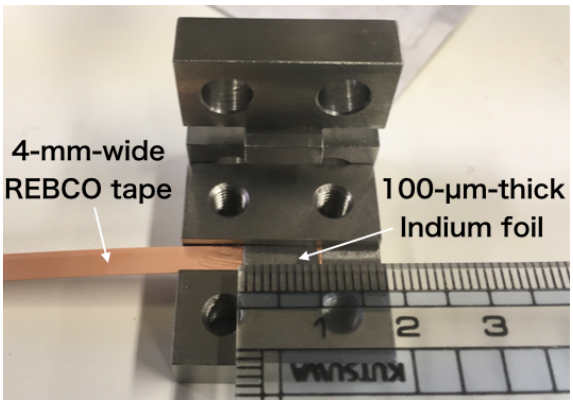

(a) Indium foil on a REBCO tape

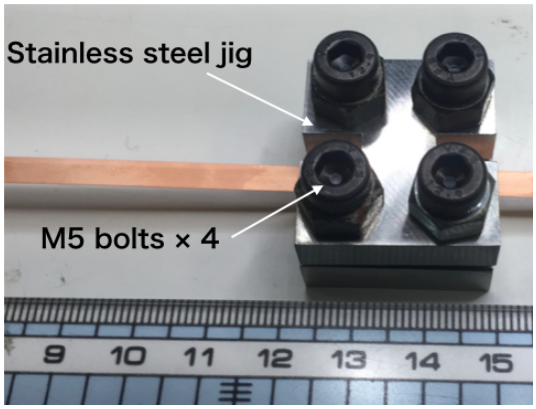

(b)Applying pressure at joint

Fig. 4.2: Fabrication of the single-layer lap joint sample with 4-mm-wide REBCO tape

Table. 4.1: Number of joint sample

lot name	joint length (mm)	number of sample	name of sample
A	5	15	A1-15
A	2	4	A16-19
A	10	4	A20-23
B	5	18	B1-18

of prepared samples and the allocated name were listed in Table 4.1

4.3 Influence of extruded indium foil

After the pressurizing of the joint, the indium extruded from the joint as shown in Fig. 4.3 because the indium plastic deformed easily. The contact area of contact interfaces is considered to have a direct influence on the joint resistance. The indium foil extruded from the joint section by the pressurizing is also possibly influence the joint resistance by adding current path and lowering the joint resistance. Therefore, the influence of this extruded indium was analyzed using a numerical simulation. The extruded indium in joint length direction and width direction are evaluated, respectively. The simulation was based on the method described in Section 3.3, and the geometry is modified accordingly for the analysis.

Fig. 4.4 shows the evaluation for extruded indium in joint length direction. Fig. 4.4 (a) shows the case that the indium extruded to the right, and the extruded length was swept from 0 to 1 mm. The cases that the indium extruded to the left, the right and the both were simulated. The current distribution in the case that indium extruded to the right for 1-mm length was displayed in Fig. 4.4 (b). Although the current flowed the extruded indium, the current path shown by the streamline indicated no significant increment in extruded indium.

Fig 4.5 shows the evaluation for extruded indium in width direction. The extruded indium has also simulated the cases to the left, the right, and both from 0 to 1 mm. The current distribution in the case that indium extruded to the right for 1-mm length displayed in Fig. 4.4 (b) indicated only little the current flows the extruded indium.

The joint resistance is calculated by Eq. 3.1, and the change ratio of the joins resistance expressed in Eq. 4.1 are compared with extruded length and extruded width.

$$\text{Change ratio} = \frac{R_{(\text{L or W})} - R_0}{R_0} \tag{4.1}$$

Where the R_{L} and R_{W} are the joint resistance with extruded length and width respectively, and R_0 is the joint resistance without the extruded indium (extruded length = 0 mm and extruded width = 0 mm). Fig. 4.6 shows the result of comparison and indicates the change ratio of the joint resistance is 1.5 % in the maximum. The ratio can be considered low enough to be omitted.

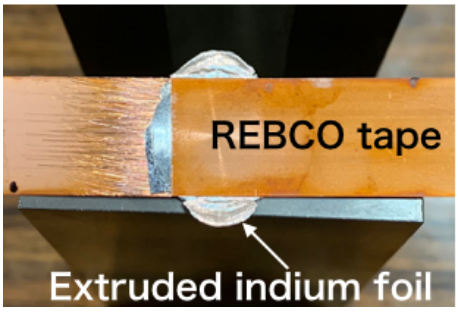

Fig. 4.3: Extruded indium of single-layer joint sample

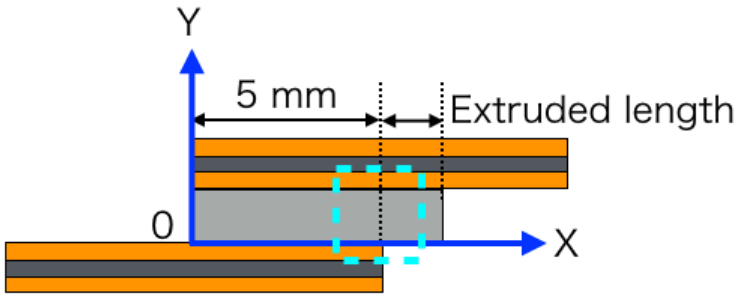

(a) Simulation model for extruded indium in joint length direction

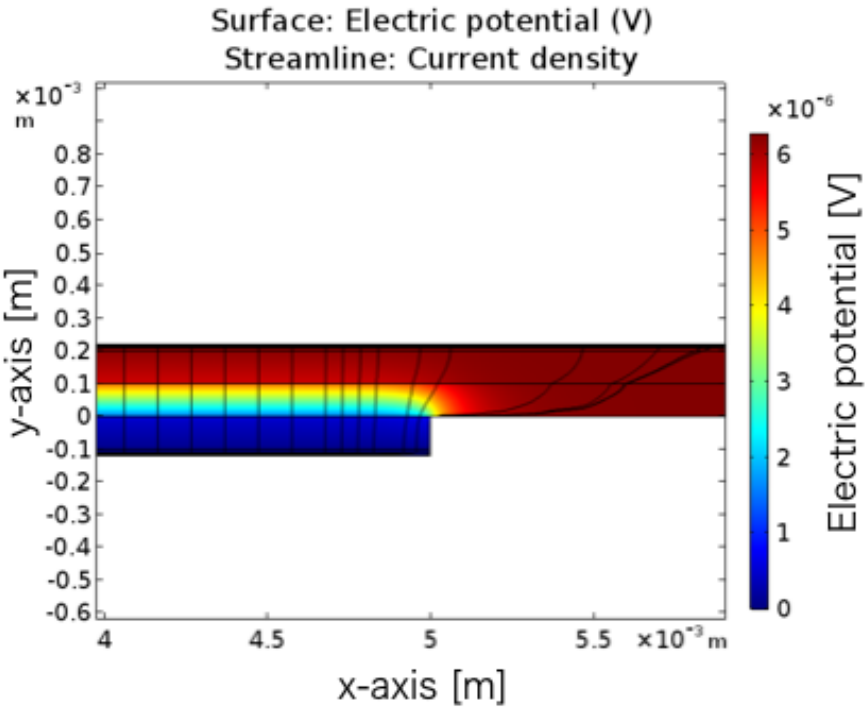

(b) Current distribution at the extruded indium

Fig. 4.4: Evaluation for extruded indium in joint length direction

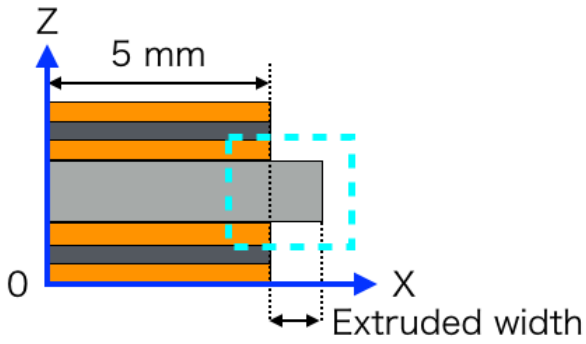

(a) Simulation model for extruded indium in width direction

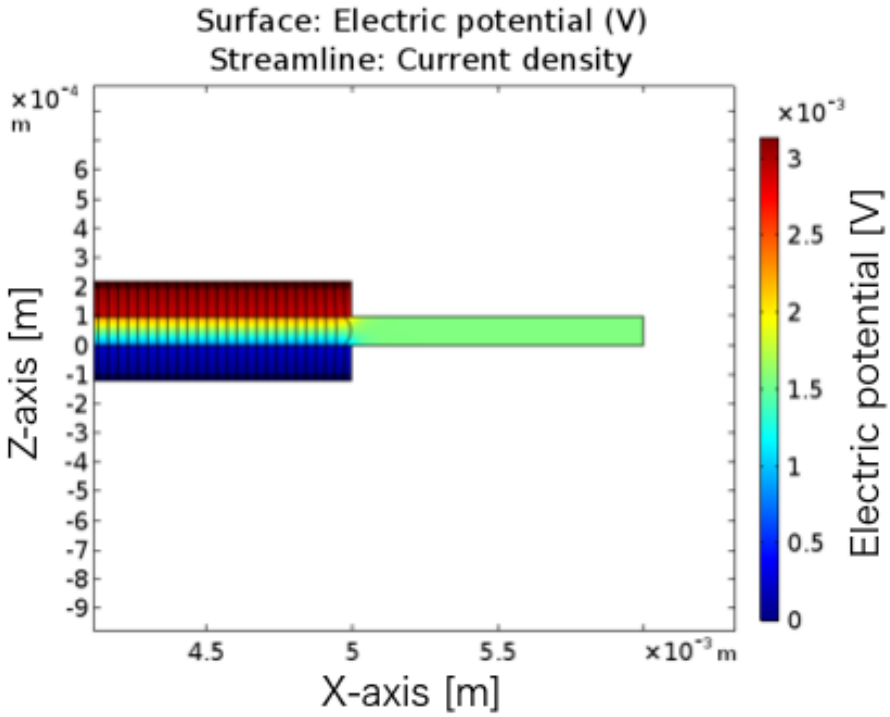

(b) Current distribution at the extruded indium

Fig. 4.5: Evaluation for extruded indium in width direction

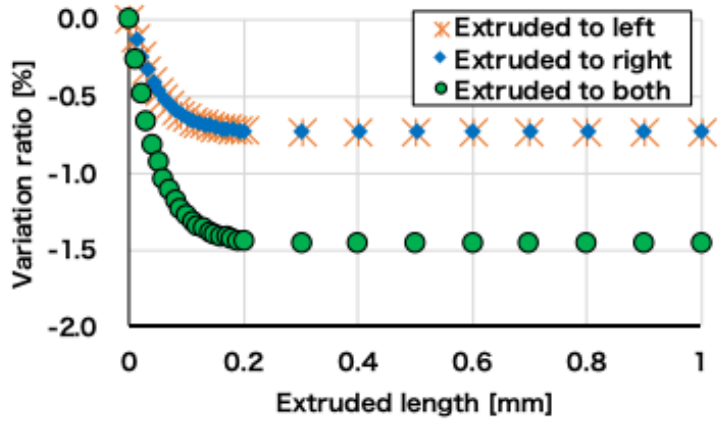

(a) Joint resistance variation by extruded indium length

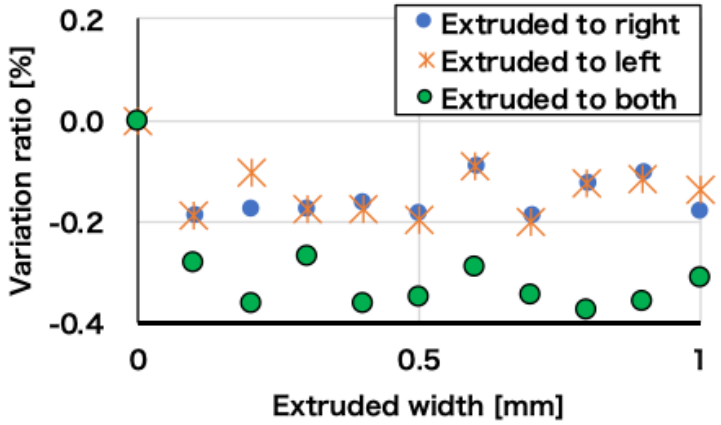

(b) Joint resistance variation by extruded indium width

Fig. 4.6: Joint resistance variation by extruded indium

4.4 Experimental conditions

Each single-layer lap joint sample was scanned using an X-ray CT scan and measured the joint resistance in liquid nitrogen to evaluate the correlation between the contact area and contact resistance. Each sample was scanned before and after the cooling to evaluate the cooling influence on the contact area.

Fig. 4.7 shows the sample set up for the X-ray CT scanner (ScanXmate-D160TS110, Comscantecno Company Ltd., Yokohama, Japan) to observe two contact interfaces between the REBCO tapes and the indium foil. The number of projections was 600, and the X-ray tube voltage and X-ray tube current were set to be 145 kV and 20 µA, respectively. A metallic filter was not used. The obtained three-dimensional CT data consists of $496 \times 496 \times 496$ voxels. The size of the voxel was 13.168 µm for the samples with 2 mm and 5 mm joint length, and 25.957 µm for 10 mm long joint samples, which were the smallest available sizes of the instrument depending on the size of the samples.

After acquiring the first X-ray CT scan, each sample was cooled using liquid nitrogen (77 K), and the joint resistance, R_{joint}, was measured from the current-voltage slope ($I - V$ curve) using the four-terminal method. Fig. 4.8 illustrated the experimental set up for the measurement. The two terminals that were used to measure voltage were set on both REBCO tapes that straddle the joint, with a separation distance of approximately 20 mm. Currents up to 40 A (0, 10, 20, 30, and 40 A) were applied, and the joint resistance was evaluated by applying the least-squares approach to the measured $I - V$ curve. Each sample was soaked into liquid nitrogen, measured twice, and heated to room temperature to confirm reproductivity of the $I - V$ curve. Subsequently, the samples were scanned by an X-ray CT scan again with the same conditions.

Fig. 4.7: Experimental set up for X-ray CT scan

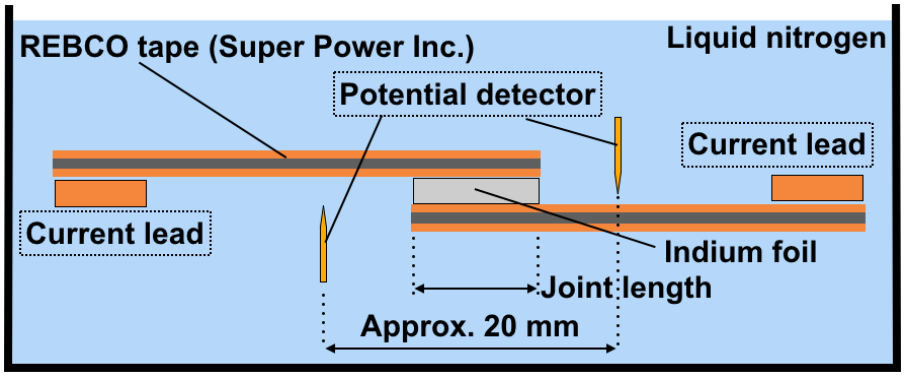

Fig. 4.8: Joint resistance measurement

4.5 Experimental result

4.5.1 Measurement of joint resistance

Several examples of joint resistance measurement results are shown in Fig. 4.9. The normal $I - V$ curve is the voltage proportionally increased according to the current increment. And the gradient of the curve is calculated using the least-squares approaches as joint resistance of each sample.

In the measurement, sample A7 and sample B8 shown different behavior, and the $I-V$ curve are shown in Fig. 4.10 For the result of sample A7 shown in Fig. 4.10(a), the gradient shows a significant increase after the current raised to more than 10 A, and the increase of voltage is extraordinarily high. This is considered to be the flux-flow resistance showed up and counted as a composition of electrical resistance. The I_c deterioration cause this phenomenon by the current exceed the I_c dramatically increase the voltage by translation of flux quantum. Therefore, the joint resistance of sample A7 was calculated used the voltages measured below the current of 10 A To eliminate the unnecessary increment in joint resistance, For the sample B8, the $I - V$ curve seems normal compared to that of sample A7. But in the measurement of the second time, the sample B8 quenched and burnout as Fig. 4.11. Therefore in the measurement of the sample B8, the current passed the stabilizer layer because the I_c deteriorated at the quenched spot possibly caused the resistance of the copper layer counted as a part of joint resistance. This assumption was validated using numerical simulation in section 4.9. Although these two samples were calculated and evaluated following, the value of these samples is considered to be unreliable for discussion. And noting that since the $I - V$ curve shows different tendency, the sample A7 was not inspected using the X-ray CT scan after the cooling.

The measured joint resistance, R_{joint} of each single-layer joint sample is listed in Table 4.2. And the contact resistance and contact resistivity are calculated sequentially using contact area.

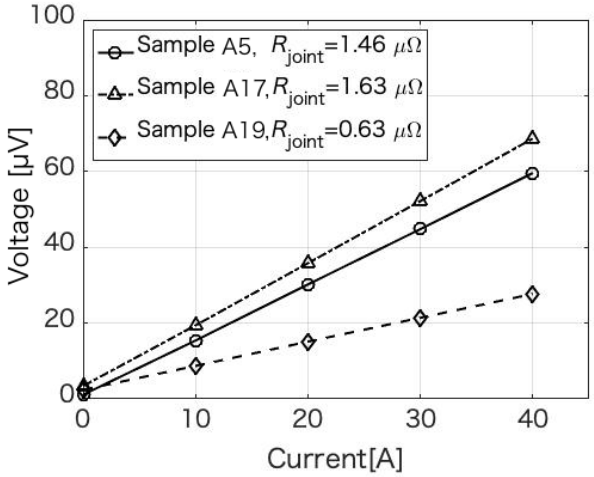

Fig. 4.9: Joint resistance measurement

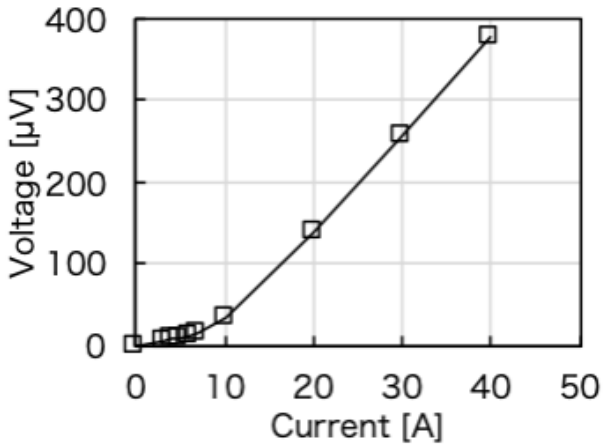

(a) Sample A7

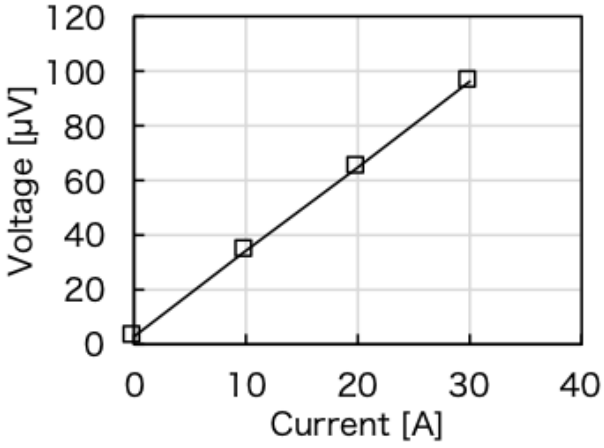

(a) Sample B8

Fig. 4.10: Joint resistance measurement of specific samples

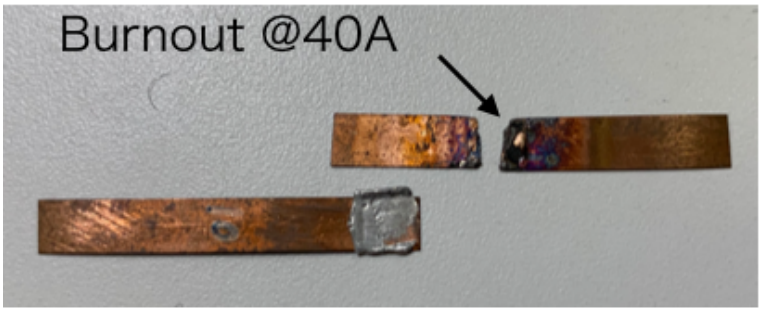

Fig. 4.11: Quenched and burnout sample B8

Table. 4.2: Joint resistance of narrow-width single layer lap joint sample

Sample name	Original joint length (mm)	Joint resistance (μΩ)	Sample name	Original joint length (mm)	Joint resistance (μΩ)
A 1	5	3.47	B 1	5	0.70
A 2	5	0.97	B 2	5	0.36
A 3	5	1.29	B 3	5	0.28
A 4	5	0.82	B 4	5	0.32
A 5	5	1.46	B 5	5	0.37
A 6	5	0.96	B 6	5	0.39
A 7	5	*2.06	B 7	5	0.59
A 8	5	0.75	B 8	5	*3.12
A 9	5	1.43	B 9	5	0.82
A 10	5	0.63	B 10	5	0.82
A 11	5	0.72	B 11	5	0.31
A 12	5	0.67	B 12	5	0.28
A 13	5	0.79	B 13	5	0.59
A 14	5	0.58	B 14	5	0.32
A 15	5	0.86	B 15	5	0.38
A 16	2	1.42	B 16	5	0.32
A 17	2	1.14	B 17	5	0.45
A 18	2	1.63	B 18	5	0.90
A 19	2	1.83			
A 20	10	0.63			
A 21	10	0.52			
A 22	10	0.50			
A 23	10	0.56			

4.5.2 Cross-sectional images extraction and observation

The cross-sections corresponding to the contact interfaces are shown in Fig. 4.12. Since the contact interface could not be kept strictly parallel to the axis of the scanned area, an arbitrary cross-section extraction was applied and used to extract the cross-sectional images of contact interfaces.

Each sample has two contact interfaces, and one of them from different joint length samples were are shown in Fig. 4.13. The image of the CT scan displays the distribution of CT numbers as explained in Eq. 2.33, which is a relative and average value of the X-ray attenuation coefficient in a voxel. The higher the atomic number is, the higher the CT number is, and the brighter the image is. The copper layer of REBCO tape, indium foil, and possibly air gap constitute the contact interface. Therefore, the brighter area is corresponding to the voxel has a high ratio of indium; in other words, the contacting area. In case the brightness of the image significantly lowered, that means the air gap is existing in the voxel or non-contact area.

However, although the composition of the same cross-section should be similar, the CT number is uneven in the direction of width. a cross-sectional image of a 5-mm long joint sample was chosen, and the CT number on a cut line of the cross-section was extracted in Fig. 4.14 to show the distribution of CT numbers. The distribution indicated the CT number at both sides is high, then gradually decreased in approaching the center of the joint.

This phenomenon is called the cupping effect, which is a kind of physical artifact of an X-ray CT scan. When the X-ray penetrating an object, the intensity of the X-ray would be weakened following the attenuation coefficient, as expressed in Eq. 2.13. The attenuation coefficient varied depend on the energy of a X-ray photon, and the attenuation coefficient energy dependency of copper and indium [60] are shown in Fig. 4.15. The tendency of energy dependency indicates the lower the X-ray energy is, the more the attenuate happened. When the X-ray with a range of energy (white X-ray) penetrating an object, the outer of the object attenuates the low energy X-ray first, result in that the attenuation seems to be higher at the outer of the object in appearance. The X-ray used for common X-ray equipment is white X-ray because the equipment generating single-energy X-ray (monochromatic X-ray) required a limited environment like a particle accelerator. Therefore the cupping effect is inevitable at the current stage.

The cross-sectional images of the joint provide the information of the contact interface, and the size of the actual contact area can be considered to be helpful for the evaluation of contact condition. Based on the physical characteristics of the white X-ray described above, the cross-sectional images that both sides of the joint tend to be brighter than the center can be explained. However, since the CT number that corresponding to the existence of an air gap is not unique, the area that contact and non-contact could not be discriminated by a certain threshold of CT number. Common image segmentation techniques like edge detection were not appropriate to use in the segmentation and calculation of the contact area.

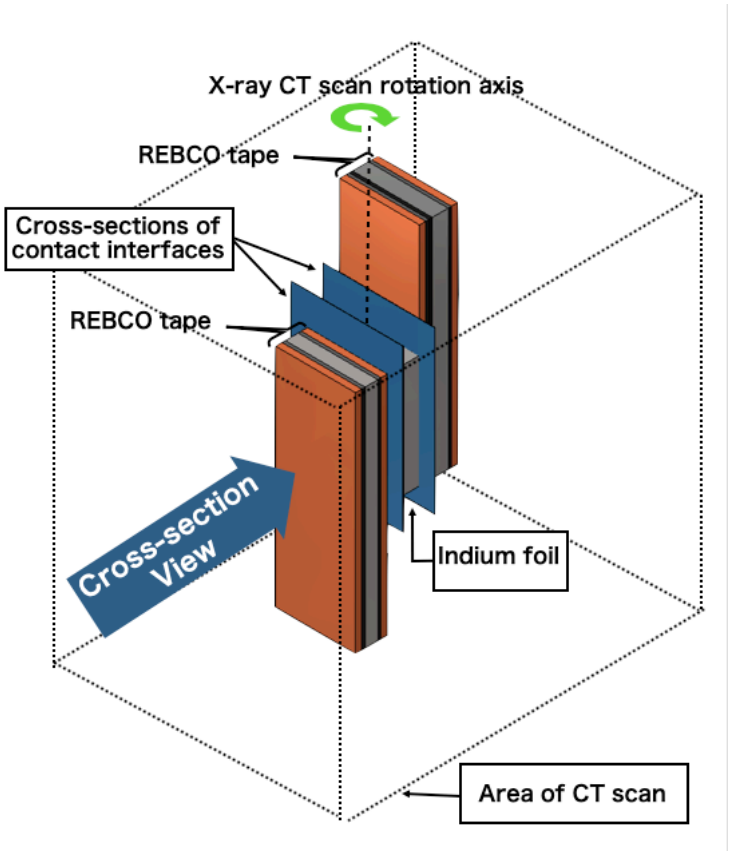

Fig. 4.12: Location of cross-sectional images of contact interface

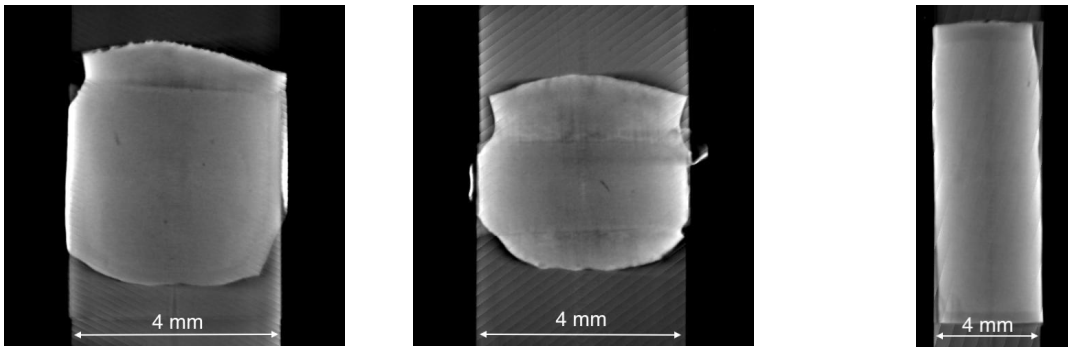

(a) Joint sample with 5-mm long joint length

(b) Joint sample with 2-mm long joint length

[c] Joint sample with 10-mm long joint length

Fig. 4.13: Extracted cross-sectional image of contact interface

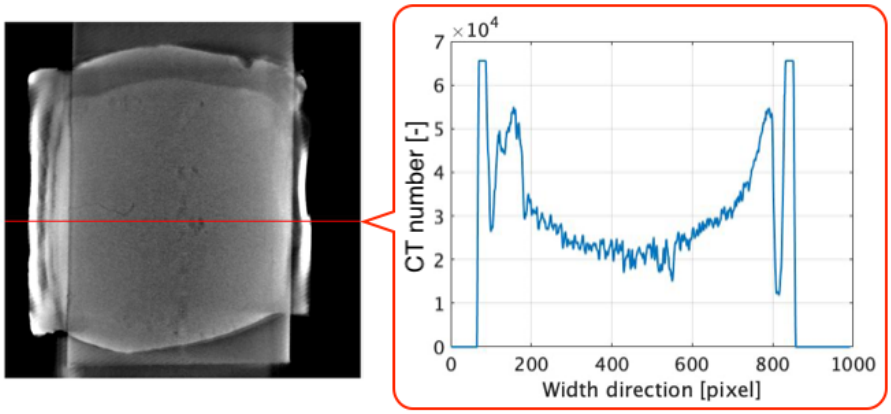

Fig. 4.14: Distribution of CT number at cross-sectional image

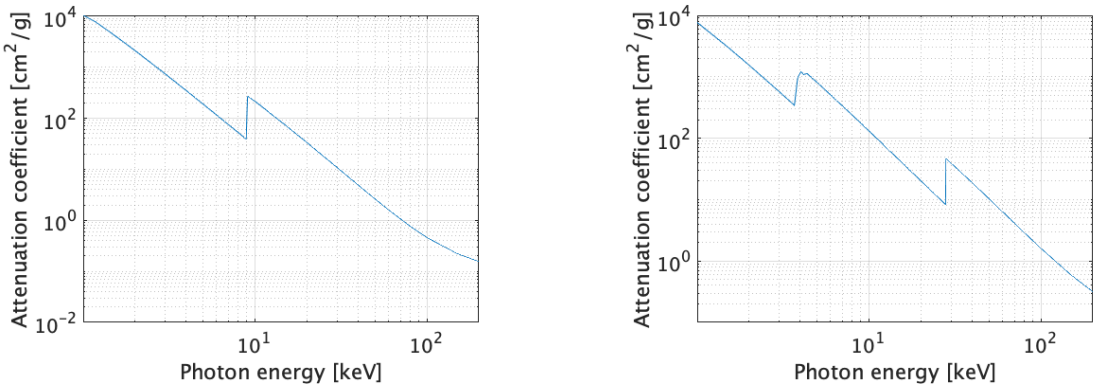

(a) Copper (b) Indium

Fig. 4.15: X-ray attenuation coefficient

4.6 Evaluation for contact area of contact interfaces

After acquired the images of the contact interface, the contact area is needed to be evaluated from the images. Using a threshold for distinguishing the contact area and the area with an air gap (non-contact area) is inappropriate due to the cupping effect. The feature that the non-contact area can be identified visually was focused. An image segmentation technique based on the similarity called graph-cut image segmentation [69] was introduced to segment the contact area.

The concept of the technique is minimum cut, as shown in Fig. 4.16. The pixels can be considered as the grid, and the CT number is corresponding to the value at each point. The connection between each point is calculated as cost, and the connection with reference is also calculated as cost. In case the CT number is similar in adjacent pixels, the cost between these pixels is high. After the cost distribution, cutting was applied. If the cutting was applied to a line ,the cost of the line was accumulated. The cutting method for the smallest sum of cost can be interpreted as the easiest way to separate the dissimilar group. Therefore, this image segmentation can separate the the pixels according to their similarity and belonging group.

Based on the evaluation of extruded indium in the section 4.3, the cross-section illustrated in Fig. 4.17 was mainly focused. The area of two REBCO tapes superposing was identified as the region of interest (ROI) based on X-ray transmission images of the joint, then the cross-sectional images corresponding to the contact interface in Fig. 4.17(b) were extracted.

The series of image segmentation is displayed in Fig. 4.18 as an example. Fig. 4.18 (a) represents the X-ray transmission image of a sample B3, and its ROI was the ranged following the contour of the tapes, as shown in Fig. 4.18 (b). Fig. 4.18 (c) shows one of the two cross-sectional images of the two contact interfaces from the sample, which were extracted from the X-ray CT data. It should be noted that the shape of the two REBCO tapes in Fig. 4.18 (c) consists of the top surface of the REBCO tape and a partial volume averaging, which is a kind of artifact of X-ray CT. The reference data for two groups, the air gap existed area (non-contact area) and contact area, reference seeds for each group were selected manually based on the

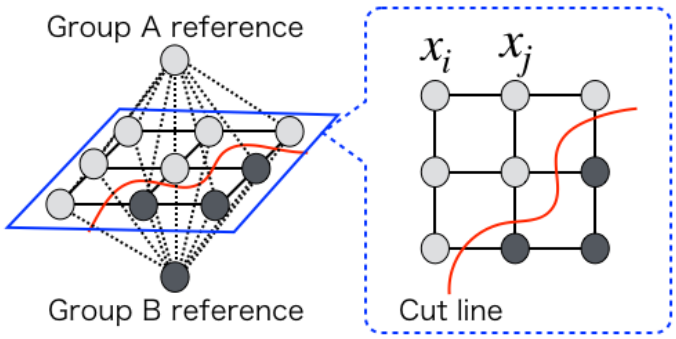

Fig. 4.16: Concept of graph cut segmentation

feature of X-ray CT scan [70]. In Fig. 4.18 (c), the dark areas around the center of the joint were identified as gap areas. The seeds of the gap were chosen at these spots (arrowhead No. 1). In addition, a discontinuous and dark area in the upper and lower area in the ROI could be observed (arrowheads No. 2). These are dark bands, which is another kind of artifact of X-ray CT, caused by the boundary between different X-ray attenuation properties. The seeds of the gap area were also selected in these dark bands areas. The seeds of the observed contact area were selected in the area except for the gap areas as arrowhead No. 1 and No. 2. The calculation of the graph cut was executed, and Fig. 4.18 (d) shows the segmented observed contact area acquired from the cross-sectional image.

An integrated image segmentation program was developed using MATLAB R2018a with the Image Processing Toolbox. Fig. 4.19 shows the graphic user interface of the program. The area framed by a blue dot line in the left is to cut out an arbitrary cross-section and the extract the cross-sectional images at contact interfaces, whereas the area framed by an orange dot line in the right is utilized for image segmentation.

After the acquisition of the three-dimensional data taken by X-ray CT scan, the area of two REBCO tapes superposing was identified as the region of interest (ROI) based on X-ray transmission images of the joint. This is because the content in section 4.3 indicated that the indium outside the superposing area has little effect on the joint resistance. Then we manually extracted two-dimensional cross-sectional images corresponding to the contact interfaces shown in Fig. 4.17 (b). The tilted angles in width and longitudinal direction was calculated to correct the contact area. In order to reduce the computational resource necessary for subsequent image segmentation, Simple Linear Iterative Clustering [68]was applied to the extracted images. The number of superpixels was 5120. Subsequently, graph cut was utilized to segment the ROI into areas with and without air gap because only the presence of air contributes to an abrupt change in the CT number. Points with a locally small CT number were chosen as initial seeds for areas with gaps; those with a relatively large CT number were chosen as the areas of the observed contact area. Finally, the calculation was executed, and the two observed contact areas of the two contact interfaces are denoted as S_{CT1} and S_{CT2} for distinction. The contrast of the image was appropriately adjusted using histogram equalization to enhance the visibility of the ROI and the seeds of the air gap areas. The segmentation processing was performed three times to evaluated the error caused by the different initial seed points. The ratio that observed contact area accounts for the nominal contact area (product of joint length and width of REBCO tape) is shown in Fig. 4.20, and the actual contact area that observed by X-ray CT scanner generally less than that of nominal contact area.

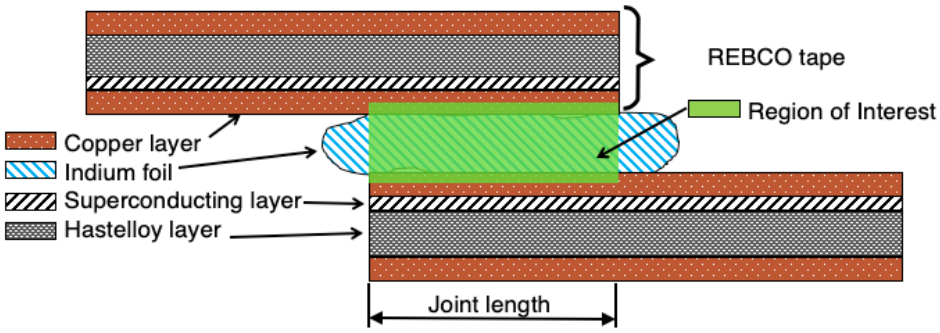

(a) Region space of ROI

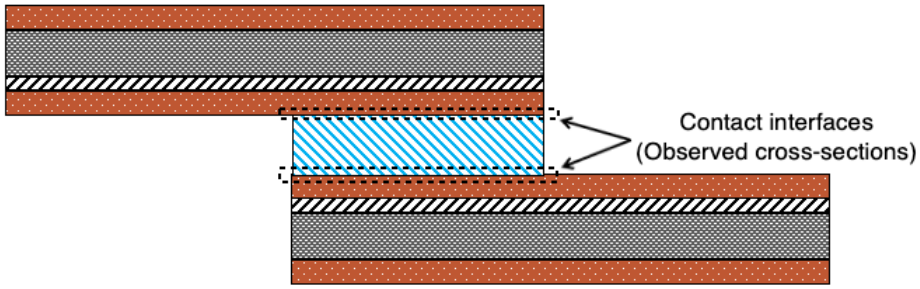

(b) Position of observed cross-sections at joint

Fig. 4.17: Configuration of extracted cross-sectional images

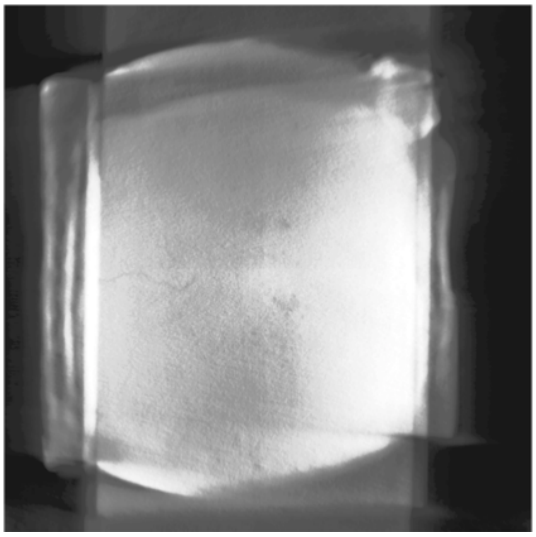

(a) X-ray transmission image

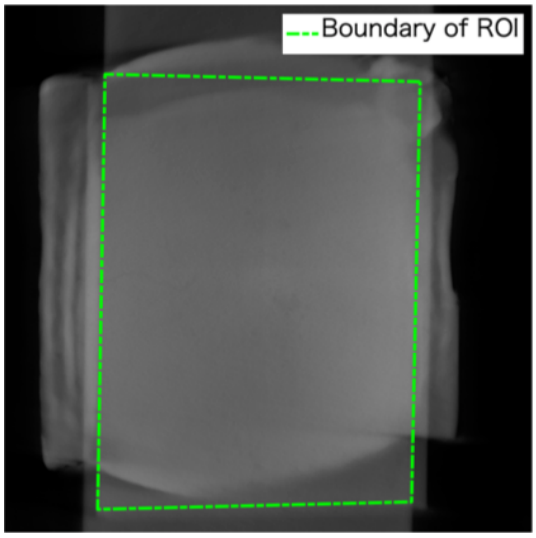

(b) Ranging region of interest (ROI)

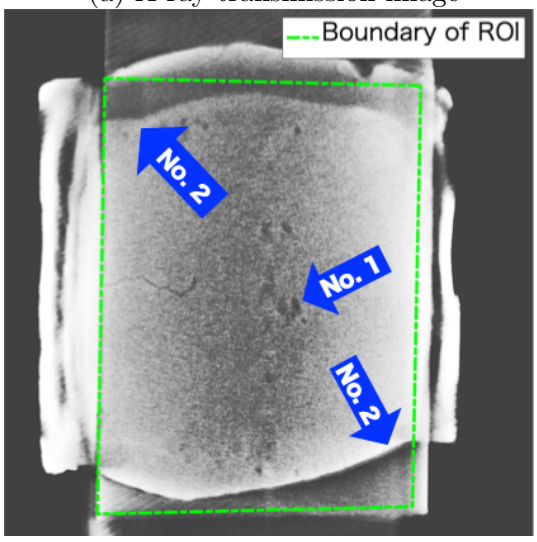

[c] Locating the seeds of non-contact area

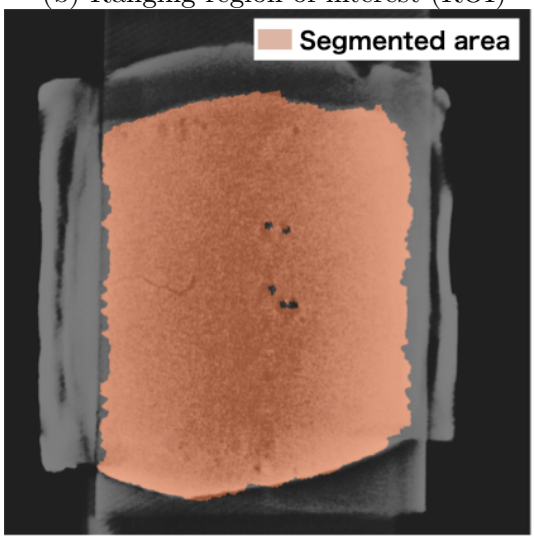

[d] Segmented contact area

Fig. 4.18: Procedure of contact area segmentation

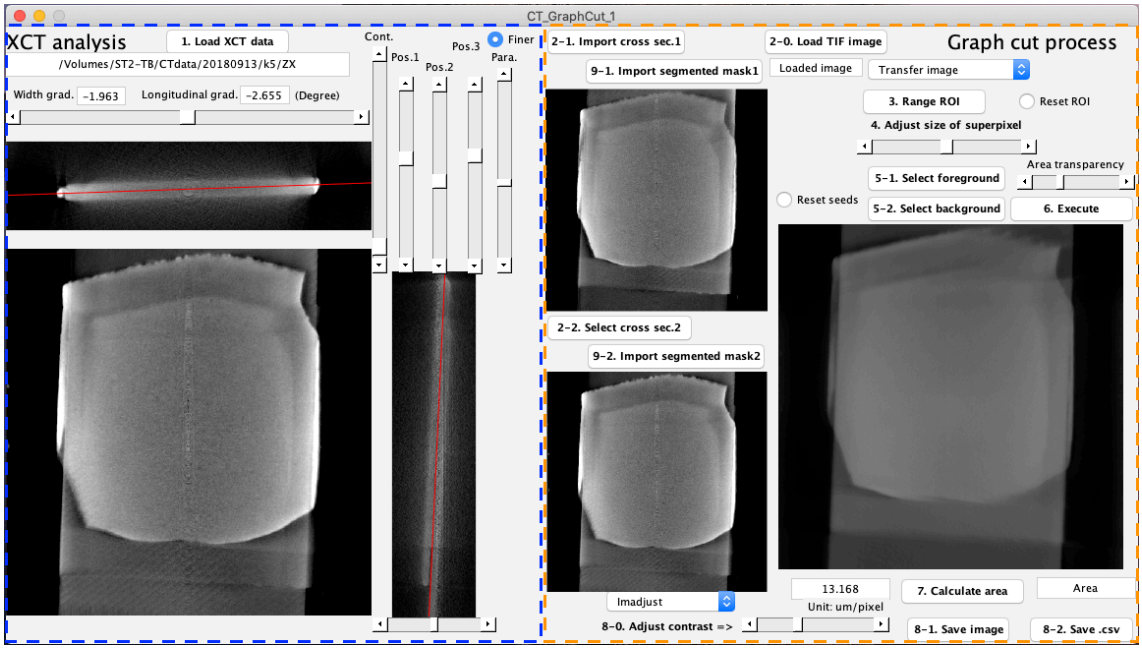

Fig. 4.19: Graphical User Interface for contact area calculation

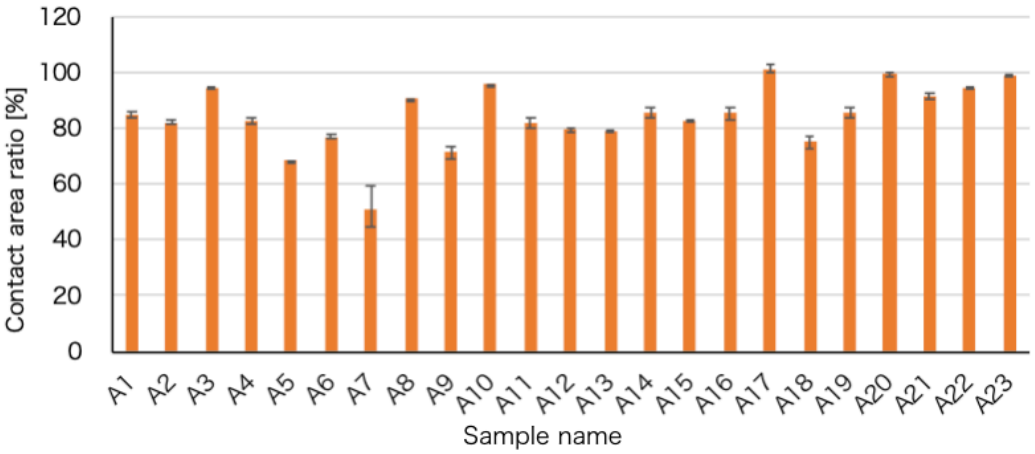

(a) Lot A

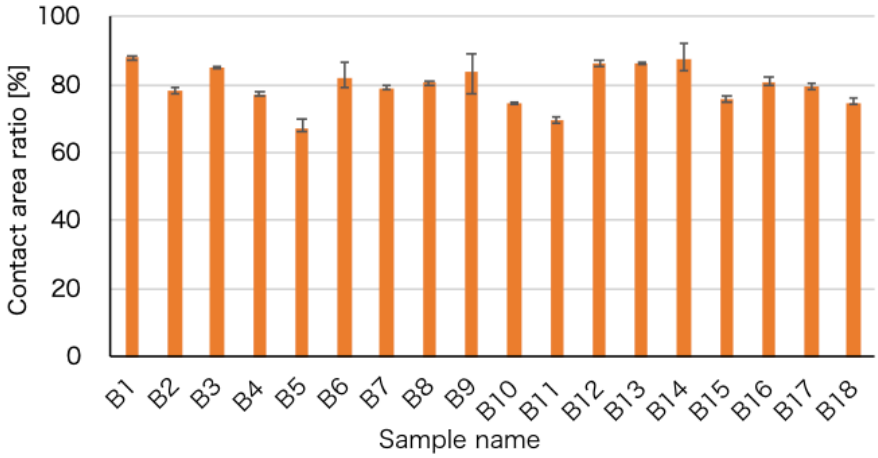

(b) Lot B

Fig. 4.20: Segmented contact area ratio

4.7 Comparison of contact area before and after cooling

The two observed contact area S_{CT1} and S_{CT2} is able to be calculated with introducing the graph cut segmentation technique described in section 4.6. The sum of the segmented contact area $S_{CT1} + S_{CT2}$ before and after the cooling from each joint sample was compared in Fig. 4.21. Although the slight difference is exist, no typical tendency could be found in the evaluation. Besides, the difference is smaller than the error caused by how the seeds for foreground and background were chosen. Therefore, the influence of cooling is concluded to be not significant.

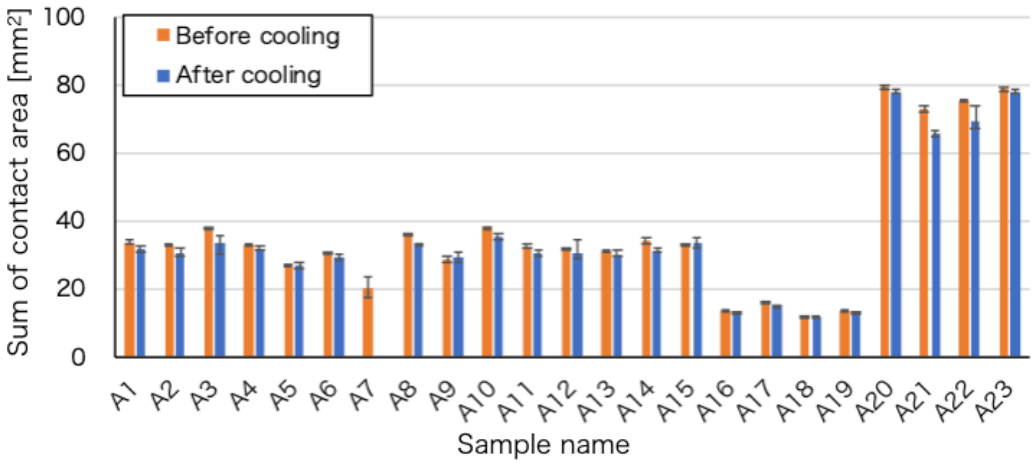

(a) Lot A

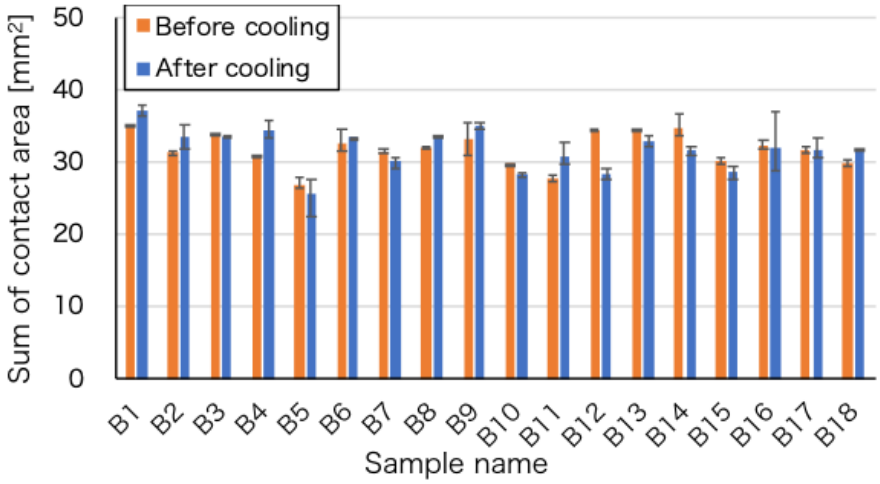

(b) Lot B

Fig. 4.21: Sum of contact area before and after cooling

4.8 Evaluation of contact resistivity

4.8.1 Calculation of contact resistivity

In a conventional evaluation, the “nominal contact area S_{n}”, which is calculated by simply multiplying the joint length and width of the REBCO tape is used to calculate contact resistance. Using the S_{n}, the contact resistance R_{n} can be expressed as Eq. 4.2

$$R_{\mathrm{n}} = R_{\mathrm{joint}} - (2 \times \rho_{\mathrm{Ag}} \frac{T_{\mathrm{Ag}}}{S_{\mathrm{n}}} + 2 \times \rho_{\mathrm{inter}} \frac{1}{S_{\mathrm{n}}} + 2 \times \rho_{\mathrm{Cu}} \frac{T_{\mathrm{Cu}}}{S_{\mathrm{n}}} + \rho_{\mathrm{In}} \frac{T_{\mathrm{In}}}{S_{\mathrm{n}}}) \tag{4.2}$$

where$\rho_{\mathrm{Ag}}, \rho_{\mathrm{Cu}}, \rho_{\mathrm{In}}$, are the resistivity of silver, copper, and indium at 77 K ($\rho_{\mathrm{Ag}} = 2.70 \times 10^{-9}\Omega\mathrm{m}, \rho_{\mathrm{Cu}} = 2.10 \times 10^{-9}\Omega\mathrm{m}, \rho_{\mathrm{In}} = 1.67 \times 10^{-8}\Omega\mathrm{m}$) [29], $T_{\mathrm{Ag}}, T_{\mathrm{Cu}}, and T_{\mathrm{In}}$ are the thicknesses of silver, copper, and resulting indium. T_{In} was in 32 µm to 94.5 µm range. ρ_{In} (= 1.05 p $\Omega\mathrm{m}^2$) is the interface resistivity evaluated from a previous study.

By use of X-ray CT scan, the “observed contact area S_{CT}” are able to be utilized to calculate the contact resistance R_{CT}. The calculation using two contact area of two contact interfaces, S_{CT1} and S_{CT2} can be expressed as Eq. 4.3

$$\begin{aligned} R_{\mathrm{CT}} = R_{\mathrm{joint}} - (\rho_{\mathrm{Ag}} \frac{T_{\mathrm{Ag}}}{S_{\mathrm{CT1}}} + \rho_{\mathrm{inter}} \frac{1}{S_{\mathrm{CT1}}} + \rho_{\mathrm{Cu}} \frac{T_{\mathrm{Cu}}}{S_{\mathrm{CT1}}} + \rho_{\mathrm{In}} \frac{T_{\mathrm{In}}}{\sqrt{S_{\mathrm{CT1}}}\sqrt{S_{\mathrm{CT2}}}} \\ + \rho_{\mathrm{Cu}} \frac{T_{\mathrm{Cu}}}{S_{\mathrm{CT2}}} + \rho_{\mathrm{inter}} \frac{1}{S_{\mathrm{CT2}}} + \rho_{\mathrm{Ag}} \frac{T_{\mathrm{Ag}}}{S_{\mathrm{CT2}}}) \end{aligned} \tag{4.3}$$

The calculated contact resistance R_{n} and R_{CT} was listed in Table 4.3.

Table. 4.3: Contacct resistance of narrow-width single layer lap joint sample

Sample name	R_n (μΩ)	R_{CT} (μΩ)	Sample name	R_n (μΩ)	R_{CT} (μΩ)
A 1	3.29	3.24	B 1	0.52	0.50
A 2	0.80	0.75	B 2	0.17	0.14
A 3	1.11	1.07	B 3	0.10	0.07
A 4	0.66	0.62	B 4	0.14	0.12
A 5	0.29	0.21	B 5	0.20	0.11
A 6	0.79	0.72	B 6	0.16	0.12
A 7	1.88	*1.69	B 7	0.41	0.35
A 8	0.58	0.54	B 8	2.93	*2.89
A 9	1.26	1.19	B 9	0.64	0.62
A 10	0.47	0.45	B 10	0.65	0.57
A 11	0.54	0.49	B 11	0.14	0.09
A 12	0.51	0.46	B 12	0.11	0.04
A 13	0.62	0.56	B 13	0.41	0.37
A 14	0.42	0.38	B 14	0.15	0.10
A 15	0.68	0.65	B 15	0.20	0.13
A 16	1.04	0.95	B 16	0.14	0.10
A 17	0.74	0.71	B 17	0.27	0.22
A 18	1.29	1.17	B 18	0.72	0.68
A 19	1.47	1.40			
A 20	0.54	0.54			
A 21	0.43	0.41			
A 22	0.42	0.40			
A 23	0.48	0.48			

4.9 Analysis of contact resistivity

The comparisons between the contact area and contact resistance are shown in Fig. 4.22. The comparison of two lots shows no specific tendency in the contact resistance indicated no significant different in performance between two lot. The plot that circled by red dot line is corresponding to the sample A7 and B8, which was confirmed to have I_c deteriorated area in the REBCO tape. Since the joint resistance of these samples were relatively high, one reason for high contact resistance is considered to be the $I_c$deterioration, which is not the contact resistance exactly. Since the REBCO tapes superposing at the joint were inaccessible using the four-terminal method, we could not identify the quality of the REBCO tapes. The situation illustrated in Fig. 4.23 possibly occurred and increase the value of contact resistivity.

The result of sample A7 and B8 shown in Fig. 4.10 and Fig. 4.11 validated the possibility of I_c deterioration in REBCO tape. The sample A1 with extraordinary high contact resistance compared to other joint samples was also considered to have the I_c deterioration. To identify the existence of I_c deterioration, the current up to 100 A was applied to sample A1. Fig. 4.24 shows the measured $I-V$ curve of the sample A1. Since the I_c of the REBCO tape used in sample A1 was 91 A, the feature of I_c deterioration could not be confirmed. The sample S1 was concluded to have extremely poor contact condition with current result.

However, the possibility that the I_c deterioration existed at the joint section could not be taken away. A numerical simulation was conducted to confirm the possibility of this assumption. The model simulated the I_c deteriorated area that existed in the joint section is shown in Fig. 4.25. The numerical simulation is based on the description in Section 3.3, and the particular area inside the REBCO layer is modified to the insulator to simulate the I_c deteriorated area. The distance between the edge of the deteriorated area and the joint section was 1.0 mm, and the distance between the other edge of the deteriorated area and the joint section was denoted as the depth of deteriorated area (D_{det}) and varied from 0.6 to 1.0 mm. Referring to Eq,

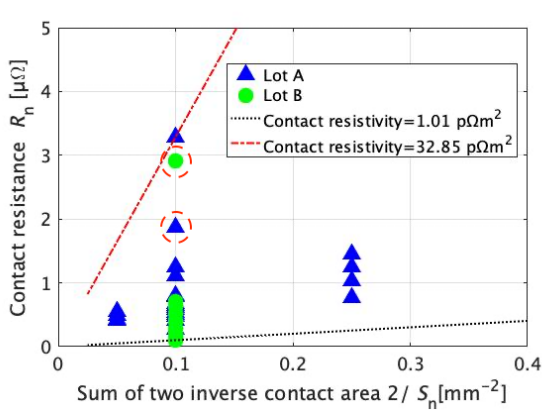

(a) Correlation between $2/S_n$ and R_n

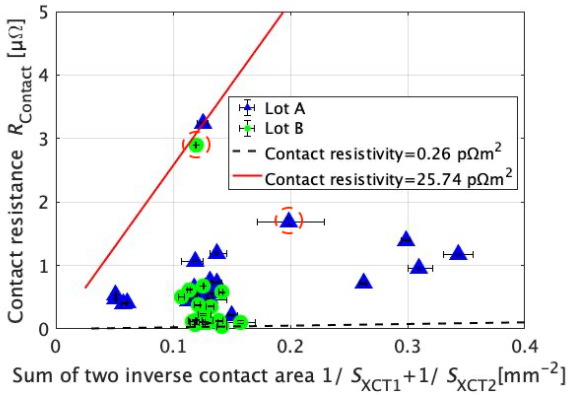

(b) Correlation between $1/S_{CT1}+1/S_{CT2}$ and R_{CT}

Fig. 4.22: Comparison between contact are and contact resistance

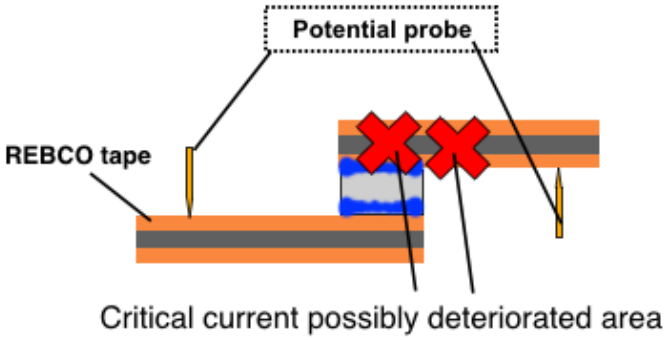

Fig. 4.23: Assumed deteriorated area at REBCO tape

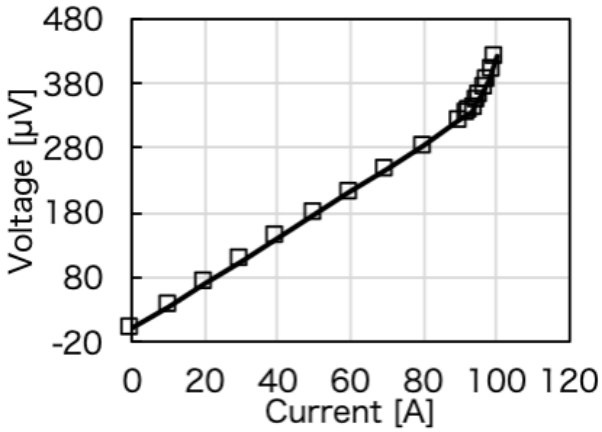

Fig. 4.24: $I-V$ curve of sample A1

3.1, the contact resistance is calculated by surface integration of the generated energy density at imaginary conductance. The contact resistance varied by the depth of the deteriorated area is shown in Fig. 4.25(b). When the depth of the deteriorated area was 0.66 mm, and the length of the deteriorated area is 0.34 mm, the contact resistance increased to 3.00 μΩ, which is approximately equal to those of the two joint samples with extraordinary high contact resistance. Since the 0.34 mm of I_c deteriorated area is possible to exist, the probability that the I_c deterioration inside the joint section increases the evaluated contact resistance is validated.

In case the I_c deteriorated area outside the joint section, as similar to the case of sample B8, the simulation model illustrated in Fig. 4.26(a) was simulated and evaluated. The length of deteriorated area (D_{det}) was swept from 10 to 100 μm, and the calculated contact resistance varied by the D_{det} indicates only ten μm length of the deteriorated area is long enough to increase the contact resistance high.

Based on the aforementioned simulated validation, the joint sample with extraordinary high contact resistance is reasonable to consider I_c deteriorated area between the potential probes as a cause. Since I_c deterioration is not the feature of the contact condition, the samples of A7 and B8 were excluded in further discussion.

The relationship between the contact resistances R_n and the sum of two inverse nominal contact areas $2/S_n$ is shown in Fig. 4.22 (a). the contact resistivity was calculated by multiplying

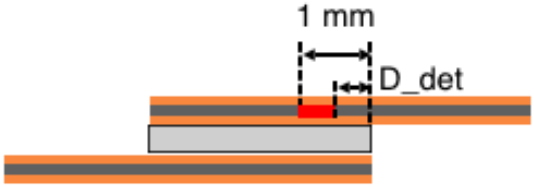

(a) Model of I_c deteriorated area inside the joint section

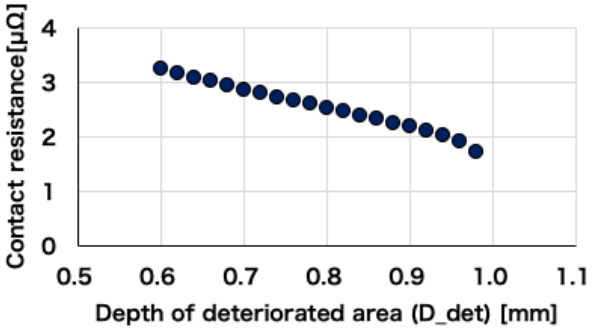

(b) Contact resistance variation by depth of deteriorated area (D_{det})

Fig. 4.25: Simulation for I_c deteriorated area inside the joint section

(a) Model of I_c deteriorated area outside the joint section

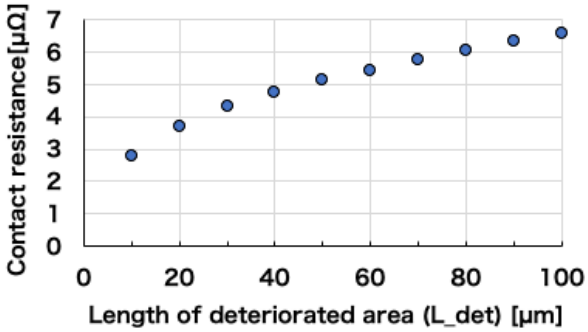

(b) Contact resistance variation by length of deteriorated area (L_{det})

Fig. 4.26: Simulation for I_c deteriorated area outside the joint section

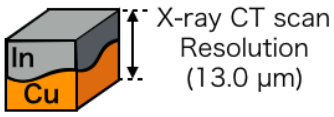

Fig. 4.27: A voxel of X-ray CT scan image

the contact resistance and the nominal contact area. The lines correspond to contact resistivity of 1.01 and 32.85 pΩm^2, which is minimum and maximum contact resistivity calculated using R_{n}. This parameter is calculated by multiplying the contact resistance Rn and the sum of the two nominal contact areas $2R_{\mathrm{n}}$ to determine the average contact condition of the two contact interfaces. The results indicate that except for the two samples which had relatively high contact resistance, the sample with larger contact areas tended to have relatively high contact resistivity. The existence of air gaps is considered to increase the contact resistivity because of the difficulty of uniformizing joint pressure for larger joints. It was necessary to eliminate the gap area to verify this assumption.

In Fig. 4.22 (b), the relationship between R_{CT} and the sum of the inverse observed contact areas $S_{\mathrm{CT1}} + S_{\mathrm{CT2}}$ was shown. The contact resistivity, ρ_{contact} calculated by using contact resistance R_{CT} and the sum of the two observed contact area $S_{\mathrm{CT1}} + S_{\mathrm{CT2}}$ with Eq. 4.4

$$\rho_{\mathrm{contact}} = R_{\mathrm{CT}} \times \frac{1}{\frac{1}{S_{\mathrm{CT1}}} + \frac{1}{S_{\mathrm{CT2}}}} \tag{4.4}$$

The lines correspond to contact resistivity of 0.26 and 25.74 pΩm^2 that were minimum and maximum contact resistivity Compare to the result shown in Fig. 4.22 (a), it was determined that the dependency of contact resistance on the contact area tended to be more linear. By eliminating the air gap area using an X-ray CT scan for inspection, the evaluation of the contact resistivity can be achieved more accurately.

Considering the dispersion of the contact resistivity in Fig. 4.22 (b), although the local I_{c} degradation on REBCO tapes is one possibility, the contact condition changes with the scale smaller than X-ray CT scan resolution would be the primary cause. Fig. 4.27 illustrated the composition of a voxel of X-ray CT scan image. One pixel in the image have a thickness with resolution of X-ray CT scan strictly, and the observed contact area is not the exactly boundary of the contact interface but the space include the contact interface. The volume of voxel is consist of copper and indium, and show the averaged property of component material. In case the air existed inside the voxel, the average density would decreased and then visually discriminable. Therefore the size of detectable air gap is governed by the resolution of X-ray CT scan.

In the boundary of two different metals, micro-gap, oxidized film, and alloy are present. Theoretically, a study showed [71]the real contact area accounts for nominal contact area less than 50% from the microscopic-scale point of view. The effect of micro-gap and the thin oxidized film is too small to affect CT numbers, and the alloy of the two metals is too similar to be

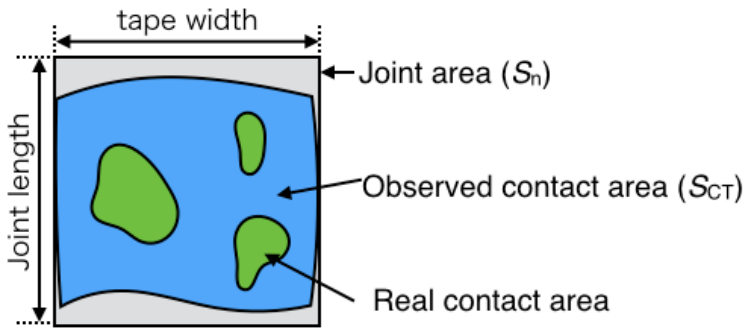

Fig. 4.28: Image of contact area

segmented from the other voxels consisting of the same metals. As such, it is difficult to identify the distribution of these micro-order fine structures to evaluate the real contact area. In the case that the real contact area distributed uniformly on the S_{CT1} and S_{CT2}, the contact resistance R_{CT} could be expected to proportionate to the sum of inverse contact area $1/S_{CT1} + 1/S_{CT2}$. Consequently, the result with dispersive contact resistivity can be interpreted as the inhomogeneous distribution of real contact area that could be evaluated using another method having much finer spatial resolutions than the X-ray CT scan adopted in this study. For the case to improve the ability of an X-ray CT scan to achieve the much finer spatial resolution, finer X-ray detects sensor and smaller focus of X-ray tube can be considered. For the latter, however, to achieve high X-ray penetrating power though the high atomic number and dense material like indium, high energy of the electron is needed to collide to the target material, and the heat generated by the electron collided to the target would be concentrated on the focus area and melt the target material. The current focus size of the X-ray tube is micro-meter order with tungsten target, and minify the size of focus is difficult. An innovative X-ray generation method is needed to achieve the finer spatial resolution for observing micro-meter order or even finer object.

According to the theory of electric contacts [72] and the improvement of the joining method [48] [49] [46] [46] [50]developed based on the theory, the distribution of real contact area varies with the joining process. Based on the result above, we conclude that the range of the contact resistance prediction is improved with the acquisition of the observed contact area, but cannot be perfectly predicted only from the scale of this region.

Considering the ratio of the real contact area governs the contact resistance theoretically, and the real contact area accounts for a certain ratio to the observed contact area, as illustrated in Fig. 4.28, the contact resistivity can be taken as a benchmark value for the ratio of the real contact area. Since the real contact area varied depend on the joining condition, the contact resistivity corresponding to certain joining methods. Evaluating and contact resistivity using X-ray CT can acquire an accurate range of contact resistivity corresponding to the joining method. Therefore, using an X-ray CT scan for evaluating contact resistance is conclude to be adequate and suitable to proceed to further analysis.

4.10 Summary

In this section, the applicability of an X-ray CT scan for evaluating contact condition was discussed. 41 samples of single-layer lap joint fabricated with 4-mm width REBCO tapes were prepared, and the contact interfaces were observed using an X-ray CT scan. The extruded indium caused by pressuring of joining shown little influence on the evaluation of joint resistance. Therefore the area of extruded indium was omitted. The cross-sectional images corresponding to the contact interfaces were extracted. The contact area and the area that contain the air gap could be confirmed visually, and the graph cut image segmentation technique was used to segment the contact area quantitatively. The segmented contact area shows the nominal contact area, which is simply calculated by multiplying the width of REBCO tape and original joint length, is tend to be greater than the actual contact area observed using X-ray CT scan. The comparison of the contact area before and after the cooling showed the cooling does not affect the contact area. Using the observed contact area can achieve more accurate contact resistivity than using the nominal contact area, However, the local degradation of REBCO tape and micro-order fine structure in the observed contact area is considered to account for dispersive contact resistivity. Considering the achievement and the difficulties comprehensively, using an X-ray CT scan to inspect the contact interfaces is adequate at the current state. Further discussion about the joining and evaluation can be advanced using an X-ray CT scan.

5 Analysis on contact condition of joint sample using X-ray CT scan

5.1 Objective

Since The X-ray CT scan is considered as the appropriate evaluation technique, The contact resistance variation depends on the joint fabrication method is evaluated using X-ray CT scan to give a conclusion of preferable joining method. The latest joining technique: heat treatment was introduced to keep pace with the development of joining. The implement of this evaluation is listed following.

1. Fabricating and testing the single-layer lap joint sample and two-row-four-layer joint sample with simple-stack procedure and joint-piece procedure.

2. Evaluating and comparing contact resistivity of each sample and analyzing the reason for high contact resistivity.

3. Extrapolating the joint resistance from obtained result to evaluate the feasibility of the obtained result

REBCO tapes with 12-mm-wide, which is considered as the prime candidate for the fusion magnet, were used to fabricate joint samples for discussion. Three kinds of fabrication methods: single-layer lap joint, two-row-four-layer joint samples with two different fabrication procedures, were prepared and compared. The single-layer joint sample is used as a standard in comparison with of two-row-four-layer. The joint resistance, joint thickness, contact area of each joint were evaluated to calculate the contact resistivity. To evaluate the influence of the fabrication method on contact resistivity and concluded the optimal joint fabrication method, the contact resistivity from each joint sample was compared. The acquired contact resistivity is used to extrapolate the joint resistance at the operating condition to evaluate the feasibility of the acquired contact resistance.

5.2 Joint sample fabrication

5.2.1 Single-layer lap joint sample

Fig. 5.1 illustrated the fabrication process. The REBCO is 12-mm-wide copper-stabilized REBCO tapes (SCS12050-AP, SuperPower Inc, Schenectady, NY, USA, I_c : over 460 A at 77 K and self-field). The compositions of the tape are as same as those of 4-mm-wide REBCO tapes from Super Power Inc.. Random sections of the REBCO tape were tested to measure interlayer resistance (resistance of interfaces of REBCO/silver silver/copper) using contact-probing current transfer length method [74] in advance. The interlayer resistance, ρ_{inter}, was 4.2 pΩm^2. The copper surface at the top of the REBCO tape at the joint section was grounded using sandpaper with an abrasive particle diameter of 81 µm. Then the surface was chemically deoxidized using a commercial flux (SUSSOL-F, Hakko corp., Osaka, Japan) contains ZnCl (35-45%) and NH_3Cl(<10%). Finally, the surface was cleaned with ethanol. The indium foil was also cleaned using ethanol.

In the process of applying pressure, the number of bolts was increased to six due to the increment of contact joint area. The joint length was 10 mm, and the required torque was calculated from the Eq. 2.36. The torque was also applied with two steps. After reached the required torque, the sample was heated using an electric hot plate(). The temperature was raised to 120°C [50] and kept for 15 minutes. Then the required torque was applied again because the applied pressure decreases as a result of stress relaxation induced by heating treatment. Subsequently, the sample was put back on the hot plate and another 15 minutes of heating was applied. Finally, the required torque was applied again, and the sample was cooled down to room temperature. 8 samples were prepared and denoted as SingleLap1-8. Fig. 5.2 shows the REBCO tapes with indium foil in-between before applying pressure and heating treatment of the sample.

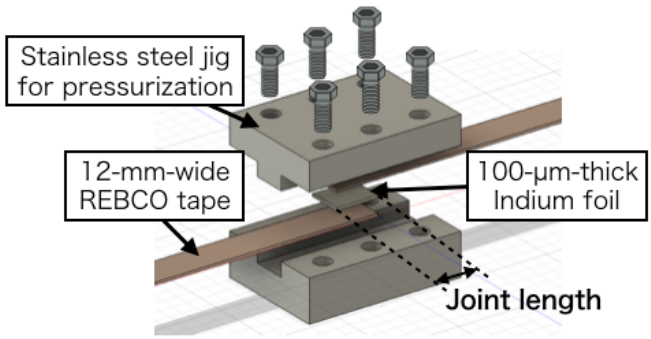

Fig. 5.1: Fabrication of single lap joint sample with 12-mm-wide REBCO tape

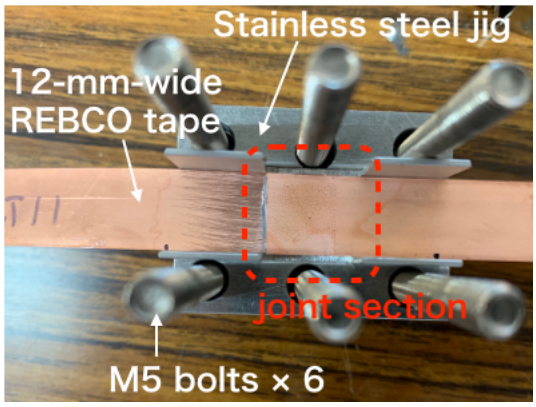

(a) Placing indium foil and REBCO tapes

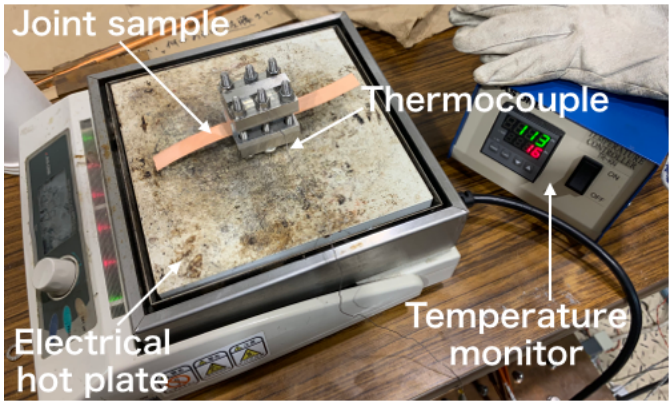

(b)Heating joint sample

Fig. 5.2: Fabrication of the single lap joint sample with 12-mm-wide REBCO tape

5.2.2 Two-row-four-layer joint sample

The schematic image of a two-row-four-layer joint sample is shown in Fig. 5.3. The joint has totally eight layers of the bridge-type joint, in which each layer has two single lap joints. For discriminating each joint, the rows were identified as north and south, and layers were numbered from one to four according to its layer from the top to the bottom. The two joints were named joint 1 and joint 2, which are distributed from overview of the samples. The geometry of the sample and the allocated name of each joint are shown in Fig. 5.4. The total length of the sample was 270 mm, and the length of each single lap joint was 10 mm. The original length of the indium foil was 9 mm to prevent overlapping and stress concentration during pressurizing. The terminal region for each layer was set 20-mm-long, and additional length of 15 mm was kept for the sample supporter. The joint section of four-layer REBCO tapes were sandwiched by two 2-mm-thick copper plates from the top and the bottom. The gap between two rows was 1 mm. The REBCO tapes used for the two-row-four-layer joint sample were as same as those of single lap joint samples with 12-mm-wide REBCO tapes.

The two-row-four-layer joint sample were fabricated with simple-stack procedure and joint-piece sample. Two procedure are illustrated in Fig. 5.5 and procedure of fabrication are explained in detail on the following. Two samples for each fabrication procedure were prepared and evaluated. The samples fabricated with simple-stack procedure were denoted as SimpleStack-1

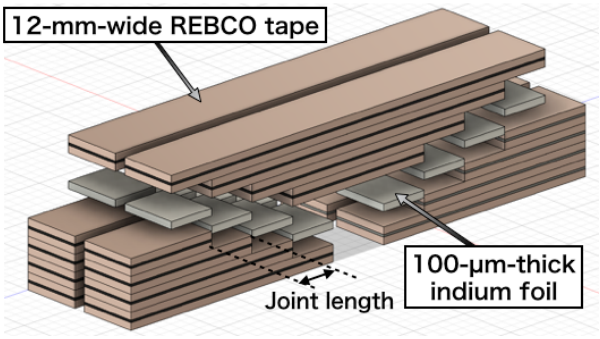

Fig. 5.3: Three-dimension view of two-row-four-layer joint sample

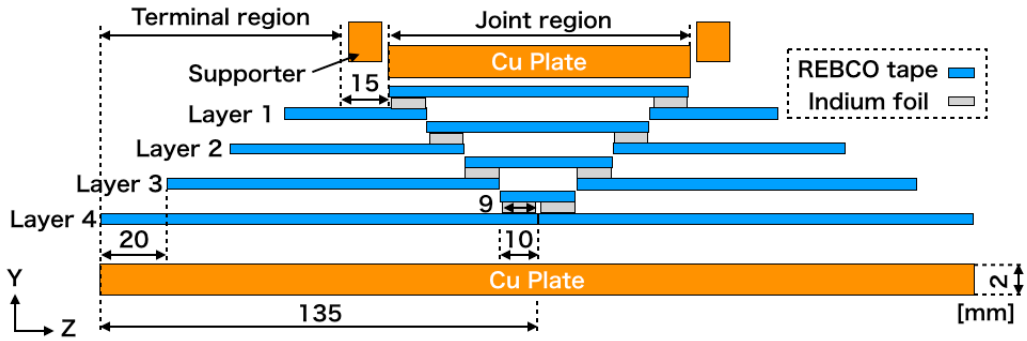

(a) Side view

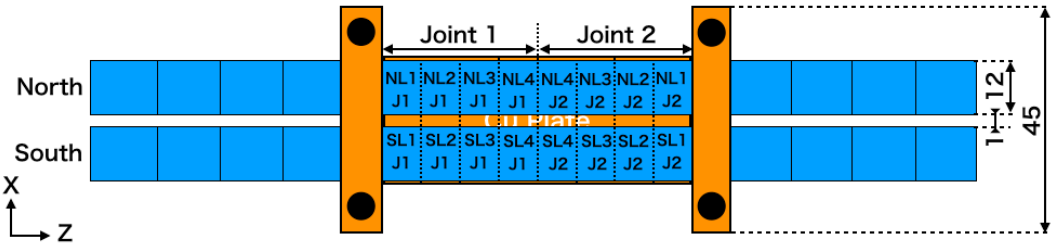

(b) Plane view

Fig. 5.4: Geometry of two-row-four-layer joint sample

and SimpleStack-2, while those with joint-piece procedure were denoted as JointPiece-1, and JointPiece-2.

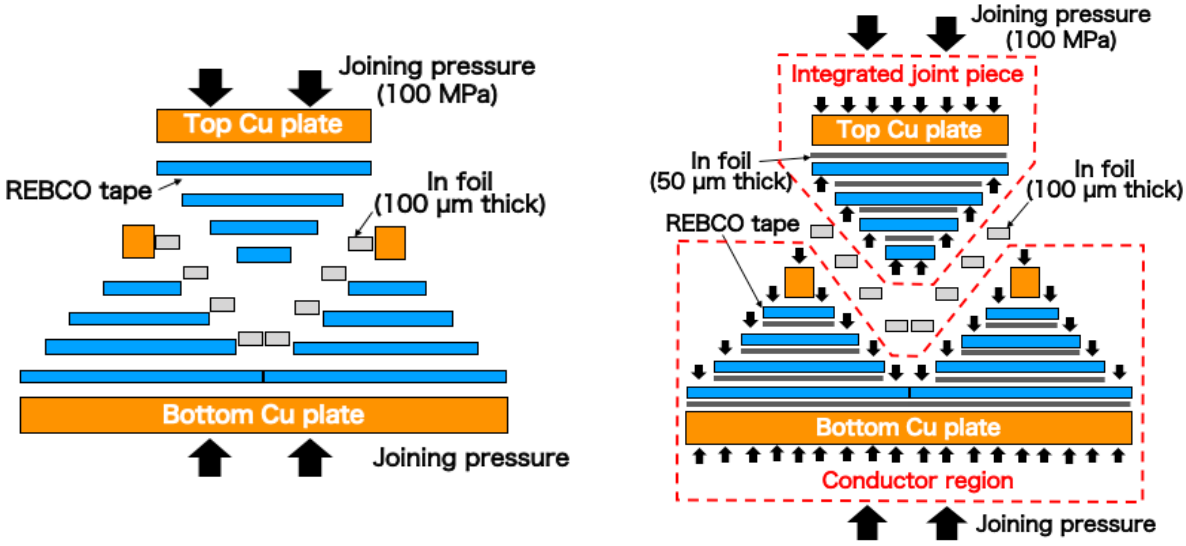

(a) Simple stack procedure (b) Joint piece procedure

Fig. 5.5: Fabrication of two-row-four-layer joint sample

1. Preparation for REBCO tapes and indium foils

   The REBCO tapes and indium foils were clipped with designed geometry. The copper stabilizer's surface of each REBCO tape corresponding to the joint surface was ground with 81 μm diameter of abrasive particle and chemically deoxidized using commercial flux. The joint surfaces of REBCO tapes and indium foils were cleaned with ethanol in advance to joining. Fig. 5.6 shows the all material and tools used for fabricating the two-row-four-

layer joint sample.

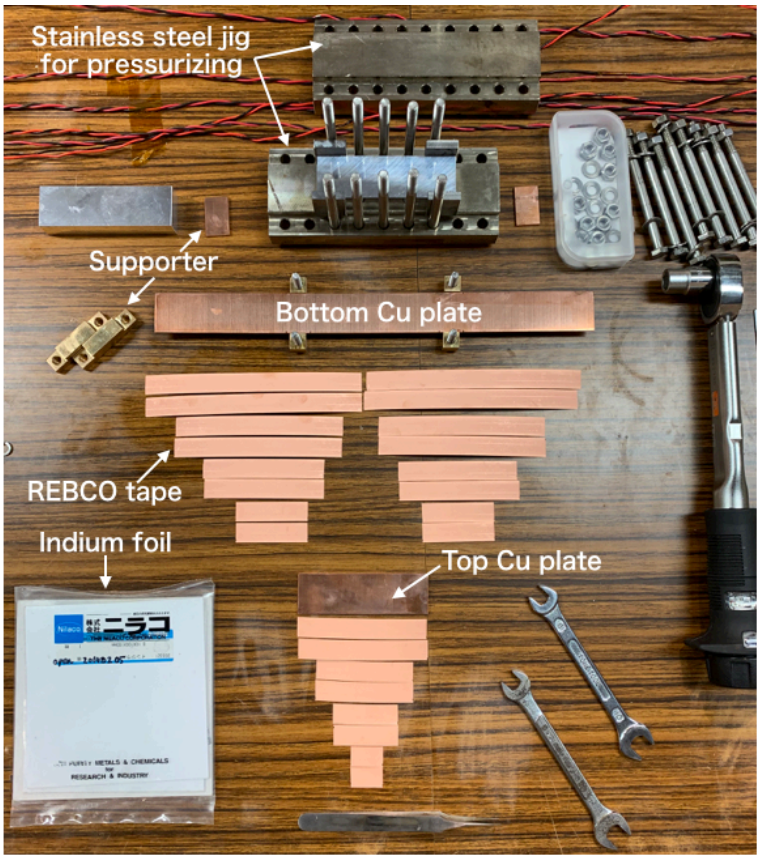

Fig. 5.6: Materials and tools for fabricating one two-row-four-layer joint sample

2. Preparation for joining

- Simple-stack procedure

  The REBCO tapes of all layers on the bottom copper plate were simply stacked firstly, and the supporter was fixed to keep the tapes position. Indium foils of layer 4 were placed on the contact surfaces, then the upper REBCO tape of layer 4 was stacked with the contact surfaces face-to-face. Subsequently, layer 3, layer 2, and layer 1 were stacked in order, and the top copper plate was place on the top of joint section in the last. The total time for preparing was approximately 1 hour. Fig. 5.7 shows the process of stacking at the joint sample with simple-stack procedure

- Joint-piece procedure

  In the joint-piece procedure, the REBCO tapes were bonded on the bottom and the top copper plate using 50-µm-thick indium foils to form conductor region and integrated joint piece. The surface of copper plates were chemically deoxidized using commercial flux, 50-µm-thick indium foils and REBCO tapes were placed on them. Then a set of stainless steel jig sandwiched the aforementioned part, and 40 MPa of pressure was applied with bolting. Whole jig was heated to 170°C using an electric

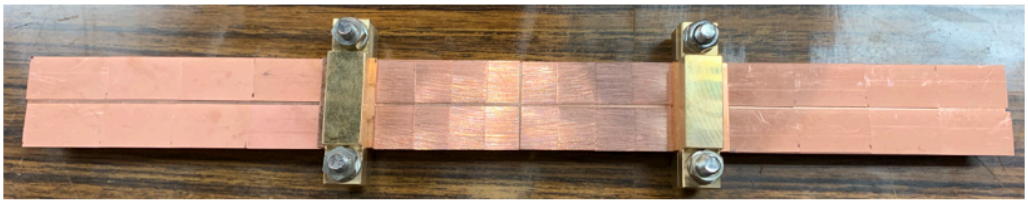

(a) Stacking REBCO tapes on bottom copper plate

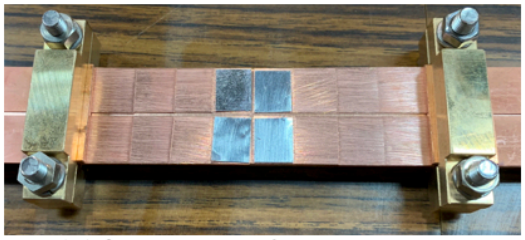

(b) Stack indium foils on layer 4

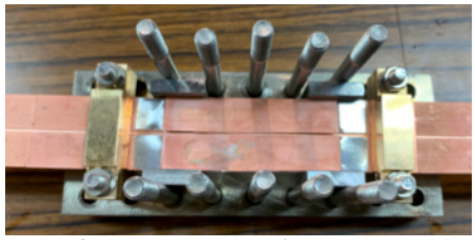

(c) Stacking indium foils on layer 1

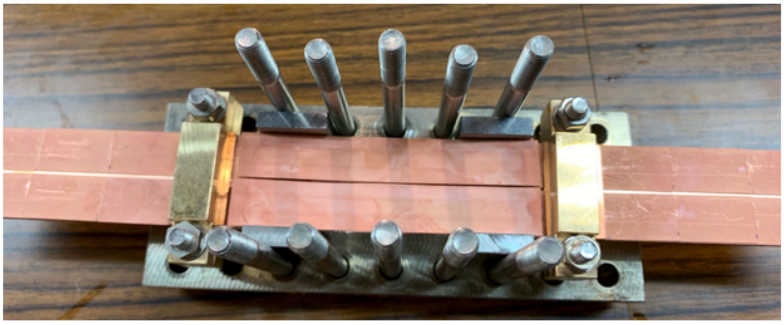

(d) Stacking REBCO tapes on layer 4

Fig. 5.7: Steps of stacking REBCO tapes and indium foils

furnace, and then put the heated parted back to ambient environment to cool down the part to the room temperature. Most of the indium were pushed out by the pressurizing. Since the pressure was applied to all joint area, there was no space for the pushed out indium between the layered REBCO tapes. Approximately 1-µm-thick of indium was remained and the REBCO tapes were fixed on the copper plate. The pushed out indium was removed with a scraper. The sequence of fabricating conductor region was from layer 4 to layer 1, whereas that of integrated joint piece was from layer 1 to layer 4. During the fabrication of each layer, the contact surface of the layer fabricated before was covered with Kapton tapes. After all layers' fabrication finished, the Kapton tapes were taken out, and contact surface were chemically deoxidized and ethanol cleaned. Finally, the 100-µm-thick indium foils were placed on the contact surfaces, and the integrated joint piece was place on the joint section. The total time spent for preparing was more than 8 hours. This time can be shorten to quarter by preparing a jig to press and heat all layers of each part all together in the future. The prepared conductor region and integrated joint piece were shown in Fig. 5.8.

From the Fig. 5.8(a), we could found the a little misalignment between the integrated joint-piece and conductor region. This misalignment can be expected to cause

decrement in contact area, and the increment in applied pressure since the same was applied. However, in the previous study[40] indicated the increased pressure over 100 MPa has little effect on the joint resistance, the condition of experiment was kept the same for convenience.

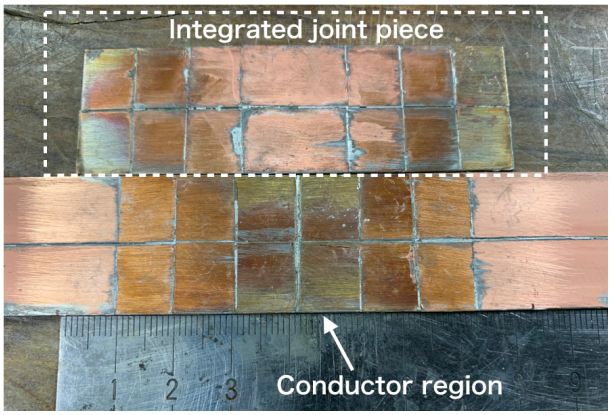

(a) Contact surfaces of JointPiece1

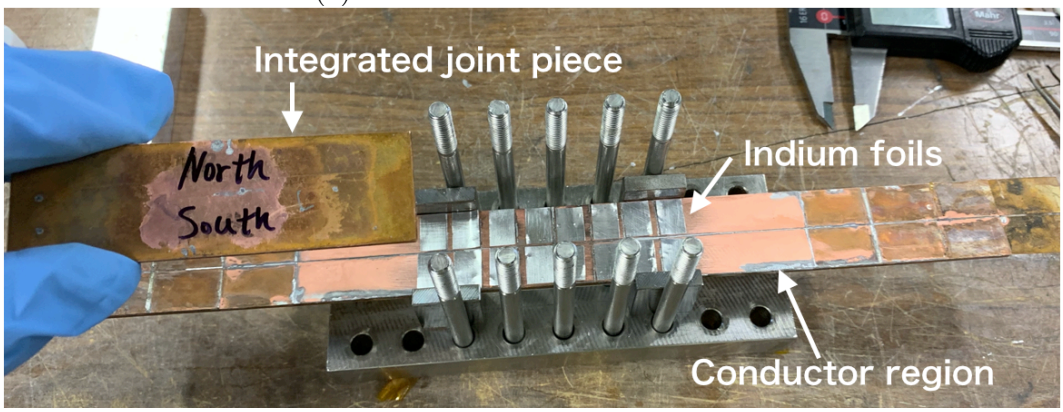

(b)

Prepared integrated joint-piece and conductor region before joining

Fig. 5.8: Joint sample with joint-piece procedure before joining

3. Joining with heating treatment

The prepared joint samples were pressurized with heating treatment. The total joint area was 12 mm $\times$ 10 mm $\times$ 8 $\times$ 2 = 1920 mm^2, the required pressuring force was more than 1.92×10^5 N. 18 stainless steel bolts with a diameter of 6 mm were used to applying the pressure. Each bolts need apply 13 Nm to reach the required pressure at joint according to the Eq. 2.36.

The side view of procedure of bolting set up is illustrated in Fig. 5.9. Aluminum spacer was inserted between the sample and the pressurizing plates to secure enough height for supporter. Due to the interference of supporter parts and bolts, 5 pairs of bolts at the center were bolted at first. At this condition, the sample was holden by the stainless steel plates. Then the supporter parts were removed and the other 4 pairs of bolts were bolted. The support parts were returned after the pressurizing.

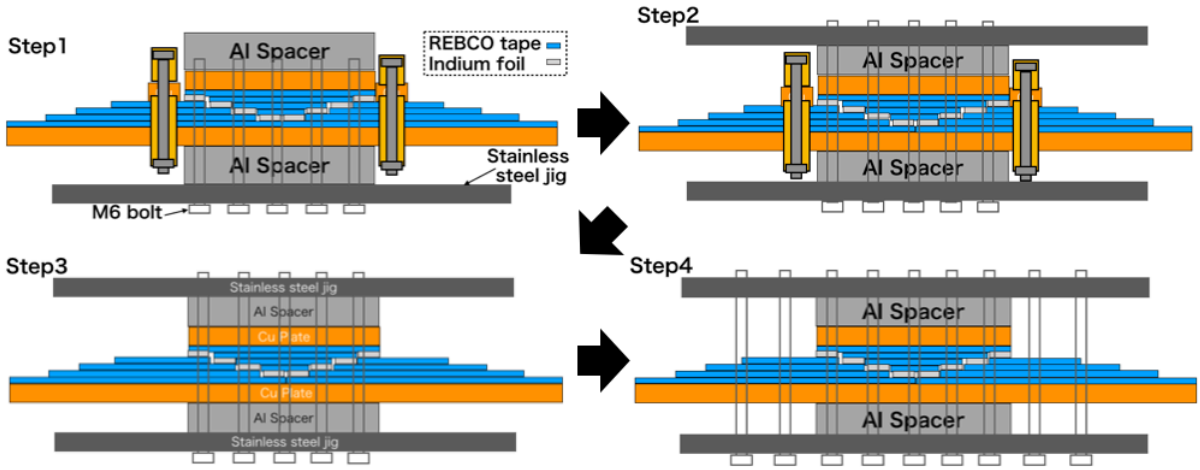

Fig. 5.9: Procedure of bolting

Fig. 5.10: Sequence of bolting

In the bolting, zigzag sequence and stepped torque were applied to prevent the tilted pressurizing. The sequence of bolting was numbered and shown in Fig. 5.10, and the torque was applied with three steps: 3 Nm, 8 Nm, and 13 Nm. After 13 Nm was applied to each bolt, the whole jig was put into the electric furnace for heating treatment. Fig. 5.11 shows the two-row-four-layer joint sample place in the electric furnace. The joint sample was heated to 120°C with monitoring by thermocouple, and kept for 30 minutes. Then the jig was taken out from the electric furnace and the torque of 13 Nm was applied to compensate the stress relaxation resulted from the soften indium. Subsequently the jig was put back to the furnace and heated for another 30 minutes with 120°C. Finally, the sample was taken out and torque of 13 Nm was applied again in ambient environment, and cooled down to the room temperature. The whole process of joining took approximately 3 hours, and this can be shorten by optimizing the heating and cooling method using appropriate designed jig and equipment in the future.

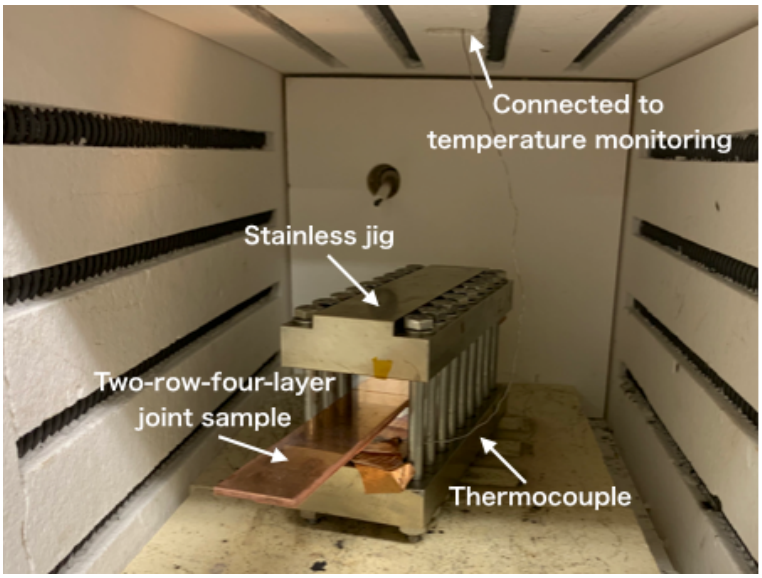

Fig. 5.11: Heating process environment for two-row-four-layer joint sample

5.3 Experimental procedure

5.3.1 Joint resistance measurement

In the measurement of joint resistance each sample was soaked under liquid nitrogen and energized. The configuration for the experiment is described in following sequentially.

- Single-layer lap joint sample

  The single-layer lap joint sample was measured from the current-voltage slope ($I - V$

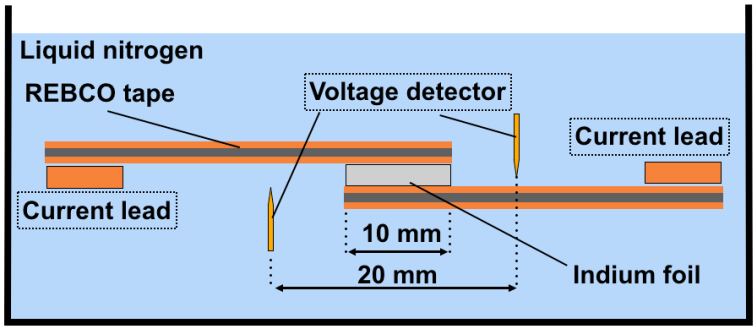

Fig. 5.12: Joint resistance measurement for single layer lap joint sample

curve) with four-terminal method. Fig. 5.12 shows the schematic configuration of the measurement. The two voltage detector were set straddle the joint with a distance of approximately 20 mm to measure the voltages drop though the joint. Currents up to approximately 200 A were applied sequentially, and the current and measured voltage was recorded with a multimeter(2701, Agilent technology). Joint resistance was evaluated by applying the least-squares approach to the measured $I-V$ curve. Each sample were soaked into liquid nitrogen, measured twice, and return to the ambient environment to confirm the reproductivity of the $I - V$ curve.

- Two-row-four-layer joint sample

  In the measurement of two-row-four-layer joint sample, the whole joint sample was cooled using liquid nitrogen and energized layer by layer. Fig. 5.13 illustrated the schematic configuration of joint resistance measurement when the current was applied to the layer 3 of south row. Ten pair of attachable potential probes were used for simultaneously picking up the voltage drop across each layer, top copper plate and bottom copper plate to monitor current sharing. The currents up to 100 A were applied to each layer, and the current and voltages were recorded using a multimeter. The joint resistance of each layer are the sum of two single lap joints, and solved from a simultaneous equations of measured voltages explained following. The current was applied to each layer twice to confirm reproductivity of the measurement. Fig. 5.14 shown the actual experimental setup for joint resistance measurement of tow-row-four-layer joint sample

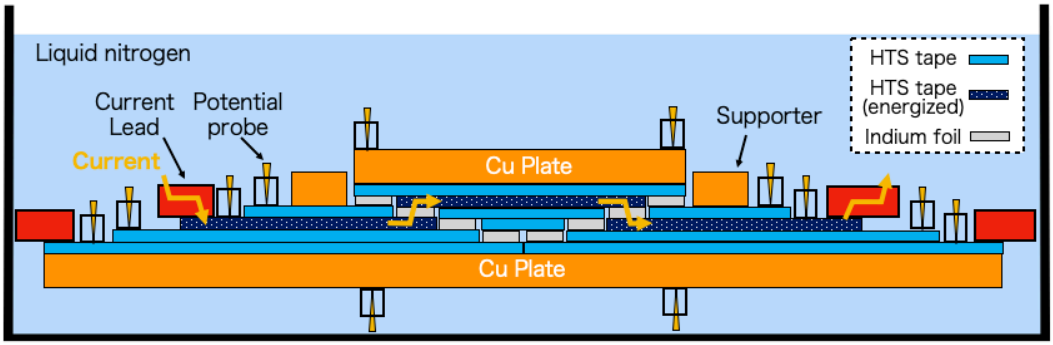

(a) Side view of joint resistance measurement

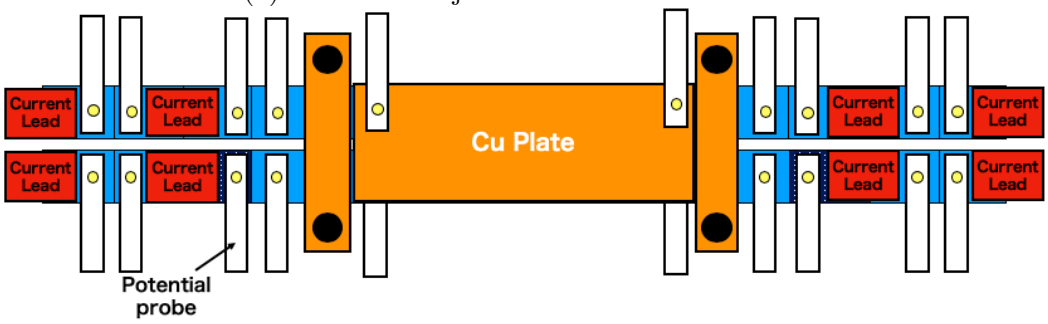

(b) Plane view of joint resistance measurement

Fig. 5.13: Schematic configuration of joint resistance measurement for two-row-four-layer joint sample

5.3.2 Contact interface evaluation using X-ray CT scan

- Single layer lap joint sample

For the single-layer lap joint sample with 12-mm-wide REBCO tapes, micro-focus X-ray CT scanner (ScanXmate-D225RSS270, Comscantecno Company Ltd., Yokohama, Japan) was used to observed the contact interfaces. Fig. 5.15 shows the experimental set up for X-ray CT scan. The X-ray tube voltage and X-ray tube current were 225 kV and 200 µA, respectively. 2-mm-thick of copper plate was used for the filter. The number of projection

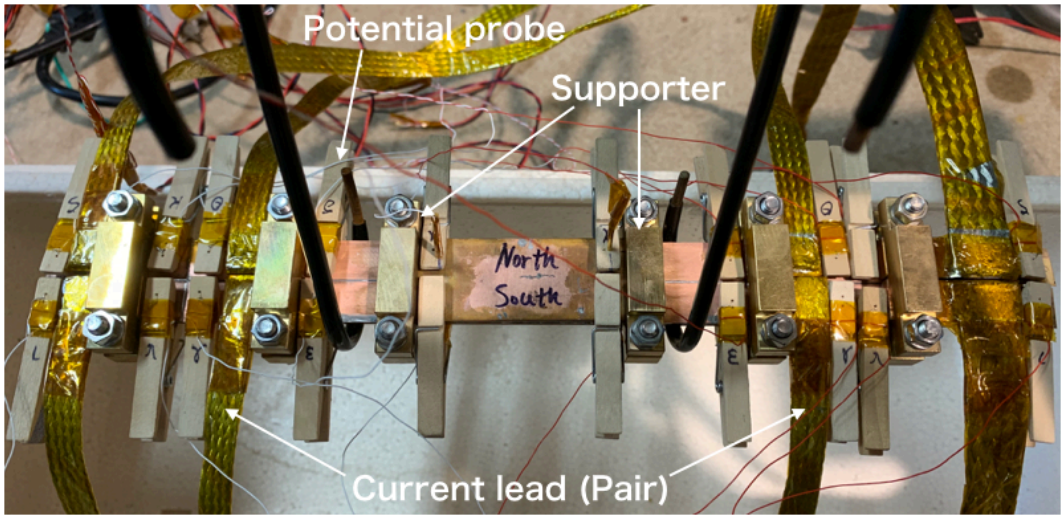

Fig. 5.14: Joint resistance measurement for two-row-four-layer joint sample

was set to 1000. The obtained three-dimensional CT data consist of $928 \times 736 \times 736$ voxels, and the size of the voxel was 33.208 µm/pixel The self-developed program 4.6 was used to extract the cross-sectional images of contact interfaces.

- Two-row-four-layer joint sample

For the two-row-four-layer joint sample, an high energy X-ray CT scanner with higher sensitivity X-ray detector are needed because the wider and thicker composition of the joint sample attenuate the X-ray. Micro-focus X-ray CT scan (TXS-300 TESCO corp., Kanagawa, Japan) was used The joint sample was set as Fig. 5.16 inside the X-ray CT scan. The X-ray tube voltage and X-ray tube current were set to be 230 kV and 180 µA, respectively. A copper filter with 0.5 mm thickness was used. The number of projection was 2000, and obtained resolution was 20.9 µm/pixel. A free viewer software myVGL [73] was utilized to cut out the cross-sectional images of the contact interfaces.

5.3.3 Joint thickness measurement

For the single-layer joint sample, the thickness of each joint was measured using micrometer(MDC-25SB, Mitutoyo corp., Kanagawa, Japan) after the joint resistance measurement and X-ray CT scan. Six random point at each joint section was selected and measured, the average of the six value was utilized as joint thickness. Then the resulting indium thickness is calculated from the joint thicknesses subtracting two REBCO tapes (for each is 0.942 mm thick).

For the two-row-four-layer joint sample with simple-stack procedure, each layer can be disassembled since the REBCO tapes were not fixed. Meticulous care was paid on the disassembly operation , the SimpleStack-1 and SimpleStack-2 were disassemble to each layer as shown in Fig. 5.17. Because of the possibility for deteriorating the contact condition, the samples were disassembled after the joint resistance measurement and X-ray CT scan. Then the thickness was measured at each lap joint using micrometer.

For the two-row-four-layer joint sample with joint-piece procedure, the thickness between two copper plates was measured because the REBCO tapes were completely fixed. the joint section was segmented as the Fig. 5.18, and thickness of romdom six points at each corresponding joint area was measured as joint thickness. The resulting indium thickness was obtained by subtracting thicknesses of copper plates and five REBCO tapes from the joint thickness. Due to the difficulty of the accessibility to the single lap joint, the uncertainty of the resulting indium thickness is considered to be the highest in the JointPiece-1 and JointPiece-2.

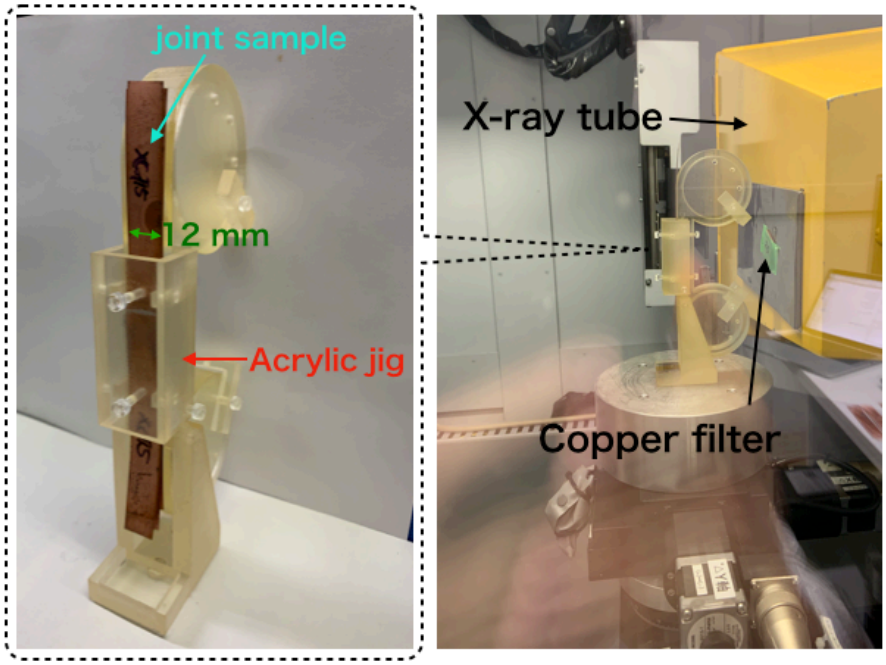

Fig. 5.15: X-ray CT scan set up for single-layer lap joint with 12-mm-wide REBCO tape

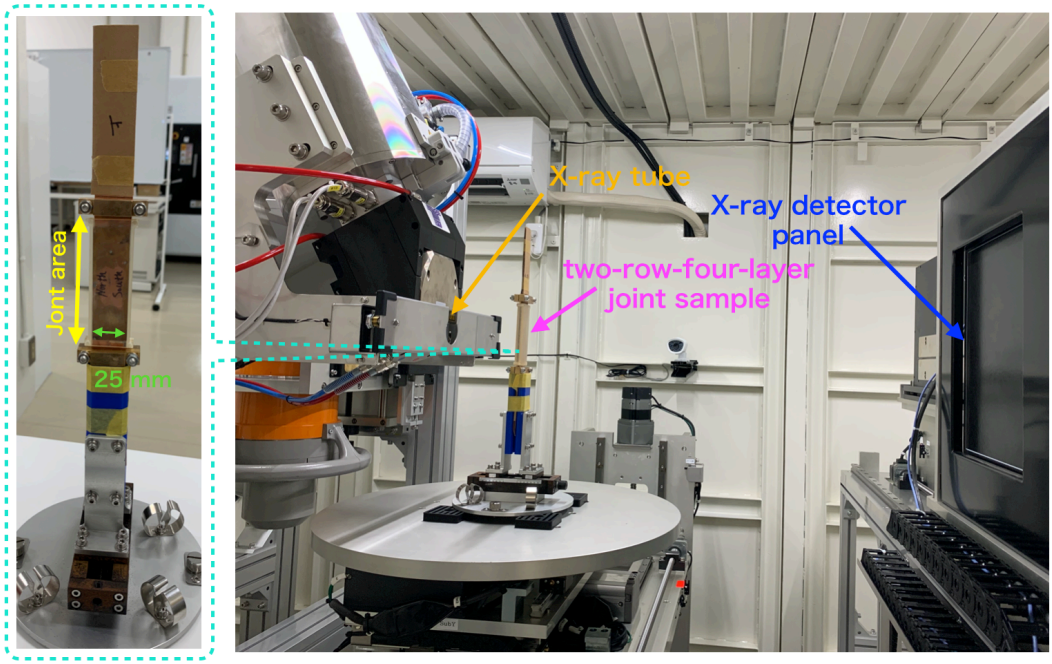

Fig. 5.16: X-ray CT scan set up for two-row-four-layer joint sample

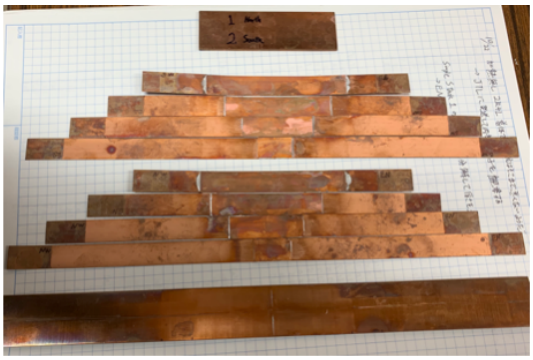

(a) Disassembled SimpleStack-1

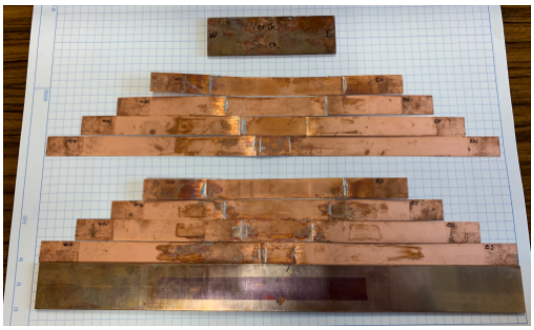

(b) Disassembled SimpleStack-2

Fig. 5.17: Disassembled tow-row-four-layer joint samples with simple-stack procedure

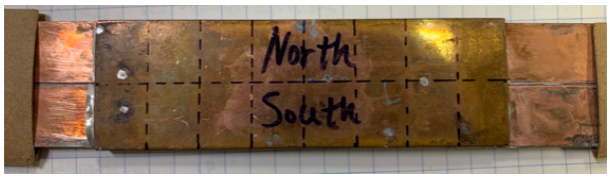

Fig. 5.18: Segmented area at joint section

5.4 Experimental result

5.4.1 Result of single-layer lap joint sample

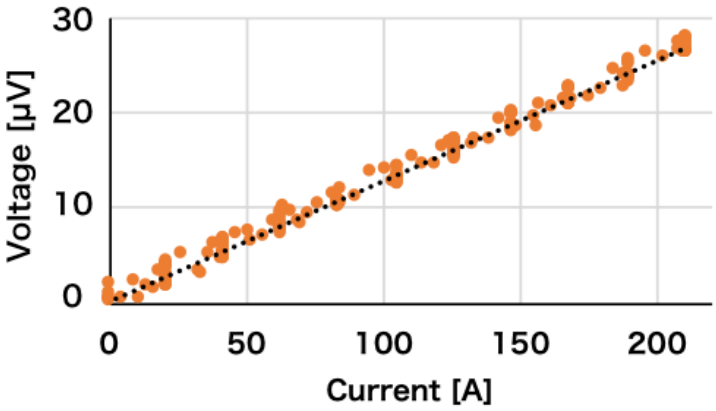

Fig. 5.19: $I-V$ curve of sample SingleLap5

The measured $I-V$ curve of sample SingleLap5 is shown in Fig. 5.19 as an example. The least-squares method was applied to calculate the approximate curve at black dot line, and the gradient of the line is the joint resistance.

In the evaluation of contact area, the same technique explained in section 4.6 was used. The cross-sectional image of a contact interface from sample SingleLap5 is shown in Fig. 5.20 (a). The segmented area as 5.20(b) displays the segmented area that corresponding to the contact area. Each sample conducted three times of segmentation, and the average value was used as the contact area.

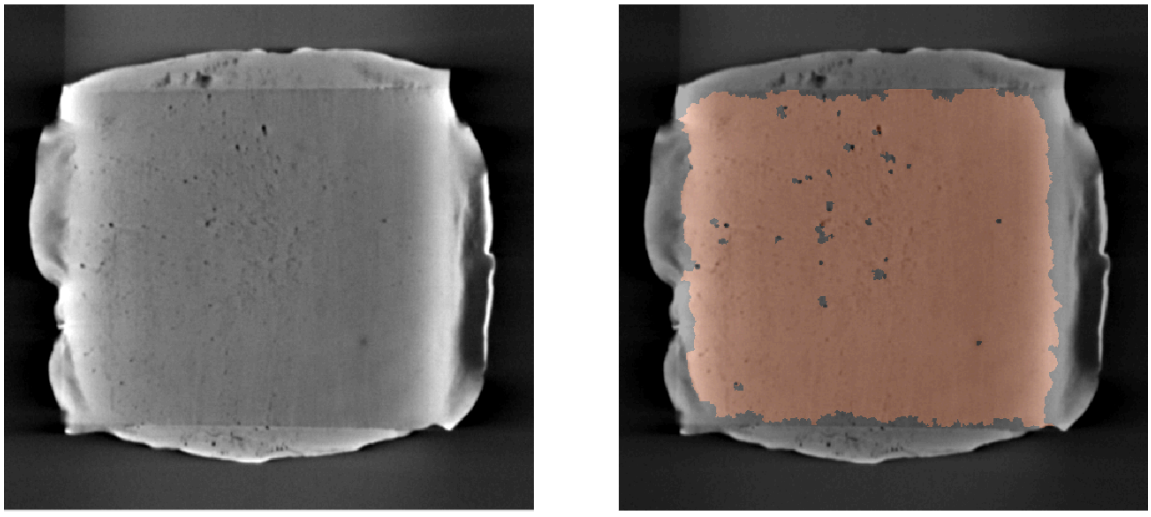

(a) Cross-sectional image of sample SingleLap5 (b) Segmented contact area of SingleLap5

Fig. 5.20: Disassembled tow-row-four-layer joint samples with simple-stack procedure

The measured joint resistance, resulting indium thickness, and evaluated contact area of each single-layer joint sample were listed up in Table 5.1. Noting that the resulting indium thickness

shows little decrement since the temperature of heating process was lower than the melting point of indium. The effect of heating process is to soften the indium but not to melt it.

Table. 5.1: Experimental results of single-layer lap joint sample

Sample name	Joint resistance (μΩ)	Thickness of Resulting indium (μm)	Contact area (mm^2)
SingleLap1	0.155	98.5	99.6
SingleLap2	0.138	94.0	120.2
SingleLap3	0.158	83.8	111.9
SingleLap4	0.123	100.0	115.0
SingleLap5	0.129	86.0	120.3
SingleLap6	0.126	83.7	107.4
SingleLap7	0.125	75.7	114.5
SingleLap8	0.151	76.5	102.2

5.4.2 Joint resistance measurement of two-row-four-layer joint sample

In the evaluation of joint resistance, one layer was energized and ten points of voltages was monitored. A measurement result from the condition that NL2 of JointPiece-1 was energized is shown in Fig. 5.21. The X-axis is the time steps. The current was raised to 100 A in a stepwise procedure as plotted with green triangle, while the voltage of measured voltage increased following the increment of current. Although only layer NL2 was energized, the increasing of voltage was found not only in layer NL2 but also in layer NL1.

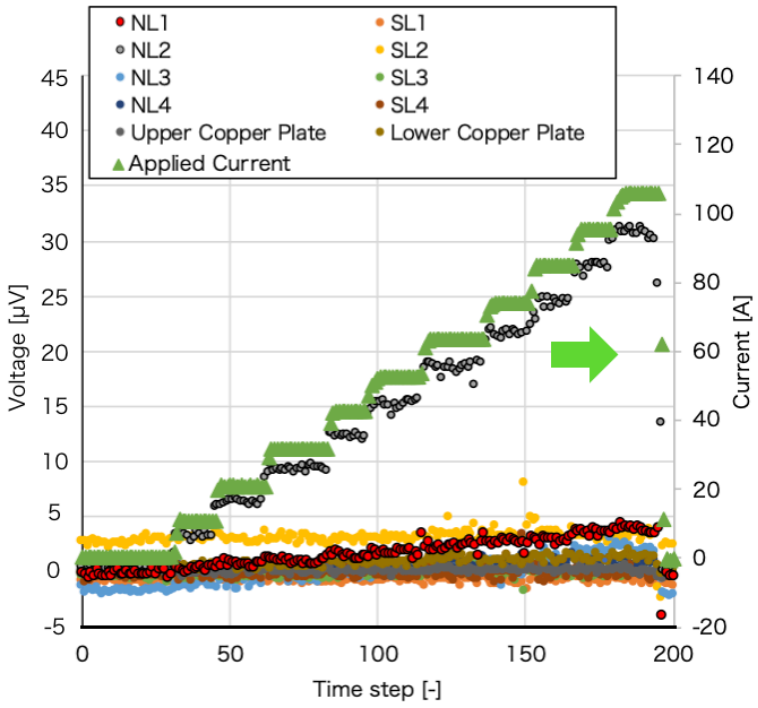

Fig. 5.21: Raw measurement data

This phenomena happens because of the current Leakage, or current bypassing other layers.

Aside from the main current path in layer NL2, other two current path at the joint can be considered as shown in Fig. 5.22. The pattern 1 is the current cross the interface between the NL2 and NL1 and reached the REBCO layer of NL1. Then the leaked current flows the the joint of NL1. The other case is the current leak to layer NL1 and NL3 through the indium at the joint. This is because the pressuring with heat treatment during the sample fabrication soften and plastically deform the indium foil to a unified and connected indium circuit. In case the current leak to other layers, the actual current passing the energized layer became less, and the joint resistance calculated from total applied current and measured voltage would result in an underestimated valued of joint resistance. A compensation modification to obtain accurate joint resistance was needed.

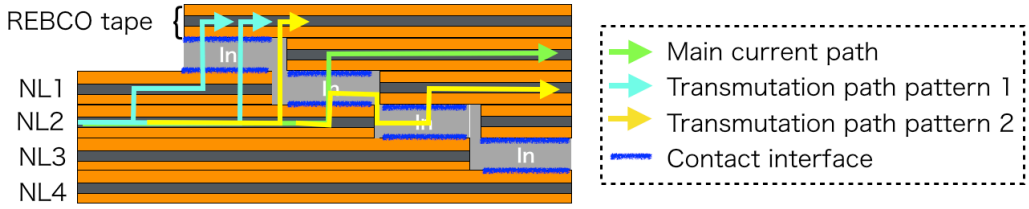

Fig. 5.22: Assumption for current Leakage path

A comprehensive method for the joint resistance calculation using simultaneous equations was considered. Because the rigorous current leakage path is too variable to identify, only the joint was assumed to cause the increment of the voltage at the layer that was confirmed to carry the leaked current. The resistance of the current cross the interface of the layers and the thin cross section of the indium would increase the total resistance of the actual leaked current path. The assumption applied above would result in relatively high current leakage, low main current, and overestimation of joint resistance at energizing layer. Since the overestimating joint resistance is the side of prudence, evaluating using the calculated joint resistance was considered to be applicable.

The detail of simultaneous equations for calculating joint resistance is expressed following. Using subscripted i to distinguish layer, and in case the layer l was energized, the measured voltage of individual layer $i(V_{i,l})$, voltages of top and bottom copper plates($V_{\mathrm{CuTop}l}$ and $V_{\mathrm{CuBottom}l}$) and total applied current, $I_{\mathrm{total}l}$, can be expressed as

$$V_{i,l} = R_i \times I_{i,l} \tag{5.1}$$

$$V_{\mathrm{CuTop}l} = R_{\mathrm{CuTop}} \times I_{\mathrm{CuTop}l} \tag{5.2}$$

$$V_{\mathrm{CuBottom}l} = R_{\mathrm{CuBottom}} \times I_{\mathrm{CuBottom}l} \tag{5.3}$$

$$I_{\mathrm{total}l} = \sum_{i=1}^{8} I_{i,l} + I_{\mathrm{CuTop}l} + I_{\mathrm{CuBottom}l} \tag{5.4}$$

where the $I_{i,l}, I_{\mathrm{CuTop}l}, I_{\mathrm{CuBottom}l}$ are the current of layer number i, top copper plate, bottom

copper plate, respectively. R_{CuTop} and R_{CuBottom} were known. The resistance of each layer, R_i, corresponding to joint resistance of each numbered layer. R_i was calculated from current-voltage slope ($I-V$ curve) by applying the least squares approach with iteration. Fig. 5.23 shows the variation of the joint resistance before and after the current leakage compensation modification. The significant variation of joint resistance from JointPiece-1 and JointPiece-2 can be confirmed, whereas the SimpleStack-1 and SimpleStack-2 has slightly or no variation. The more variation happened, the more current leak to other other layers. The reason for the joint samples with joint-piece procedure has high current leakage is considered to be the process of fixing the REBCO tapes significantly decreased the resistance at interface between the layers. The ease of current leakage could be also interpreted as a merit of saving the REBCO tape from quench caused by overflowed current.

The modified joint resistance of each layer from each joint sample were listed in Table. 5.2 and used in following analysis.

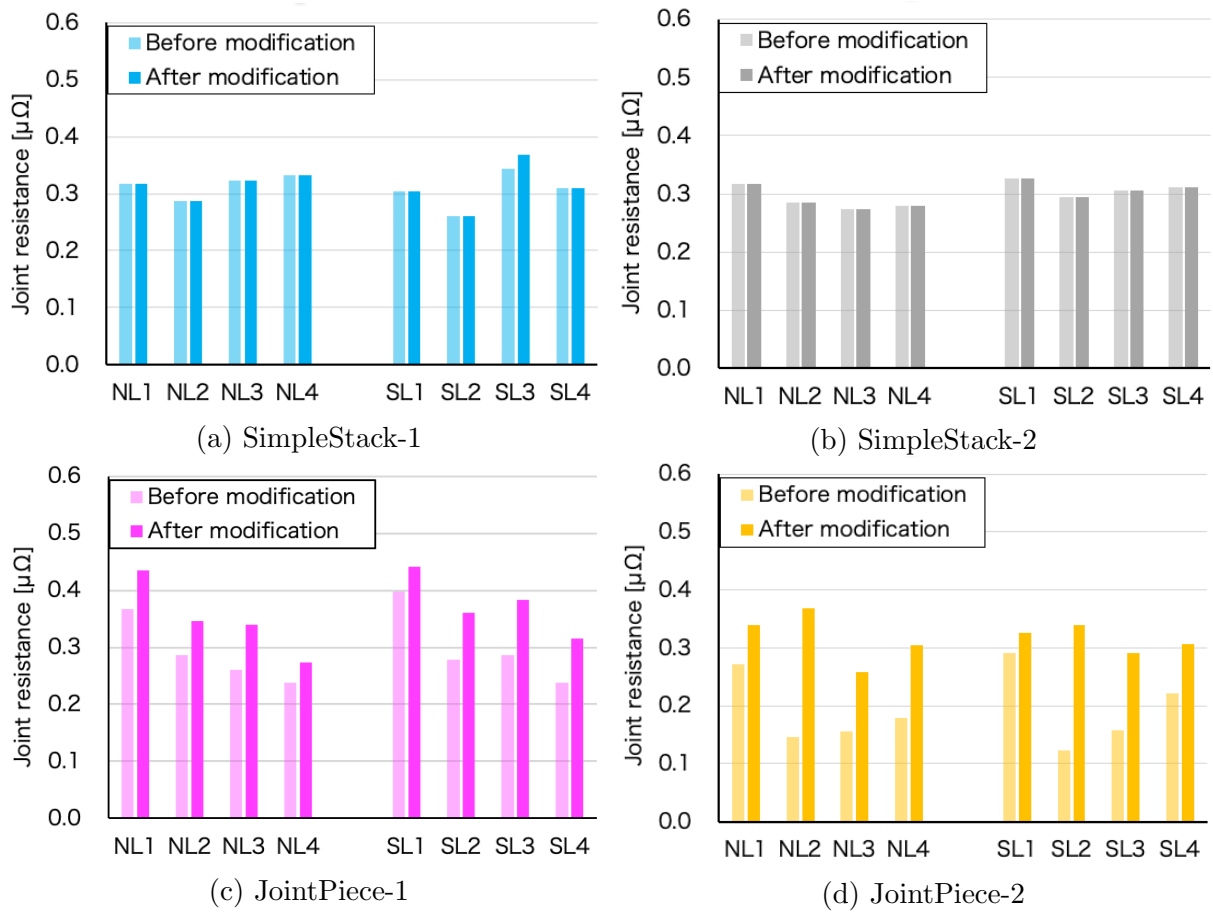

(a) SimpleStack-1

(b) SimpleStack-2

(c) JointPiece-1

(d) JointPiece-2

Fig. 5.23: Joint resistance before and after the compensation modification

Table. 5.2: Joint resistance of two-row-four-layer joint sample

Layer name	Joint resistance of SimpleStack-1 (μΩ)	Joint resistance of SimpleStack-2 (μΩ)	Joint resistance of JointPiece-1 (μΩ)	Joint resistance of JointPiece-2 (μΩ)
NL1	0.317	0.317	0.435	0.339
NL2	0.288	0.285	0.347	0.368
NL3	0.323	0.273	0.340	0.229
NL4	0.333	0.280	0.273	0.305
SL1	0.305	0.326	0.442	0.326
SL2	0.260	0.294	0.360	0.339
SL3	0.369	0.305	0.383	0.292
SL4	0.310	0.311	0.316	0.307

5.4.3 Contact area evaluation of two-row-four-layer joint sample

The operation screen of myVGL is shown in Fig. 5.24. The arbitrary cross-sectional images can be extracted.

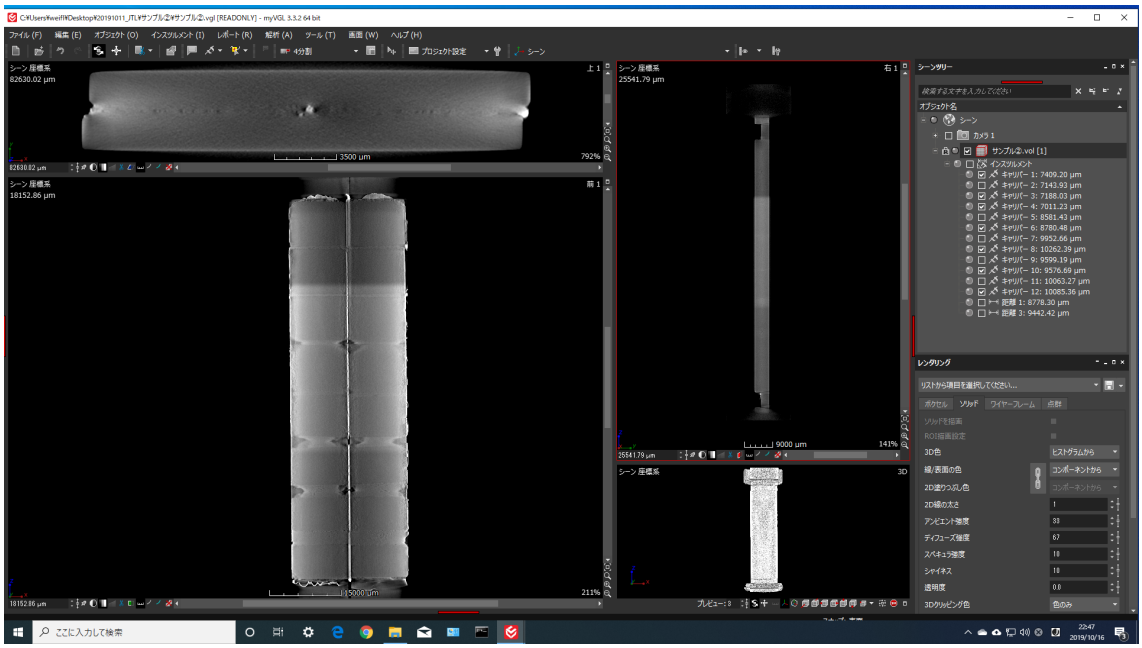

Fig. 5.24: Acquired X-ray CT images of two-row-four-layer joint sample using myVGL

The location of cross-section are shown in Fig. 5.25, an example at cross-sectional images of contact interface is shown in Fig. 5.26 The extracted image was segmented using the procedure explained in section— 4.6, and the segmented contact area is colored in Fig. 5.26(b). Noting that even the resolution of X-ray CT scan was 0.0209 mm/pixel, the extracted imaged was modified by the enlargement factor accordingly. The resolution is needed to be compensated, and the compensate coefficient, α is expressed by Eq. 5.5

$$\alpha = \frac{25.4[\mathrm{mm/inch}] \div \mathrm{DPI[pixel/inch]}}{\mathrm{Resolution[mm/pixel]} \times \gamma} \tag{5.5}$$

where γ is enlargement factor of the observed image, and DPI is resolution of the extracted image (dots per inch).

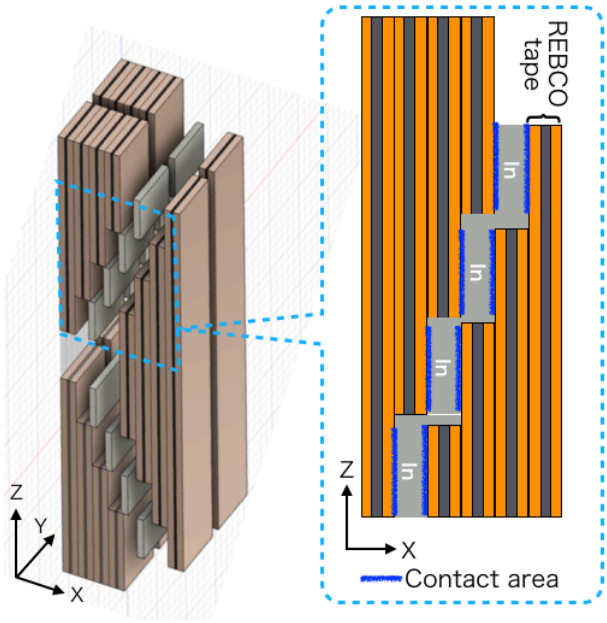

Fig. 5.25: Contact interfaces of two-row-four-layer joint sample

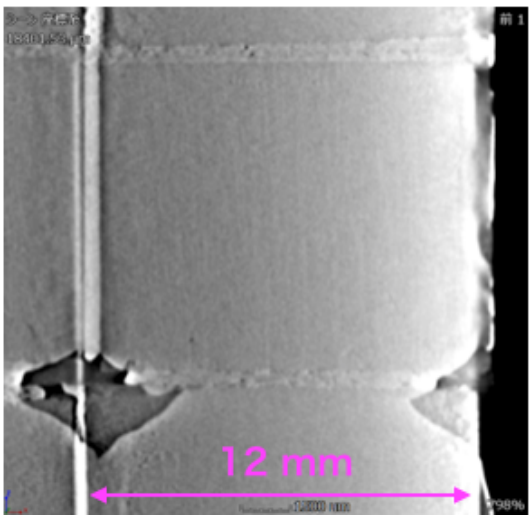

(a) Extracted cross-sectional image

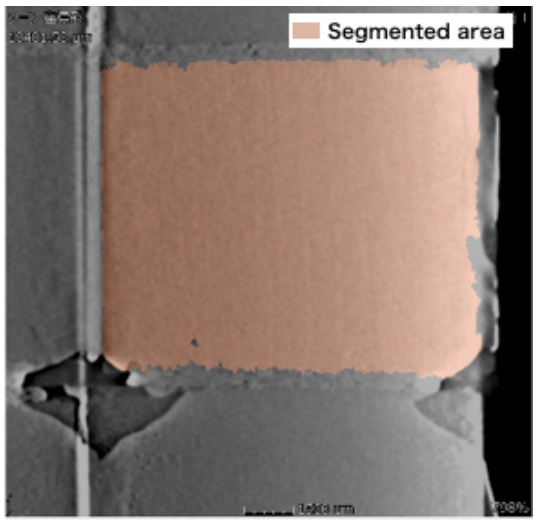

(b) Segmented contact area

Fig. 5.26: Cross-sectional images of contact interface at south row layer 3 joint 2 from JointPiece-1

The Fig. 5.27 - 5.30 displayed the segmented contact area of each contact area from each two-row-four-layer joint sample. The all contact area lower than the conventional contact area 120 mm^2, which is calculated by multiplying the original joint length and REBCO tape width. The reason caused by the shortage of contact area is considered to be the misalignment of joining, in other word the joint length in real was less than the original joint length due to the misalignment of fabrication.

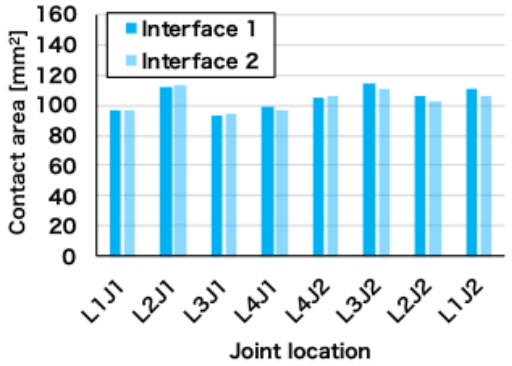

(a) North row

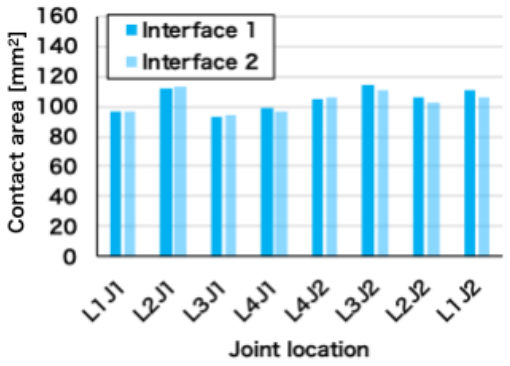

(b) South row

Fig. 5.27: Contact area of SimpleStack 1

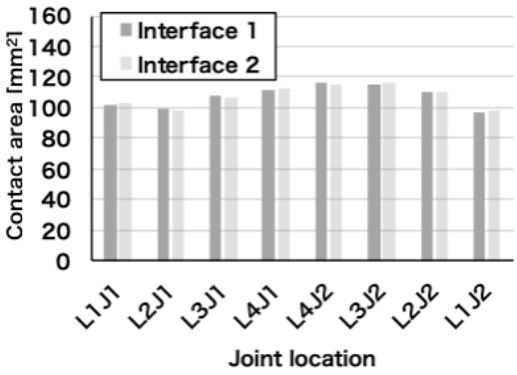

(a) North row

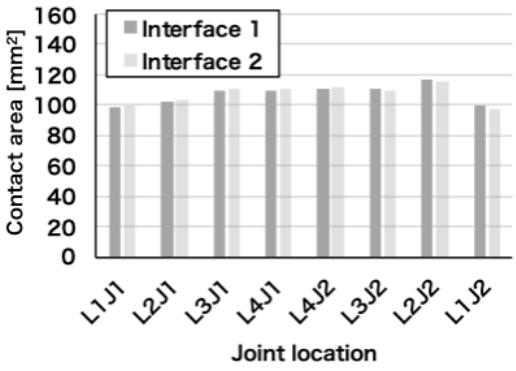

(b) South row

Fig. 5.28: Contact area of SimpleStack 2

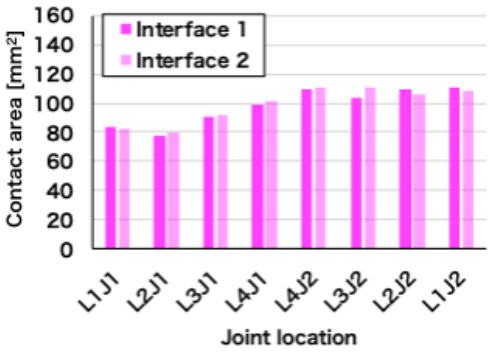

(a) North row

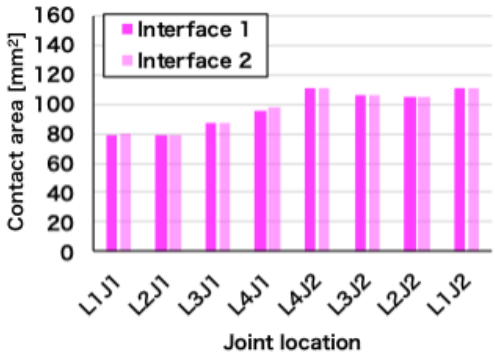

(b) South row

Fig. 5.29: Contact area of JointPiece 1

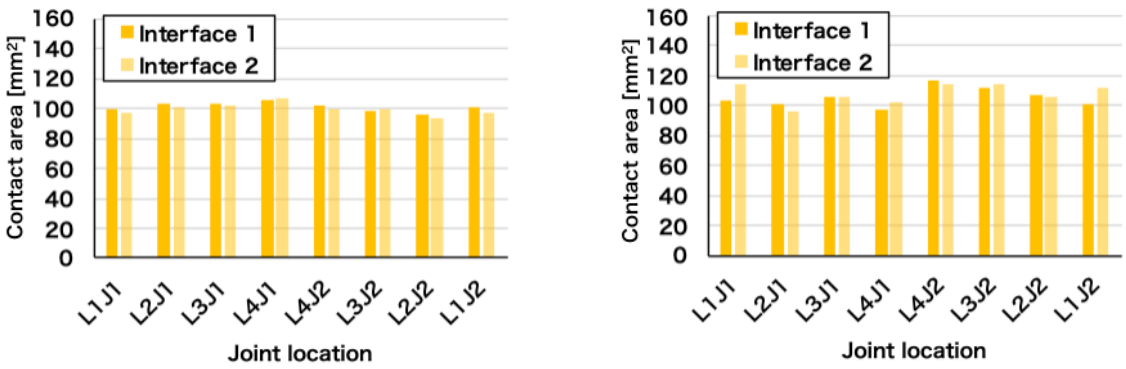

(a) North row (b) South row

Fig. 5.30: Contact area of JointPiece 2

To validate the assumption, the lengths at center of the joint in longitudinal direction (actual joint length) were evaluated from the contact interface images and compared with contact area as shown in Fig. 5.31. The comparison show high correlation between actual joint length and contact area. The reason for general shortage is result from the misalignment of fabrication. Since the evaluation of contact resistivity using the contact area that actual contact, the shortage of contact area would not influence but improve the accuracy of contact area.

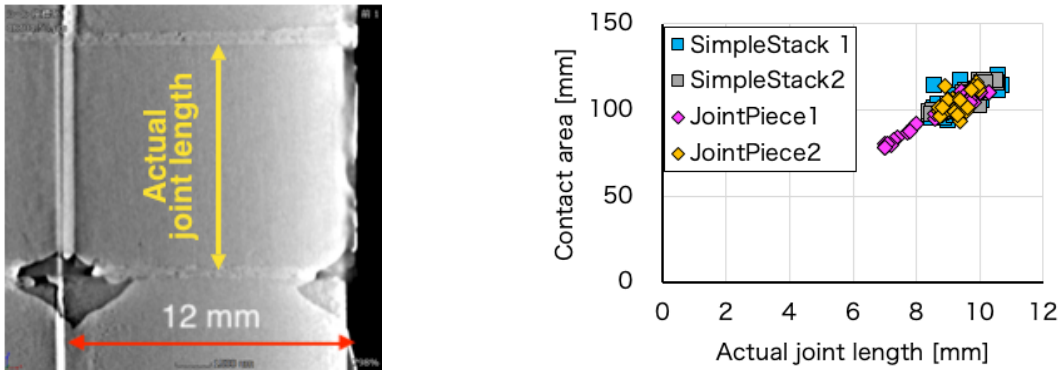

(a) Definition of actual joint length (b) The comparison

Fig. 5.31: Comparison between actual joint length and contact area

5.4.4 Resulting indium thickness of two-row-four-layer joint sample

The resulting indium thickness of each joint sample was shown from Fig. 5.32 to Fig. 5.35. The thickness of the indium is generally less than the original thickness of 100 µm due to the plastic deformation. The joints at layer 3 Joint 1 of SimpleStack 2 was extraordinary thicker than other joints, and continuous tendency of thickness distribution can be found around this joints. At these joint, extruded indium could be found cover the copper surface of REBCO tape as shown in Fig. 5.36. Although the extruded indium was chipped using a razor carefully, the resulting indium on the surface still have influence on the thickness of micro-order. The value of these layers are not accurate to discussed and evaluate. Therefor the range from 0 mm thickness of resulting indium was considered and the range of the contact resistivity was calculated in these layers.

Considering the joining pressure is one of the most important factors to the contact resistance, which induces plastically deformation of indium foil, the contact resistivity is needed to compare with the resulting indium thickness.

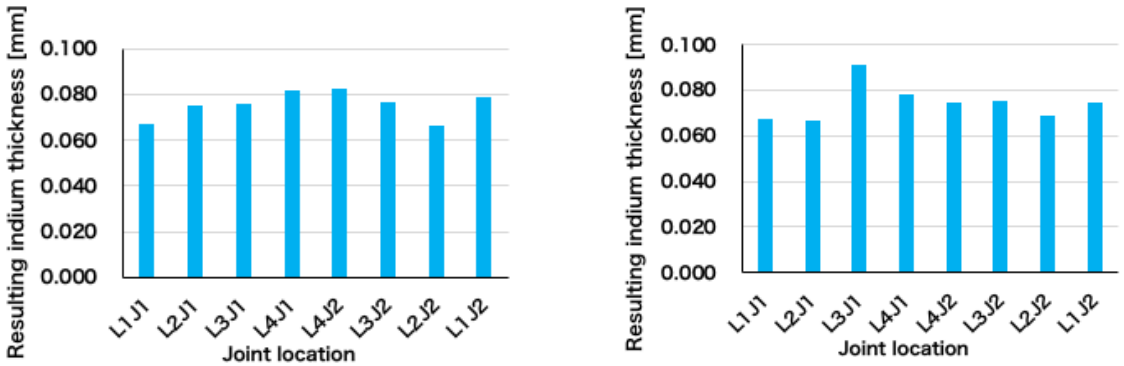

(a) North row (b) South row

Fig. 5.32: Resulting indium thickness of SimpleStack 1

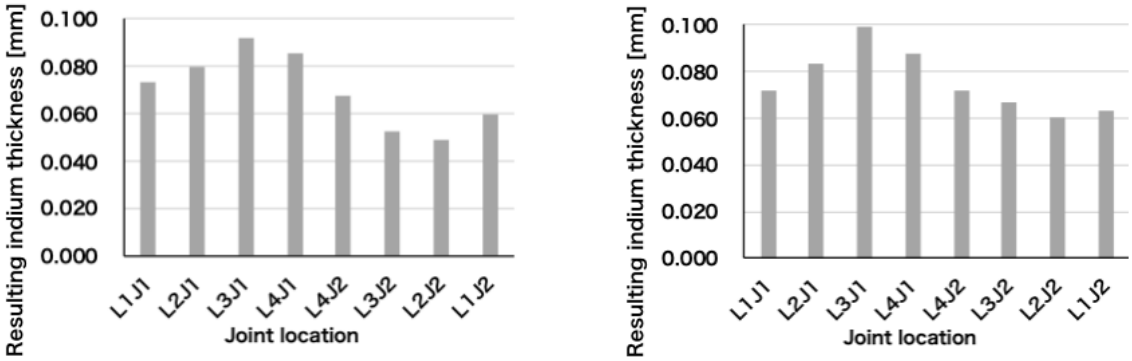

(a) North row (b) South row

Fig. 5.33: Resulting indium thickness of SimpleStack 2

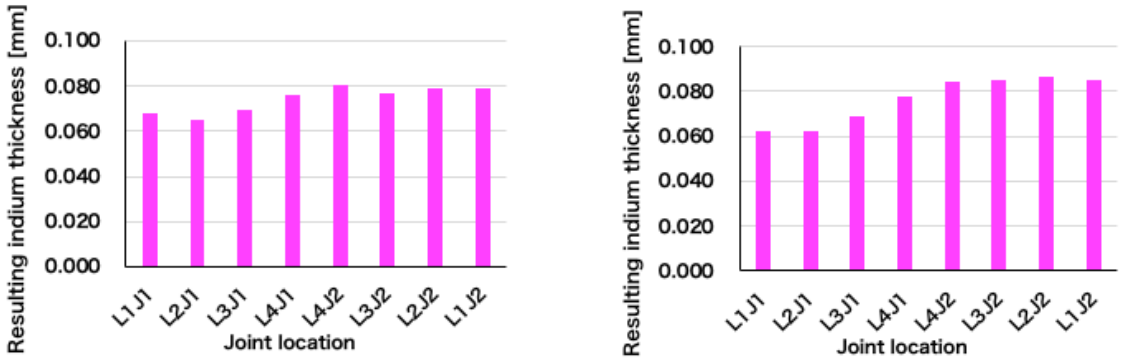

(a) North row (b) South row

Fig. 5.34: Resulting indium thickness of JointPiece 1

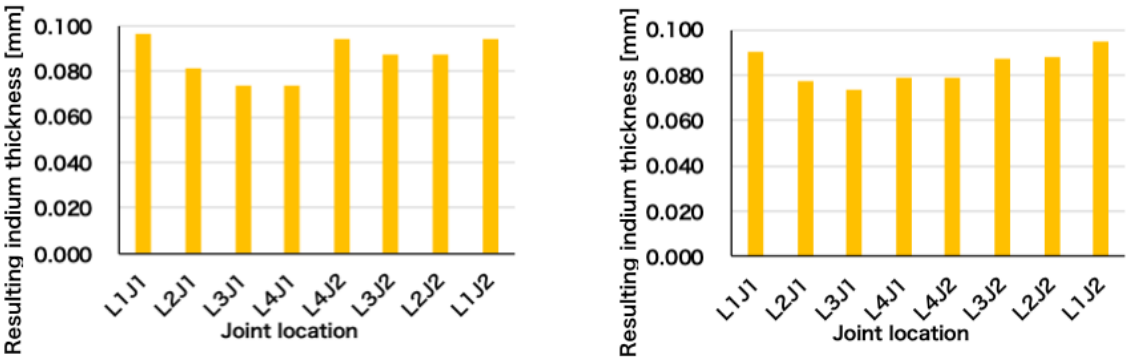

(a) North row (b) South row

Fig. 5.35: Resulting indium thickness of JointPiece 2

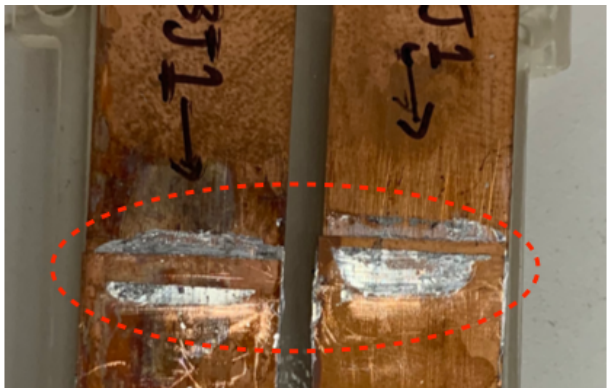

Fig. 5.36: The top surface of joint section at layer 3 joint 1 from SimpleStack 2

5.4.5 Analysis for abnormal cross-sectional images of two-row-four-layer joint sample with simple-stack procedure

During the analysis of cross-sectional images, several abnormal pattern was found in both row at the layer 3 joint 1 of SimpleStack2. Fig. 5.37shows normal cross-section images taken from SimpleStack1 and Fig. 5.38 shows the abnormal images. The lines pointed by red arrows should not be seen unless other material existed.

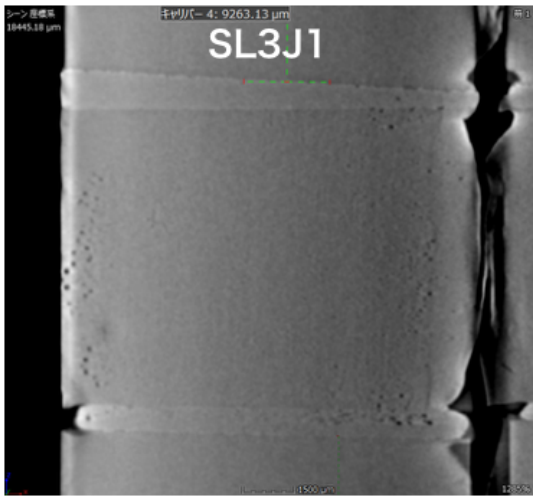

(a) Cross-sectional image of SL3J1

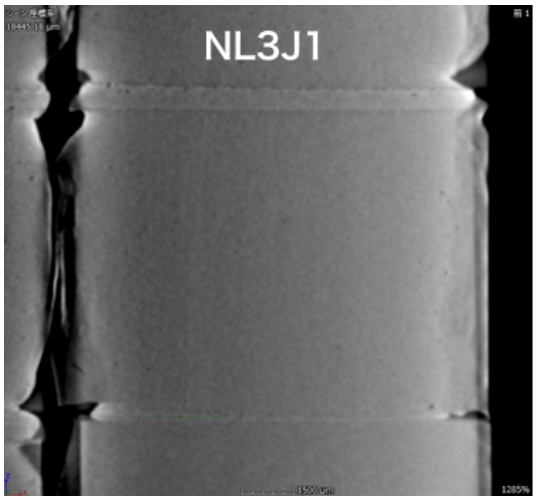

(b) Cross-sectional image of NL3J1

Fig. 5.37: Crosse-sectional images of contact interface at layer 3 joint 1 of SimpleStack 2

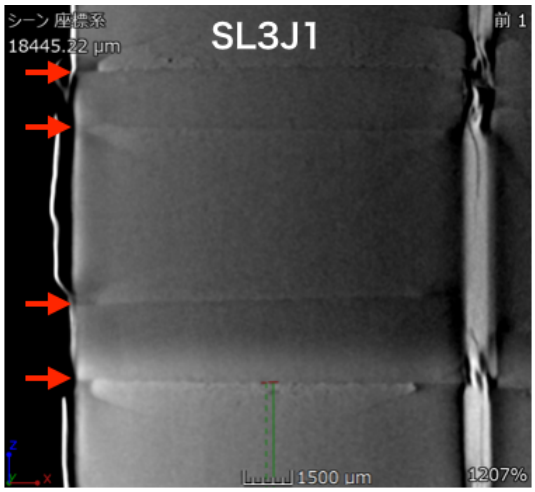

(a) Cross-sectional image of SL3J1

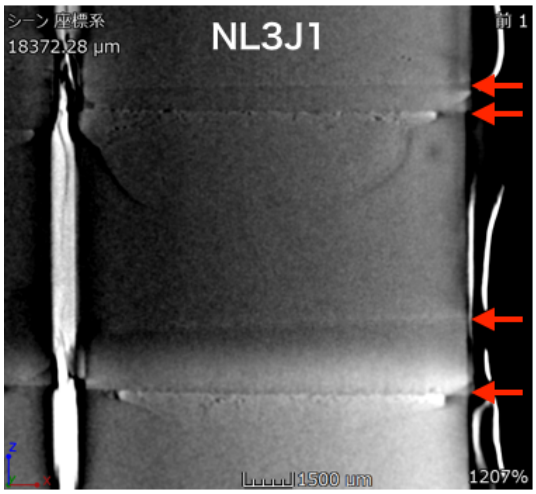

(b) Cross-sectional image of NL3J1

Fig. 5.38: Crosse-sectional images of contact interface at layer 3 joint 1 of SimpleStack 2

The top surface of contact area is shown in Fig. 5.36. The extruded indium partially covered the top surface of the joint section, and these indium created the beam hardening and scattering artifact and projected to the cross-sectional images at contact interfaces. However, the top surface should contact with bottom surface of layer 2, and the extruded indium should not jump to the inner area at joint section. To unveil the cause of this phenomenon, the disassembled SimpleStack2 was restored to the configuration during the X-ray CT scan as Fig. 5.39.

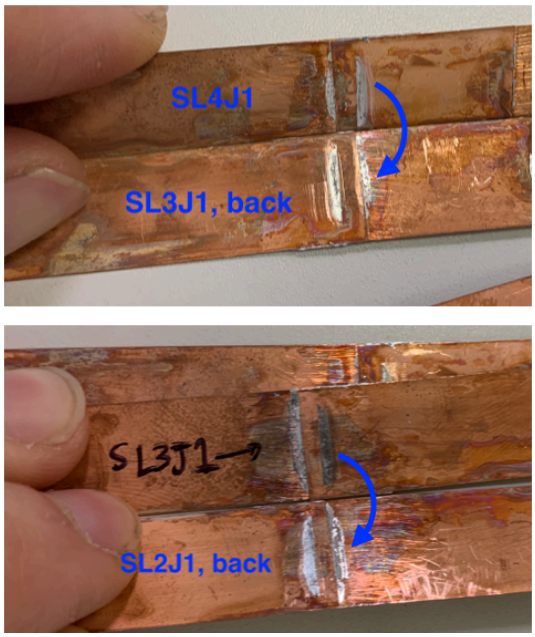

(a) Restoring of south row

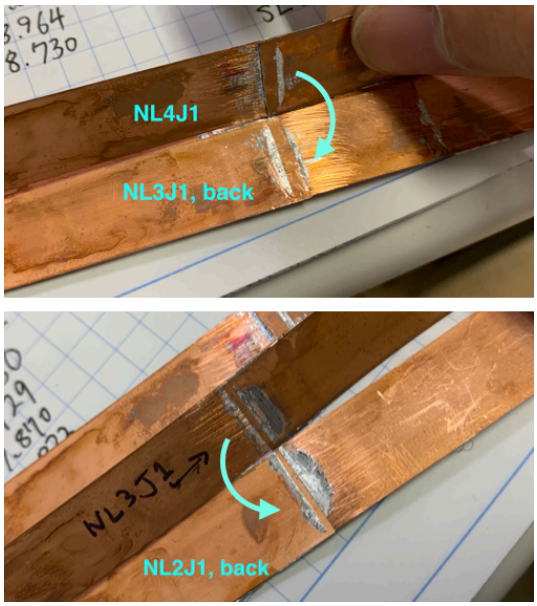

(b) Restoring of north row

Fig. 5.39: Restoring procedure of SimpleStack 2

The restored rows of SimpleStack 2 is shown in Fig. 5.40, and the imaged layers position before and after the pressurization was illustrated in Fig. 5.41. The reason for extruded indium at unexpected location is the accidentally misaligned layers, and the overlapping at the joint section of layer 3 was caused. The misaligned layer caused a part of the lap joint at layer 1 joint 2 out of the pressurizing area, and created an indentation on the top surface. The previous study [39] reported the overlapping area causes the stress concentration and deteriorate the I_c of the REBCO tape. And the edge of pressurizing also cause of stress concentration. Since the simple-stack procedure does not fix the REBCO tapes, the apprehensiveness for misalignment of REBCO tape was unfortunately validated. The pressurizing was concentrated on the overlapped area, whereas other area experience low pressure and the resulting indium lasted thick. The contact resistivity of these area is need to be analyzed and discussed.

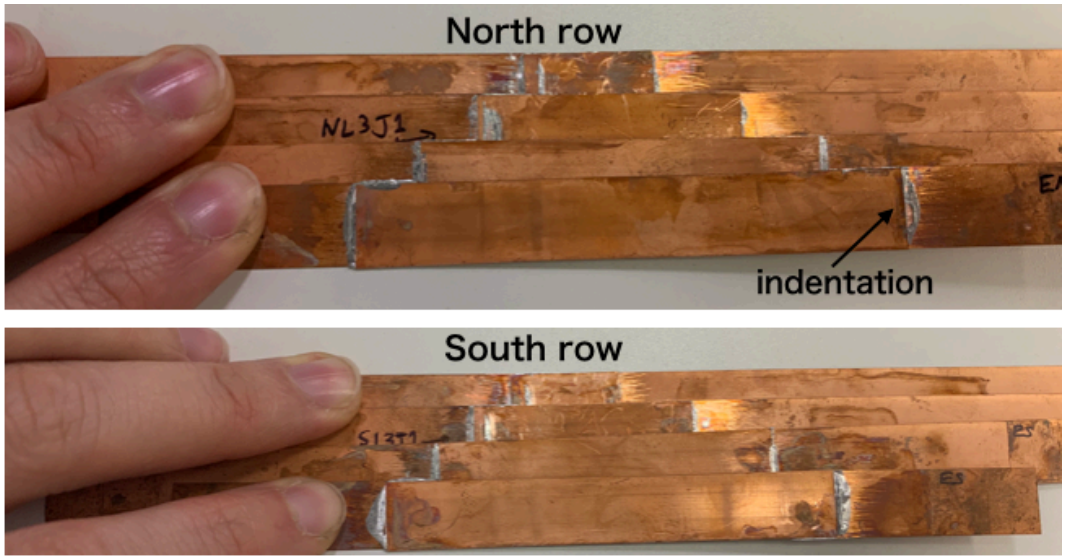

Fig. 5.40: Aligned layers of SimpleStack 2

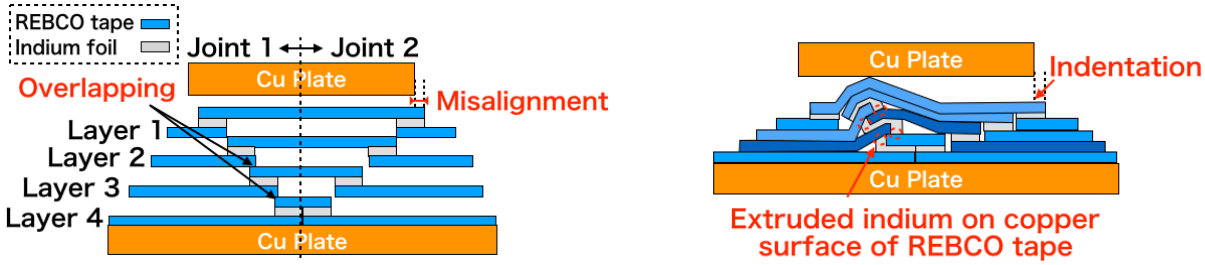

(a) Before pressurization

(b) After pressurization

Fig. 5.41: Schematic side view of restored SimpleStack 2

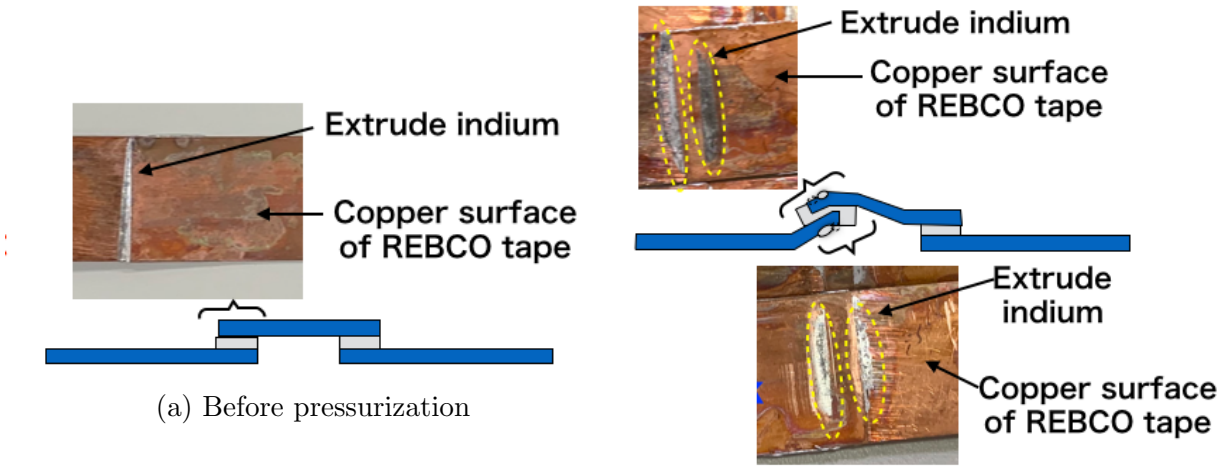

(a) Before pressurization

(b) After pressurization

Fig. 5.42: Schematic side view of restored SimpleStack 2

5.5 Evaluation of contact resistivity

5.5.1 Calculation of contact resistivity

For the single-layer lap joint sample, the contact resistance was calculated using Eq. 4.3. And the contact resistivity calculated using Eq. 4.4 were listed in Table 5.3.

Table. 5.3: Contact resistivity of single layer lap joint sample

Sample name	Contact resistivity ($p\Omega m^2$)
SingleLap1	2.60
SingleLap2	3.25
SingleLap3	4.04
SingleLap4	1.99
SingleLap5	2.74
SingleLap6	1.77
SingleLap7	2.22
SingleLap8	2.79

For the contact resistance of tow-row-four-layer joint sample, each layer have two lap joints and the current path are illustrated in Fig. 5.43.

Fig. 5.43: Current path at each layer of two-row-four-layer joint sample

Using subscripted i, j, k to distinguish layer ,joint, and contact interface respectively, it is reasonable to express the sum of four contact resistance, $\sum_{j=1}^{2}\sum_{k=1}^{2} R_{\mathrm{contact}i,j,k}$, by Eq, 5.6

$$\sum_{j=1}^{2}\sum_{k=1}^{2} R_{\mathrm{contact}\ i,j,k} = R_{\mathrm{joint}\ i} - \sum_{j=1}^{2}\left\{ \begin{array}{l} \sum_{k=1}^{2}\left(\rho_{\mathrm{Ag}}\frac{T_{\mathrm{Ag}}}{S_{\mathrm{CT}i,j,k}} + \rho_{\mathrm{inter}}\frac{1}{S_{\mathrm{CT}i,j,k}} + \rho_{\mathrm{Cu}}\frac{T_{\mathrm{Cu}}}{S_{\mathrm{CT}i,j,k}}\right) \\ +\rho_{\mathrm{In}}\frac{T_{\mathrm{In}}}{\sqrt{S_{\mathrm{CT}i,j,1}}\sqrt{S_{\mathrm{CT2}i,j,2}}} \end{array} \right\} \quad (5.6)$$

Where $\rho_{\mathrm{Ag}}, \rho_{\mathrm{Cu}}, \rho_{\mathrm{In}}$, are resistivity of silver, copper, and indium at 77 K ($\rho_{\mathrm{Ag}} = 2.70 \times 10^{-9}$ Ωm, $\rho_{\mathrm{Cu}} = 2.10 \times 10^{-9}\Omega$m, $\rho_{\mathrm{In}} = 1.67 \times 10^{-8}\Omega$m [75]), $T_{\mathrm{Ag}}, T_{\mathrm{Cu}}$ are the thicknesses of silver, copper. ρ_{inter} ($= 4.2$ $p\Omega m^2$) is the interlayer resistivity. $R_{\mathrm{joint}\ i}$, $S_{\mathrm{CT}i,j,k}$, and T_{In} are the results evaluated in subsection 5.4.2,subsection 5.4.3,and subsection 5.4.4,respectively. Since the contact resistance of each contact interface could not be evaluated separately, the average contact resistivity of each layer was utilized for discussion. The contact resistivity, $\rho_{\mathrm{contact}i}$, is calculated as Eq. 5.7.

$$\rho_{\mathrm{contact}\ i} = \sum_{j=1}^{2}\sum_{k=1}^{2} R_{\mathrm{contact}\ i,j,k} \times \frac{1}{\sum_{j=1}^{2}\sum_{k=1}^{2}\left(\frac{1}{S_{\mathrm{CT}i,j,k}}\right)} \quad (5.7)$$

The calculated contact resistivity of each layer from each joint sample is listed in Table 5.4.

Noting that overlapped layers and extruded indium explained in 5.4.5 influence the calculation of joint belong to SimpleStack-2. In these layers, the range of the resulting indium was assumed from 0 to measured thickness shown in Fig. 5.33, and the range of contact resistivity is expressed.

Table. 5.4: Contact resistivity of two-row-four-layer joint sample

Layer name	Contact resistivity of SimpleStack-1 ($p\Omega m^2$)	Contact resistivity of SimpleStack-2 ($p\Omega m^2$)	Contact resistivity of JointPiece-1 ($p\Omega m^2$)	Contact resistivity of JointPiece-2 ($p\Omega m^2$)
NL1	3.23	2.51	4.75	2.65
NL2	2.91	2.12-2.56	2.41	3.24
NL3	3.40	2.21-2.71	3.08	1.28
NL4	3.52	2.48-2.99	1.98	2.31
SL1	3.09	3.23	6.07	3.72
SL2	2.41	3.14-3.74	3.88	3.74
SL3	5.15	3.46-4.15	4.71	3.08
SL4	3.21	3.68-4.35	3.49	3.27

5.5.2 Contact resistivity distribution of two-row-four-layer joint samples

To surmise the reason for high contact resistivity of layers two-row-four-layer sample from the history of stress, the contact resistivity of each layer is arrayed according to the location of the joint in Fig. 5.44.

In the distribution of SimpleStack1, a distinct joint with high contact resistivity was shown in Fig. 5.44 (a). Since the pressure was applied by bolting, the bolts close to the joint L3J1 and L3J2 possibly applied less axial force by the handling. In the distribution of JointPiece1 shown in 5.44 (c), a tended distribution can be found more clearly. The contact resistivity at the center of north row was low, and it gradually increased as the location of the joint radiated to the outside of south row. This can be interpreted as the applied pressure at center of north row was high by over-tightening, and the tilted pressurizing resulted in low pressure at the outside.

Therefore, the non-uniform pressure by handling is reasonable to explain the location distribution of contact resistivity.

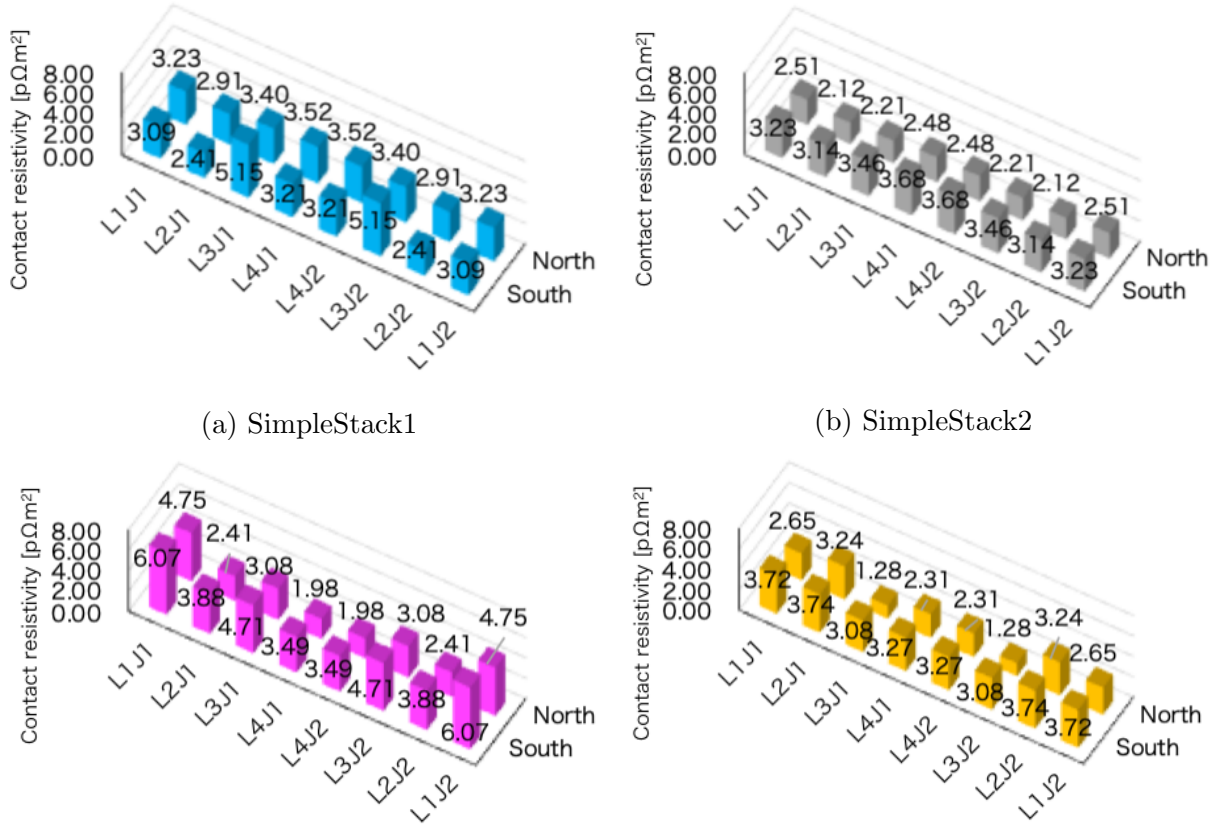

(a) SimpleStack1 (b) SimpleStack2

(c) JointPiece1 (d) JointPiece2

Fig. 5.44: Contact resistivity distribution of two-row-four-layer joint sample

5.5.3 Correlation between observed contact area and contact resistivity

The contact resistivity of all joint sample were compared with contact area in Fig. 5.45. The contact resistivity of three kind of joint sample: single-layer lap joint sample, two-row-four-layer joint sample with simple-stack procedure, two-row-four-layer joint sample with joint-piece procedure, ranged similar except one layer from SimpleStack1 and three layer from JointPiece1. The ratio that the observed contact area account for the conventional contact area (original joint length × REBCO tape width) was defined as normalized contact area. The correlation between normalized contact area and contact resistivity are shown in Fig. 5.45(b). The normalized contact area referred to the handling of fabrication, and it ranged from approximately 0.8 to 1.0. The duplicated range of contact resistivity can be confirmed more apparent nevertheless in the different contact area, or fabrication method. The reason for several high contact resistivity layers are need to be unveiled to discuss the relative merit and improve the joining.

5.5.4 Correlation between resulting indium thickness and contact resistivity

The joining pressure is one of the most important factors to the contact resistance, which induces plastically deformation of indium foil. Since the contact resistance calculated by Eq. 5.6 could not be separated into each joint, the parameter that related to the total contact resistance is

considered. The sum and difference of resulting indium thickness at two joints from same layer were compared with contact resistivity in Fig. 5.46 and Fig. 5.47, respectively. The correlation is

- Comparison with sum of resulting indium thickness The thick resulting indium thickness can be resulted from low joining pressure, and can be considered to be related to high contact resistivity. Fig. 5.46 shows the comparison between the contact resistivity and sum of resulting indium thickness of each layer from all two-row-four-layer joint samples. In Fig. 5.46 (a), the thicker resulting indium thickness tend to be higher contact resistivity with simple-stack procedure. However, this result could not fully explain the high contact resistivity since two thick and similar resulting indium thicknesses showing differenct contact resistivity was confirmed. In Fig. 5.46(b), the tendency show less correlation with joint-piece procedure. Considering the accessibility to each lap joint for the joint thickness measurement, the uncertainty of the resulting indium thickness is higher. The error of measurement caused difficulty in validating the correlation between resulting indium thickness and contact resistivity.

- Comparison with difference of resulting indium thickness The difference of resulting indium thickness was considered to reflect the non-uniform joint pressuring during the fabrication. Fig. 5.47 shows The comparison between the contact resistivity and difference of resulting indium thickness of each layer from all two-row-four-layer joint samples. However, no specific tendency could be found. In Fig. 5.47, the layers with large difference of resulting indium thickness surrounded by black dot line is corresponding to the result of overlapped layers explained in section 5.4.5. Since the extruded indium covers the copper surface of REBCO tape shown in Fig. 5.42 increased the thickness of joint and the difference of resulting indium thickness, the result of these thicknesses are not accurate. Therefore, these layers was excluded from the evaluation and discussion.

  Although the non-uniform pressure is considered to be applied on these layers, the averaged parameter of contact resistivity could not represent the detail contact resistivity

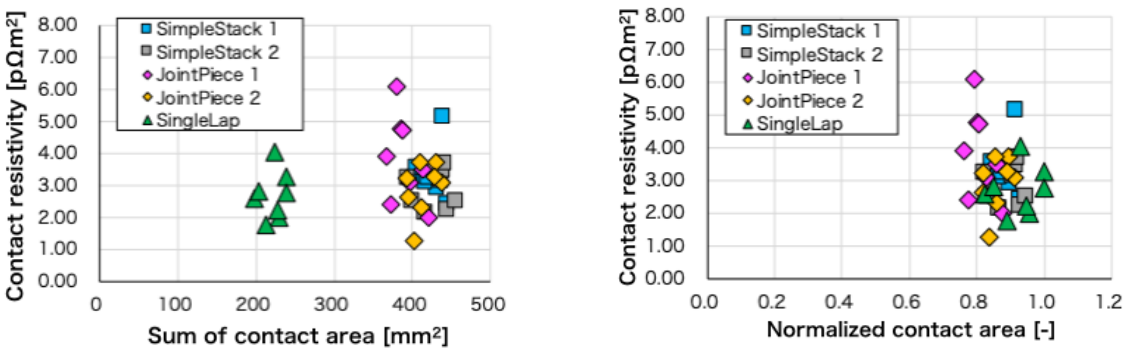

(a) Comparison with contact area (b) Comparison with normalized contact area

Fig. 5.45: Correlation between contact resistivity and contact area

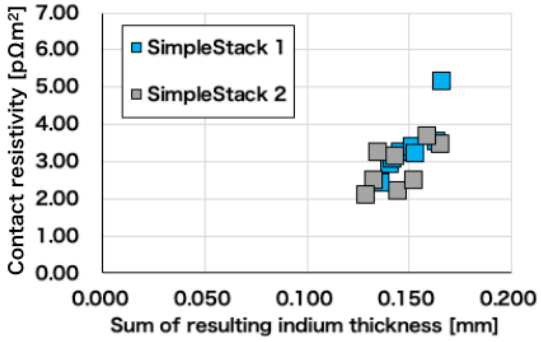

(a) Joint sample fabricated with simple-stack procedure

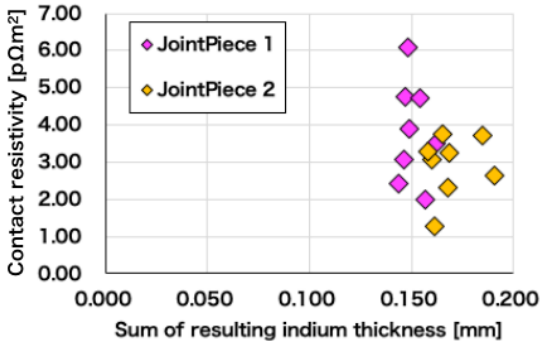

(b) Joint sample with joint-piece procedure

Fig. 5.46: Correlation between sum of resulting indium thickness and contact resistivity

distribution from this result.

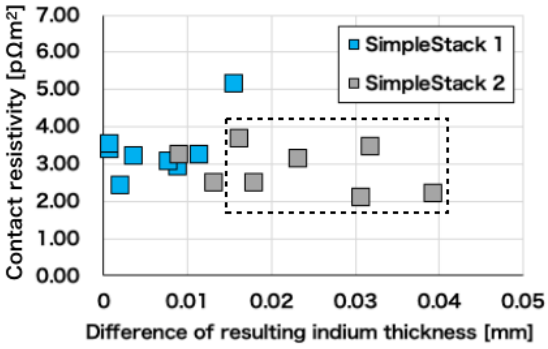

(a) Joint sample with simple-stack procedure

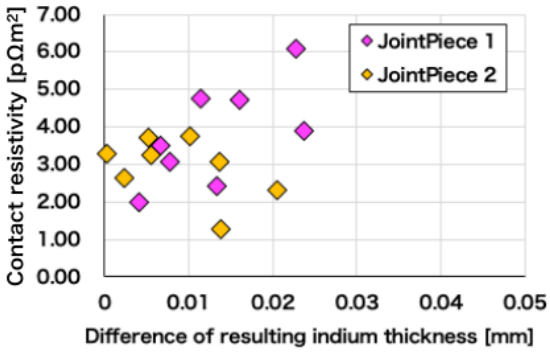

(b) Joint sample with joint-piece procedure

Fig. 5.47: Correlation between defference of resulting indium thickness and contact resistivity

The indium foil was plastically deformed by joining pressure with heating treatment, the low stress would decrease real contact area in micro-scale at contact interface and increase the contact resistance according to the theory of electric contacts [72]. The stress could not be measured after the pressuring.

5.6 Extrapolation of joint resistance using contact resistivity

5.6.1 Required condition

Based on the design of conductor from previous study [11], whether the acquired contact resistivity fulfill the requirement for joint resistance of each joint was considered. The designed specification of the conductor for helical fusion reactor is listed in Table 5.5

Table. 5.5: Specification of the HTS magnet conductor design for the helical fusion reactor

	Type-A	Type-B
Operation current	94 KA	94 kA
Operation temperature	20 K	20 K
Number of tapes	48 (2 row × 24 layers)	40 (2 row × 20 layers)

The required joint resistance for one joint is estimated to be 5 nΩfrom the perspective of cooling power. Cooling coolant requires electric power for running refrigeration system. In case the low-temperature superconducting (LTS) material was used for superconducting magnet, the power is expected to be 30 MW [22]. The aforementioned joint resistance gives an electrical power consumption comparable to the LTS option [45].

According to the Table 5.5, the conductor have 48 or 40 layers, which means the total electrical resistance in a joint is consist of 48 or 40 joint resistance in a parallel circuit. The requirement for joint resistance is calculated to be less than 240 nΩ and 200 nΩ for each type of conductor design. Here we applied the severe condition of 200 nΩ as criteria for each joint resistance, and compared it with extrapolated joint resistance.

5.6.2 Calculation for extrapolating joint resistance

The joint resistance of a mechanical lap joint fabricated with REBCO tape is consisted of several components as explained in section 1.3.3, and can be expressed as Eq. 5.8.

$$R_{\mathrm{joint}} = 2R_{\mathrm{contact}} + 2R_{\mathrm{Cu}} + 2R_{\mathrm{inter}} + 2R_{\mathrm{Ag}} + R_{\mathrm{In}} \tag{5.8}$$

R_{contact} is the contact resistance, R_{In} is the electric resistance of resulting indium at the joint, and $R_{\mathrm{Cu}}, R_{\mathrm{Ag}}, R_{\mathrm{inter}}$ are the electric resistance of copper layer, silver layer, and interlayer of REBCO tape, respectively. Considering the current path at the joint, each component can

Table. 5.6: Contact resistivity of two-row-four-layer joint samples

	Simple-stack procedure ($p\Omega m^2$)	Joint-piece procedure ($p\Omega m^2$)
Range	$2.12 - 5.15$	$1.28 - 6.07$
Average	3.11	3.35
Average of all	3.23	

be expressed as Eq. 5.9- 5.13.

$$R_{\mathrm{contact}} = \rho_{\mathrm{contact}} \times \frac{1}{S_{\mathrm{contact}}} \tag{5.9}$$

$$R_{\mathrm{In}} = \rho_{\mathrm{In}} \times \frac{T_{\mathrm{In}}}{S_{\mathrm{contact}}} \tag{5.10}$$

$$R_{\mathrm{Cu}} = \rho_{\mathrm{Cu}} \times \frac{T_{\mathrm{Cu}}}{S_{\mathrm{contact}}} \tag{5.11}$$

$$R_{\mathrm{Ag}} = \rho_{\mathrm{Ag}} \times \frac{T_{\mathrm{Ag}}}{S_{\mathrm{contact}}} \tag{5.12}$$

$$R_{\mathrm{inter}} = \rho_{\mathrm{inter}} \times \frac{1}{S_{\mathrm{contact}}} \tag{5.13}$$

The acquired contact resistivity R_{contact} range are summarized in Table 5.6. Using the maximum and minimum value of contact resistivity, the range of contact resistance can be calculated from the contact resistivity and contact area as shown in Fig. 5.48.

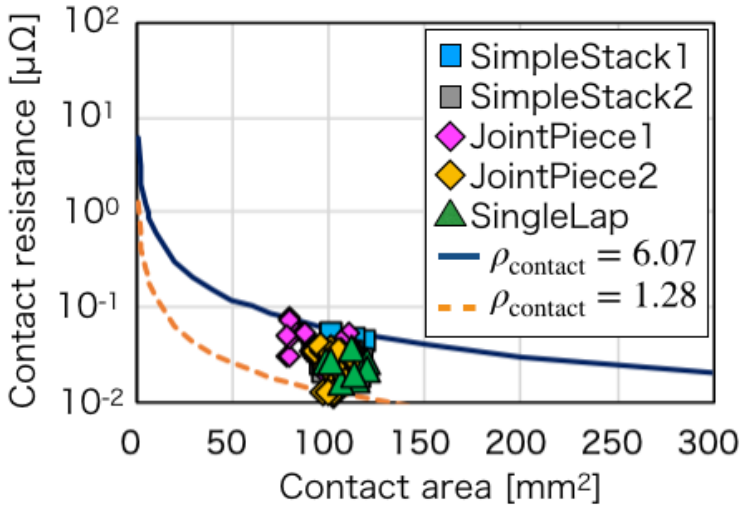

Fig. 5.48: Correlation between contact area and contact resistance

The extrapolated of joint resistance was calculated by two steps. First the contact area was modified, and second the electrical resistance at 20 K was estimated.

To identify the contact area S_{contact} for the extrapolation, the geometry of joint was considered. The length for each joint region is considered to be 1 m [45]. Since the bridge-type mechanical lap joint has two joints, and assumed to be 20 layers in this extrapolation, joint length for each layer is calculated to be 25 mm. The contact area is calculated to be 300 mm^2 by multiplying the joint length and 12 mm of REBCO tape width.

To identify the electrical resistivity of each components, the temperature dependence of each material was considered. For the contact resistance, the prediction equation studied in previous study [67] was used. For the electrical resistance of copper, silver, and indium, the electric resistivity was 1.7×10^{-10} Ωm, 0.3×10^{-10} Ωm, and 1.6×10^{-9} Ωm [75], respectively. The temperature dependence of interlayer resistance was studied in our recent study[74].The study concluded no temperature dependance of interlayer resistance could be confirmed. Therefore, the measured interlayer resistivity of 4.2 pΩm^2 at 77 K was used in the estimation for the interlayer resistance at 20 K.

5.6.3 Result of extrapolated joint resistance

The stepped variation of joint resistance are shown in Fig. 5.49- 5.51. The case of maximum contact resistivity, average contact resistivity, and minimum resistivity are extraplated. The result indicated the joint resistance at 20 K for each joint is much lower than the criteria of 200 nΩ even in the case of maximum contact resistivity. The ratio of joint resistance at 20 K was mainly consist of interlayer resistance and contact resistance. Considering the interlayer resistance of REBCO tape is predictable by sampling and evaluation using current transfer length measurement [74], screening and using REBCO tapes with lower interlayer resistance is effective to lower the joint resistance further more.

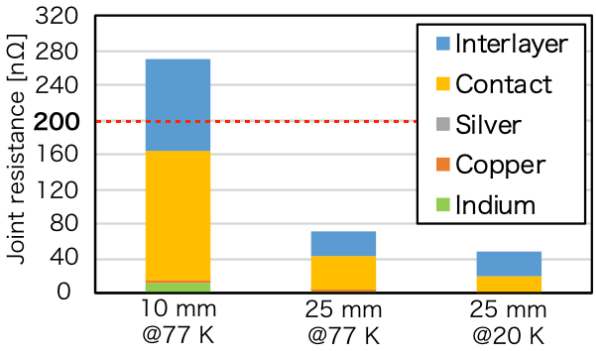

Fig. 5.49: Joint resistance extrapolation with $\rho_{\mathrm{contact}} = 6.07$ pΩm^2

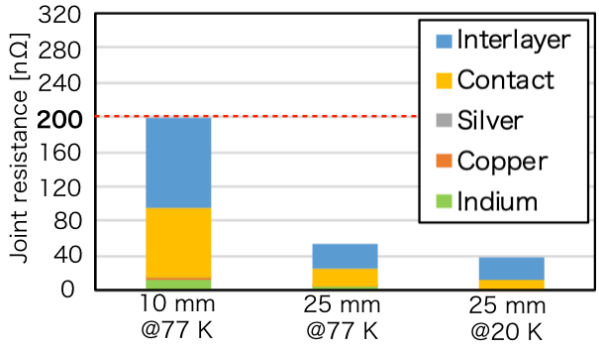

Fig. 5.50: Joint resistance extrapolation with $\rho_{\mathrm{contact}} = 3.23$ pΩm^2

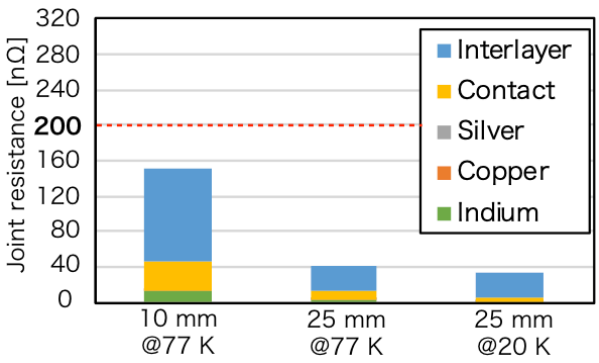

Fig. 5.51: Joint resistance extrapolation with $\rho_{\mathrm{contact}} = 1.28\ \mathrm{p\Omega m^2}$

5.7 Summary

In this section, the difference in contact condition result from different joint fabrication method was analyzed using X-ray CT scan. The joint samples fabricated with single-layer lap joint, two-row-four-layer joint with simple-stack procedure, two-row-four-layer joint with joint-piece procedure were prepared. The the cross-sectional images at contact interfaces of each joint was observed, and the contact resistivity was calculated from the joint resistance, joint thickness, and observed contact area.

Through the observation of contact interface, the overlapping layers accidentally cause by handling can be confirmed. The overlapping of REBCO tape is considered to be the cause of the stress concentration and deterioration of the REBCO tape. Therefore, inspecting the joint with X-ray CT scan before the cooling and energizing is effective to detect the situation illustrated in Fig. 5.52 and prevent using these possibly deteriorated REBCO tape in the conductor. In case these spot was found, appropriate procedure like disjoining and re-fabricating the joint can be taken.

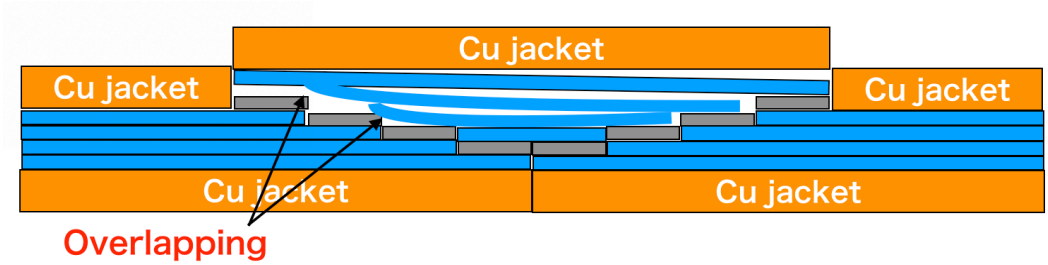

Fig. 5.52: Possible misalignment in joint fabrication

In the comparison of calculated contact resistivity from three kind of fabrication method, the range of each fabrication method was listed in Table 5.7 The result indicated no particular tendency of contact resistivity depending on the fabrication method can be confirmed. The contact resistivity is not a condition for selecting appropriate joint fabrication for application.

Table. 5.7: Contact resistivity range of three joint fabrication method

Single-layer lap joint ($p\Omega m^2$)	Two-row-four-layer joint with simple-stack procedure ($p\Omega m^2$)	Two-row-four-layer joint with joint-piece procedure ($p\Omega m^2$)
$1.77 - 4.04$	$2.12 - 5.15$	$1.28 - 6.07$

From the extrapolation of joint resistance, the expected joint resistance at 20 K with longer joint length is much lower than the criteria from the viewpoint of cooling power. Based on the characteristics of simple-stack procedure and joint-piece procedure, the freed REBCO tape in simple-stack procedure has a possibility to have misalignment and cause the deterioration in REBCO tape as Fig. 5.52. Therefore, the joint-piece procedure is suitable for the application for the joining.

6 Conclusion

6.1 Application of electrical characteristics evaluation

In this section, the applicability of predicting the joint resistance at cryogenic temperature using electrical characteristics measurement was evaluated. The acquired result is following.

- in the evaluation of electric characteristics, no frequency tendency can be confirmed.
- No correlation between the joint resistance at cryogenic temperature and electric impedance at cryogenic temperature can be found
- The correlation above indicates the even the joint resistance cryogenic temperature is high, no characteristics of the electrical impedance at room temperature can be used to predict this.
- From the numerical simulation to simulate the current path in the joint, the difference in the current path between the cryogenic temperature and the room temperature was found,
- The current at cryogenic temperature flows the direction perpendicular to the contact interface, whereas the current at room temperature flows the direction parallel to the contact interface.
- The difference in current path is results from the contrast of the electrical properties of the material
- The difference in current path results in difficulty of distinguishing the joint resistance from measurement at room temperature.
- Remediation by inducting current from the side was considered and simulated. and this method is sufficient to distinguish the existence of a full-width wide air gap, which was difficult in the conventional measurement of joint resistance at room temperature.
- The air gap that existed inside the joint is difficult to be detected since the induced current would flow concentrated on the area that normally contacted.

Therefore, we conclude the application of electric characteristics measurement is inadequate to evaluate the contact resistance at the joint.

6.2 Application of X-ray Computer Tomography scan

In this section, the applicability of an X-ray CT scan for evaluating contact condition was discussed. The acquired result is following.

- The extruded indium caused by pressuring of joining shown little influence on the evaluation of joint resistance. The four, the area of extruded indium was omitted.
- The cross-sectional images corresponding to the contact interfaces were extracted.
- The contact area and the area that contain the air gap could be confirmed visually, and the graph cut image segmentation technique was used to segment the contact area quantitatively.
- The segmented contact area shows the nominal contact area, which is simply calculated by multiplying the width of REBCO tape and original joint length, is tend to be greater than the actual contact area observed using X-ray CT.
- The comparison of the contact area before and after the cooling showed the cooling does not affect the contact area.
- Using the observed contact area can achieve more accurate contact resistivity than using the nominal contact area,
- The local degradation of REBCO tape and micro-order fine structure in the observed contact area is considered to account for dispersive contact resistivity, which could not be observed by current X-ray CT scan
- The range of contact resistivity evaluated accurately by introducing X-ray CT scan can be used to evaluate the contact condition.

Considering the achievement and the difficulties comprehensively, using an X-ray CT scan to inspect the contact interfaces and evaluate contact resistance is adequate.

6.3 Analysis on contact condition of joint sample using X-ray CT scan

In this section, the contact resistance variation depends on the joint fabrication method is evaluated using X-ray CT scan to give a conclusion of preferable joining method. The acquired result is following.

- The joint samples fabricated with single-layer lap joint, two-row-four-layer joint with simple-stack procedure, two-row-four-layer joint with joint-piece procedure were prepared.
- The the cross-sectional images at contact interfaces of each joint was observed, and the contact resistivity was calculated from the joint resistance, joint thickness, and observed contact area.
- Through the observation of contact interface, the overlapping layers accidentally cause by handling can be confirmed. The overlapping of REBCO tape is considered to be the cause of the stress concentration and deterioration of the REBCO tape. Therefore, inspecting the joint with X-ray CT scan before the cooling and energizing is effective to detect it
- The contact resistivity of single-layer lap joint sample, two-row-four-layer joint sample with simple-stack procedure, and two-row-four-layer joint sample with joint-piece procedure ranges 1.77-4.04 $p\Omega^2$, 2.12-5.15$p\Omega^2$, 1.28-6.07$p\Omega^2$, respectively
- comparison of calculated contact resistivity from three kind of fabrication method, no particular tendency of contact resistivity depending on the fabrication method can be confirmed.
- From the extrapolation of joint resistance, the expected joint resistance at 20 K with longer joint length was 50 $n\Omega$, which is much lower than the criteria of 200 $n\Omega$ from the viewpoint of cooling power.

Based on the characteristics of simple-stack procedure and joint-piece procedure, the freed REBCO tape in simple-stack procedure has a possibility to have misalignment and cause the deterioration in REBCO tape. Therefore, the joint-piece procedure is suitable for the application for the joining.

Acknoledgement

From the beginning to the last of my doctoral course, I've received so many dedicating advice and support from the people around me. Without their help, I could not have a chance to be the stage I'm now.

First, I'd like to appreciate my doctoral supervisor, Professor Hidetoshi Hashizume, for his accurate comment on my research and kindly advice on my daily life. Every time I discuss with him on the progress report or private, he helped me to find the point I missed so I could correct my direction. The eagerness of him cheered me up several times as an example I want to be. The most impressive comment he gave me was "do not think the research easy" when I lost my bearing on the research and try just to get the result easily. Thanks to his timely advice so I could stop and correct the direction of the research. I will keep his words in my mind and face the coming challenges calmly and patiently. I'm grateful to get the chance to become a member of his laboratory from my bachelor's degree and study under his advice.

I'd also like to appreciate Associate Professor Satoshi Ito for his dedicated support to my research related to the superconductor and kindly comment about everything in the laboratory life. His precise and accurate comment on the discussion greatly helps me to proceed with my research in an effective direction. His effort on improving the environment of the laboratory changes the atmosphere of the member and greatly improved the collaborative work environment with each other. I'm grateful to be a Ph.D. candidate under his advice and work as a member of his team.

I'd like to appreciate Associate Professor Noritaka Yusa for everything he provided me: the new topic of research, chance for studying abroad, meeting new people, patient on my research and altitude, and especially for his idea from the viewpoint as a member of society. His candid and incisive comment always makes me clearly understand the problem I'm having. His advice showed me and the real opinion of a member of society and kept me alarm for being left from a society. I would never forget his dedicating support at night before an important interview that he spend his time with me to practice until midnight. I'm grateful to be a student of him to study and encounter so many things that others could not experience.

I'd like to appreciate Professor Shigeo Matsuyama and Professor Akira Hasegawa for being a member of the dissertation committee and providing valuable comments to my research.

I'd like to appreciate the Japan Society for the Promotion of Science for providing financial support on my research and helping me concentrate on the research activity.

I'd like to thank my colleague, Aparicio Luis, for working together with me through the whole doctoral course. His rhythmical singing and beating always remind me I'm not alone, especially in the last year of the doctor. Discussion with him is always fun and valuable, and this could keep my motivation to continue my doctoral course to the last. I'm grateful to become

a colleague of him and work with him.

I'd like to thank Associate professor Shinji Ebara and Associate Professor Weiying Cheng for giving me a lot of valuable comments on my progress report and presentation rehearsal for academic conferences. I'd like to thank Mrs. Yumi Omoto for her kind and patient support in the office procedure throughout the time I belong to the laboratory. I'd like to thank Assistance Professor Hiroki Shishido and Dr. Kota Sakaki for their support from the viewpoint of upper-classman in the laboratory. I'm grateful to be their junior colleague to escape from the detour in the doctoral course.

I'd like to especially thank Mr. Isamu Sugawara from the Creative Engineering Center, who provided the environment and technique of manufacturing to support my experiment technically in the back.

The members from our Hashizume, Ito, Ebara, Cheng Laboratory, and Niibori, Yusa laboratory, also provided great help to me. I'd like to thank Dr. Jiuhao Ge, Mr. Guanren Chen, Mr. Shin Hasegawa, Mr. Takuya Katagiri, Mr. Makoto Kawamoto, Mr. Kohei Yuki and Mr. Haicheng Song for spending time to discuss with me. It was a very exciting and valuable time to experience a different kind of idea from them. And I'd like to thank the students of the master degree, Mr. Kazuto Osawa, Mr. Taku Kitasaka, Mr. Shota Sakurai, Mr. Sotaro Sato, Mr. Kanaki Nakamura, Mr. Haruumi Yamamoto, and Mr. Takuma Tomozawa for sharing their precious idea and delightful time with me. And in particular, I'd like to thank Mr. Ryoichiro Hayasaka for discussing with me about his idea about the interlayer resistance measurement, and sending time for sharing his know-how about the measurement.

Finally, I would sincerely appreciate my father, Mr. Xiaming Chen, and my mother, Mrs. Aijing Lin, for providing a strong backbone for my life and continually support me until the last.

References

[1] M. Seki
Introduction to nuclear fusion reactor engineering : Challenge for the future energy
Nikkan Kogyo Shimbun, (2001) in Japanese

[2] National Institute for Fusion Science, viewed 5 January 2020
<http://www.nifs.ac.jp/ene/qa/qa_02.html>

[3] Nikola Jaksic, Paul van Eeten, Victor Bykov, Felix Schauer
Analysis of the magnet support structure for the plasma fusion experiment Wendelstein 7-X
plasma Physics and Controlled Fusion, Vol 36(1994), 317-353

[4] T. Mito, J. Yamamoto, K. Takahara, N. Yanagi, O. Motojima
"Stability tests on R&D superconductors for the Large Helical Device"
Cryogenics 31 (7), pp. 634-639

[5] K. Takahata
Superconducting coils for fusion
J. Plasma and Fusion Research, Vol. 81, pp. 273-279, (2005), in Japanese

[6] L. Bromberg, M. Tekkula, L. A. El-Guebaly, R. MIller, and ARIES Team
"Options for the use of high temperature superconductor in Tokamak fusion reactor designs,"
Fusion Engineering and Design, vol. 54, no. 2, pp. 167-180, Feb. 2001.

[7] H. Hazhisume, S. Kitajima, S. Ito, K. Yagi, U. Usui, Y. Hida, A. Sagara
"Advanced fusion reactor design using remountable HTc S. C. magnet,"
J. Plasma Fusion Res. SERIES., vol. 5, pp. 532-536, 2002.

[8] E. Monneret, L. Benkheira, E. Fauve, D. Henry, T. Voigt, S. Badgujar, H-S. Chang, G. Vincent, A. Forgeas, N. Navion-Maillot
ITER Cryoplant Final Design and Construction
IOP Conf. Series: Materials Science and Engineering 171 (2017) 012031

[9] K. Takahata, T. Mito, H. Tamura, S. Imagawa, A.Sagara,
Conceptual design of an indirect-cooled superconducting magnet for the LHD-type fusion reactor FFHR
Fusion Engineering and Design, Vol.82, Issues 5-14, (2007), pp.1487-1492

[10] A. Sagara, H. Tamura, T. Tanaka, N. Yanagi, J. Miyazawa, To. Goto, R. Sakamoto, J. Yagi, T. Watanabe, S. Takayama, the FFHR design group
Helical reactor design FFHR-d1 and c1 for steady-state DEMO
Fusion Engineering and Design, vol. 89, no. 10, pp. 2114-2120, Oct. 2014.

[11] N. Yanagi, Y. Terazaki, S. Ito, K. Kawai, Y. Seino, T. Ohinata, Y. Tanno, K. Natsume, S. Hamaguchi, H.Noguchi, H. Tamura, T. Mito, H. Hashizume, and A. Sagara,
Progress of the HTS magnet option and R&D activities for the helical fusion reactor
IEEE Transactions on Applied Superconductivity, Vol. 24, No. 3, 4202805, 2014

[12] A. Sagara, J. Miyazawa, H. Tamura, T. Tanaka, T. Goto, N. Yanagi, R. Sakamoto, S. Masuzaki H. Ohtani and The FFHR Design Group
Two conceptual designs of helical fusion reactor FFHR-d1A based on ITER technologies and challenging ideas
Nucl. fusion, vol. 57, no. 8, 086046, Jul. 2017.

[13] N.Yanagi, T. Goto, J. Miyazawa, H. Tamura, Y. Terazaki, S. Ito, T. Tanaka, H. Hashizume, A. Sagara
Progress in the Conceptual Design of the Helical Fusion Reactor FFHR-d1
Journal of Fusion Energy, Vol 38, 147-161, 2019

[14] M. Koizumi, S. Murase, H. Shiraki and O. Horigami
Nb_3Sn Superconducting Coil by Wind and React Method
Technical note, (1979) in Japanese

[15] N. Yanagi, T. Mito, K. Takahata, T. Saito, J. Yamamoto, O. Motojima, The LHD Group
Development and quality control of the superconductors for the helical coils of LHD
Fusion Eng. Des., Vol. 41, pp. 241-246, (1998)

[16] O. Motojima et al.
Progress Summary of LHD Engineering Design and Construction
Nucl. Fusion, Vol. 40, pp. 599-609, (2000)

[17] T.Horiuchi, Y.Monju, N.Suzuki, T.Kawai, M.Hamada, K.Inoue, K.Uo, O.Motojima
Contact resistance of demountable multi-pin joint for superconducting helical coil
IEEE Transactions on Magnetics, Vol.23, (1987),pp.580-583

[18] H.Hashizume, S.Kitajima, S.Ito, K.Yagi, Y.Usui, Y.Hida
Advanced fusion reactor design using remountable HTc S.C. magnet
Plasma and Fusion Research, Vol.5, (2001),pp.532-536.

[19] S. Ito and H. Hashizume
Overview of fundamental study on remountable HTS magnet
Fusion Engineering and Design, Vol. 81, no. 22, pp. 2527-2533, Nov. 2006.

[20] N.Yanagi, K.Nishimura, G.Bansal, A.Satara, O.Motojima,
Split and Segmented Type - Helical Coils for the Heliotron Fusion Energy Reactor
Plasma and Fusion Research, Vol.5, S1-26,(2010)

[21] H. Hashizume, S. Ito
Design prospect of remountable high-temperature superconducting magnet
Fusion Engineering and Design, vol. 89, no. 9-10, pp. 2241-2245, Oct. 2014.

[22] N. Yanagi, T. Mito, R. Champailler, G. Bansal, H. Tamura, A. Sagawa
Design progress on the high-temperature superconducting coil option for the heliotron-type fusion energy reactor FFHR
Fusion Science and Technology, vol 60. no. 2, pp. 648-652, Aug. 2011.

[23] N.Yanagi, S. Ito, Y. Terazaki, K Natsume, H. Tamura, S, hamaguchi, T. Mito, H. Hashizume, J. Morikawa, Y. Ogawa, M. Iwakuma, A. Sagara
"Feasibility of HTS Magnet Option for Fusion Reactors"
Plasma and Fusion Research, Vol. 9, 1405013, 2014

[24] N. Yanagi, S. Ito, Y. Terazaki, Y. Seino, S. Hamaguchi, H. Tamura, J. Miyazawa, T. Mito, H. Hashizume and A. Sagara
"Design and development of high-temperature superconducting magnet system with joint-winding for the helical fusion reactor"
Nucl. fusion, vol. 55, no. 5, 053021, Apr. 2015.

[25] L. Bromberg, H. Hashizume, S.Ito, J.V. Minervini, N.Yanagi,
"Status of High Temperature Superconducting Magnet Development"
Fusion Science and Technology, Vol.60(2),(2011),pp.635-642

[26] Z. S. Hartwig, C. B. Haakonsen, R. T. Mumgaard, and L. Bromberg
And initial study of demountable high-temperature superconducting toroidal field magnets for the Valcan tokamak conceptual design
Fusion Engineering and Design, vol. 87, no. 3, pp. 201-214, Mar. 2012.

[27] Z.S.Hartwig, C.B.Haakonsen, R.T.Mumgaard, L.Bromberg,
"An initial of domountable high=temperature superconducting toroidal field magnets for the Vulcan tokamak conceptual design"
Fusion Engineering and Design Vol 87, No. 3, pp, 201-214 , 2012

[28] B. N. Sorbom, J. Ball, T. R. Palmer, F. J. Mangiarotti, J. M. Sierchio, P. Bonoli, C. Kasten, D. A. Sutherland, H. S. Barnard, C. B. Haakonsen, J. Goh, C. Sung, D. G. Whyte
ARC: A compact, high-field, fusion nuclear science facility and demonstration power plant with demountable magnets
Fusion Engineering and Design, vol. 100, pp. 378-405, 2015.

[29] J. Lu, K. Han, W. R. Sheppard, Y. L. Viouchikov, K. W. Pickard, and W. D. Markiewicz
"Lap Joint resistance of YBCO Coated Conductors"
IEEE Transaction on Applied Superconductivity, vol. 21, no. 3, 3009, Jun. 2011.

[30] R. Tediosi, M. Alessandrini, C. Beneduce, S. Scheneider, and D. Eckert
"Low Temperature and Magnetic Field Performance of Spliced Commercial YBCO CC,"
IEEE Transaction on Applied Superconductivity, vol. 22, no. 3, 6600804, Jun. 2012.

[31] N. Bagrets, A. Augieri, G. Celentano, G. Tomassetti, K. Weiss, and A. della Corte
"Investigation of ReBCO Conductor Tape Joints for Superconducting Applications"
IEEE Transaction on Applied Superconductivity, vol. 25, no. 3, 6602705, Jun 2015.

[32] T. Nakanishi, T. Machi, T. Izumi, R. Teranishi, T. Kato, T. Kato and T. Hirayama
"Jointing of Coated Conductors by Using Nano-particle Metal Pastes"
Phys. Procedia, vol. 81, pp. 105-108, 2016.

[33] H. S. Shin, J. M. Kim
"Parametric Study for Low-Resistance Joint of REBCO Coated Conductor Tapes Using Ultrasonic Welding"
IEEE Transaction on Applied Superconductivity, vol. 26, no. 3, 6603205, Apr. 2016.

[34] H. S. Shin, J. M. Kim and M. J. Dedicatoria
"Pursuing Low Joint Resistivity in Cu-stabilized ReBa2Cu3O δ Coated Conductor Tape by The Ultrasonic Weld-solder Hybrid Method"
Supercond. Sci. Techno. vol. 29, 015005, 9pp, 2016.

[35] T.Ohinata, S.Ito, H.Hashizume
Fundamental evaluation of joint resistance in mechanical butt joint of a stacked GdBCO conductor
Plasma Fusion Research, No. 7, 2405045, 2012

[36] S.Ito, T.Ohinata, L.Bromberg, H.Hashizume
Structure improvement and joint resistance estimation in demountable butt and edge joints of a stacked REBCO conductor a within metal jacket
IEEE Transactions on Applied Superconductivity vol 23, no 3, 6425423, 2013

[37] S.Ito, L.Bromberg, M.Yakayasu, J.Minervini, H.Hashizume
Proposal of electrical edge joint for a demountable high-temperature superconducting magnet
IEEE Transactions on Plasma Science, vol. 23, no 5, 1446-1452, 2012

[38] K. Kawai, S. Ito, T. Seino, N. Yanagi, H. Tamura, A. Sagara, H. Hashizume
Optimization of a mechanical bridge joint structure in a stacked HTS conductor
IEEE Transaction on Applied Superconductivity, vol. 23, no. 3, 6409408, Jun. 2013.

[39] S. Ito, K. Kawai, Y. Seino, T. Ohinata, Y Tanno, N. Yanagi, Y. Terazaki, K. Natsume, S. Hamaguchi, H. Noguchi, H. Tamura, T. Mito, A. Sagara. and H. Hashizume
Performance of a mechanical bridge joint for 30-kA-class high-Temperature superconducting conductors
IEEE Transactions on Applied Superconductivity, Vol.24, No.3, 2014, 4602305

[40] S. Ito, Y. Seino, N. Yanagi, Y. Terazaki, A, Sagara, H. Hashizume
Bridge-type mechanical lap joint of a 100 kA-class HTS conductor having stacks of GdBCO tapes
Plasma and Fusion Research, vol. 9, 3405086, Jun. 2014.

[41] Y. Seino, S. Ito, H. Hashizume
Joint resistance characteristics of mechanical lab joint of a GdBCO tape with a change in temperature and magnetic field
IEEE Transactions on Applied Superconductivity Vol. 24, No. 3, 4602105. 2014

[42] C. Scheuerlein, M. Di. Michiel, M. Scheel, J. Jiang, F. Kametani, A. Malagoli, E. E. Hellstrom and D. C. Lardalestier
"Void and phase evolution during the processing of Bi-2212 superconducting wires monitored by combined fast synchrotron micro-tomography and X-ray diffraction"
Supercond. Sci. Technol. vol. 24, No. 11, 115004, Sept. 2011.

[43] M. Inoue, H. Tartara, K. Harada, K. Higashikawa, S. Ye, A. Matsumoto, H. Kumakura, and T. Kiss
"Three-Demensional Analysis of MgB2 Wire by use of X-ray Micro-Tomography"
IEEE Transactions on Applied Superconductivity, vol. 26, No. 3, 6201004, Apr. 2016.

[44] I. Tiseanu, L. Zani, T. Craciunescu, F. Cotorobai, C. Dobrea, A. Sima
"Characterization of superconducting wires and cables by X-ray mico-tomography"
Fusion Engineering and Design, vol. 88, pp. 1613-1618, Mar. 2013.

[45] S. Ito, N. Yusa, N. Yanagi, H. Tamura, A. Sagara, H. Hashizume
"Mechanical and electrical characteristics of a bridge-type mechanical lap joint of HTS

STARS conductors"
IEEE Trans. Appl. Supercond., vol. 26 no 2, March 2016.

[46] T. Nishio, S. Ito, N. Yusa, and H. Hashizume
"Reducing Joint Resistance by Heat Treatment During Fabrication of a Mechanical Joint of High-Temperature Superconducting Conductors"
IEEE Transactions on Applied Superconductivity, Vol.26, No.4, 2016

[47] T. Nishio, S. Ito, and H. Hashizume
"Heating and loading process improvement for indium inserted mechanical lap joint of REBCO tapes"
IEEE Transactions on Applied Superconductivity, Vol.27, No.4, 2017

[48] H. Hashizume, S. Ito, N. Yanagi, H. Tamura and A. Sagara
"Development of remountable joints and heat removable techniques for high-temperature superconducting magnets"
Nucl. fusion, vol. 58, no. 8, 026014, Dec. 2017.

[49] S. Ito, H. Hashizume, N. Yanagi, T. Tamura
"Advanced high-temperature superconducting magnet for fusion reactors: Segment fabrication and joint technique"
Fusion Eng. Des., vol. 136, part A, pp. 239-246, Nov. 2018.

[50] S. Ito, H. Hashizume, N. Yanagi, and H. Tamura
"Bridge-type mechanical lap joint of HTS STARS conductors using an integrated joint piece"
Fusion Engineering and Design, Vol. 146, 590-593, 2019

[51] The Institute of Electrical Engineers of Japan
Superconducting engineering, in Japanese
Ohmsha, 1991

[52] H. Enomoto
"Oxide High-T_c Superconductors" in Japanese
Journal of Cryogenics and Superconductivity Society of Japan, No 10, Vol. 29, 1994, pp. 537-544

[53] Y. Iijima and K Matsumoto
"High-temperature-superconductor coated conductors: Technical progress in Japan"
Superconducting Science and Technology, No. 13, 2000, 68-81

[54] SuperPower Inc. 2G HTS Wire, viewed at 10 July 2018
<http://www.superpower-inc.com/content/2g-hts-wire>

[55] Microfocus X-ray sources, viewed at 4 January 2020
<https://www.hamamatsu.com/jp/ja/product/light-and-radiation-sources/microfocus-x-ray-source/index.html>

[56] Y. Iwai
Series of progress in electric engineering 9, -X-ray computer tomography scanner-, in Japanese
Corona, 1979

[57] Scofield, J.H.
Theoretical Photoionization Cross Sections from 1 to 1500 keV
Lawrence Livermore National Laboratory Rep. UCRL-51326 (1973).

[58] Hubbell, J.H., Veigele, W.J., Briggs, E.A., Brown, R.T., Cromer, D.T., and Howerton, R.J.
Atomic Form Factors, Incoherent Scattering Functions, and Photon Scattering Cross Sections,
J. Phys. Chem. Ref. Data 4, 471-538 (1975); erratum in 6, 615-616 (1977)

[59] Hubbell, J.H. and Overbo
Relativistic Atomic Form Factors and Photon Coherent Scattering Cross Sections
J. Phys. Chem. Ref. Data 8, 69-105, (1979).

[60] M.J. Berger, J.H. Hubbell, S.M. Seltzer, J. Chang, J.S. Coursey, R. Sukumar, D.S. Zucker, and K. Olsen
XCOM: Photon Cross Sections Database, NIST Standard Reference Database 8 (XGAM), viewed at 4 January 2020
<https://www.nist.gov/pml/xcom-photon-cross-sections-database>

[61] Hubbell, J.H. and S. M. Seltzer
X-Ray Mass Attenuation Coefficients, NIST Standard Reference Database 126, viewed at 4 January 2020
<https://www.nist.gov/pml/x-ray-mass-attenuation-coefficients>

[62] T. Saito
Image processing algorithm, in Japanese
Kindai kagaku sha, (1993)

[63] G. N. Ramachadra and A. V. Lakshminarayanan
Three-dimensional reconstruction from radiographs and electron micrographs
Proceedings of the National Academy of Sciences of the United States of America, Vol. 68, No. 9, pp. 2236-2249, 1971

[64] L. A. Shepp and G. F. Logan
The Fourier reconstruction of a head section
IEEE Transaction on Nuclear Science, Vol NS-21,21-43, 1974

[65] Torque handbook, viewed at 20 April 2016
<https://en.global-tohnichi.com/download_services >

[66] Tohnichi Mfg. Co., Ltd.
Tohnichi torque handbook
Bolt tightening

[67] S.Ito, Y. Seino, T. Nishio, H. Oguro and H. Hashizume
Structure and Magnetic Field Dependences of Joint resistance in a Mechanical Joint of REBCO Tapes
IEEE Transactions on Applied Superconductivity, Vol. 26, No. 4, 2016, 6601505

[68] R. Achanta, A. Shaji, K. Smith, A. Lucchi, P. Fua, S. Susstrunk
SLIC Superpixels Compared to State-of-the-art Superpixel Methods
IEEE Trans. Pattern. Anal. Mach. Intell., Vol. 34, 11, pp2274-2282, Nov. 2012.

[69] C. Rother, V. Kolmogorov, A. Blake
"GrabCut" - Interactive Foreground Extraction using Iterated Graph Cuts
ACM Trans. Graph., vol. 23, 3, pp. 309-314, Aug. 2004.

[70] Julia F. Barrett, N Keat
Artifacts in CT: Recognition and Avoidance
RadioGraphics 2004, 24, 1679-1691

[71] J. B. P. Williamson and R. T. Hunt
"Asperity persistence and the real area of contact between rough surfaces"
Proc. R. Soxc. Lond. A. vol. 327, 147-157, Mar. 1972.

[72] R. Holm
Electric Contacts Theory and Application
Berlin, Heidelberg, Spring-Verlag, 1967.

[73] myVGL - The Free Viewer App for your 3D Data, downloaded at 10 October 2019,
<https://www.volumegraphics.com/en/products/myvgl.html>

[74] R. Hayasaka. S. Ito, H. Hashizume
Evaluation of interface resistance in a REBCO tape at different temperatures by contact-probing current transfer length method
IEEE Transactions on Applied Superconductivity, Vol.29, No.5, 2019, 9000805

[75] J. W. Ekin
Experimental Techniques for Low-Temperature Measurements
Boulder, Colorado: Oxford Univ. Press, 2006.